Astronomy Letters, Vol. 26, No. 4, 2000, pp. 199–203. Translated from Pis'ma v Astronomicheskiĭ Zhurnal, Vol. 26, No. 4, 2000, pp. 243–248.

Observations of the Gamma-Ray Flux from the Galaxy Mk 501

N. A. Andreeva, Yu. L. Zyskin, O. R. Kalekin, Yu. I. Neshpor, A. A. Stepanyan*, V. P. Fomin, N. N. Chalenko, and V. G. Shitov

Crimean Astrophysical Observatory, p/o Nauchnyĭ, Crimea, 334413 Ukraine

Received May 11, 1999; in final form, August 17, 1999

Abstract—We present two-year-long observations of the flux of very-high-energy (~10^{12} eV) gamma rays from the active galactic nucleus Mk 501 performed with a Cherenkov detector at the Crimean Astrophysical Observatory. A gamma-ray flux from the object was shown to exist at confidence levels of 11 and 7 standard deviations for 1997 and 1998, respectively. The flux varied over a wide range. The mean flux at energies >10^{12} eV, as inferred from the 1997 and 1998 data, is $(5.0 \pm 0.6) \times 10^{-11}$ and $(3.7 \pm 0.6) \times 10^{-11}$ cm^{-2} s^{-1}, respectively. The errors are the sum of statistical observational and modeling errors. The mean power released in the form of gamma rays is $\sim 2 \times 10^{43}$ erg s^{-1} sr^{-1}. © *2000 MAIK "Nauka/Interperiodica".*

Key words: *active galactic nuclei, gamma-ray observations, quasars and radio galaxies*

INTRODUCTION

Studies of gamma-ray fluxes provide valuable information about the processes that take place during the acceleration of high-energy particles in various objects. Gamma rays with energies $E < 10^{10}$ eV can be recorded only from satellites. CGRO/EGRET satellite measurements gave the largest amount of information [1]. More than a hundred mostly extragalactic gamma-ray sources have been discovered. Since the area of the EGRET detector is small, it is virtually impossible to record gamma ray with energies $E > 20$ GeV. From this point of view, ground-based measurements of the fluxes of very-high-energy (VHE) (>10^{11} eV) gamma rays with detectors of Cherenkov radiation produced when gamma-ray photons enter the Earth's atmosphere are of considerable interest. Two extragalactic sources of VHE gamma rays—the Markarian galaxies Mk 421 and Mk 501—were discovered with the 10-m Cherenkov detector at the Whipple observatory (USA) [2]. These objects are relatively close to our Galaxy: their redshift is $z = 0.04$. They are of great interest from an astrophysical point of view. These objects exhibit significant X-ray flux variations, which occasionally coincide with optical variations. The characteristic time scale of the variations ranges from several minutes to one year. The gamma-ray flux from Mk 501, which was discovered in 1995, was relatively low and accounted for 0.08 of the flux from the most stable gamma-ray source, the Crab nebula. However, the gamma-ray flux abruptly increased in the spring of 1997, when it exceeded the Crab flux by a factor of 5–10 during some bursts [3–6]. During this period, the flux exhibited significant night-to-night variations. The observations of Mk 501 were started at the Crimean Astrophysical Observatory (CrAO) in the spring of 1997 and continued in 1998. Preliminary results based on the 1997 data were reported by Kalekin *et al.* [7] in June 1998 at the International Cosmic-Ray Conference in Moscow. Here, we present the results of our analysis of the 1997 and 1998 observations reduced by a new method. The method and the results of data reduction are described below.

A BRIEF DESCRIPTION OF THE GT-48 GAMMA-RAY TELESCOPE

Gamma rays with energies $E > 10^{11}$ eV are recorded with ground-based instruments. The following fact is used: VHE gamma rays interact with the nuclei of air atoms to produce the so-called electron–photon showers composed of high-energy electrons and positrons, which emit optical Cherenkov photons at a small angle (1°) to the direction of motion of the primary photon. This makes it possible to determine the region from which the gamma-ray flux originates. Since the area illuminated by a Cherenkov flash is fairly large (~10^4 m^2), low gamma-ray fluxes (~10^{-11} cm^{-2} s^{-1}) can be recorded. The main obstacle to detecting and studying VHE gamma-ray sources is a substantial background of cosmic-ray particles, which produce Chenrenkov flashes in the Earth's atmosphere that are barely distinguishable from the flashes produced by gamma rays.

Multichannel cameras make it possible to cut off most of the flashes produced by charged cosmic-ray

* E-mail address for contacts: arnold@crao.crimea.ua

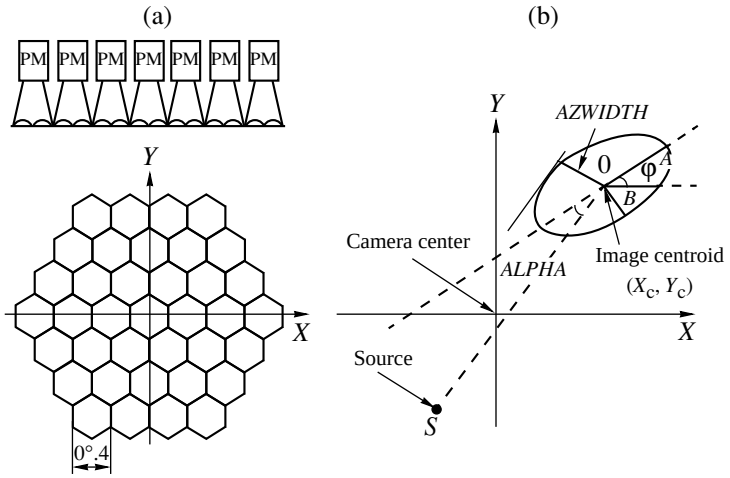

Fig. 1. (a) Scheme of the light detector; PM are photomultipliers. (b) The meaning of various flash parameters.

particles. Observations with the GT-48 multichannel camera attached to a dual telescope were started at the CrAO in 1989. We have repeatedly described GT-48 in various papers (see, e.g., [8]). The installation consists of two identical altazimuth mountings (sections), northern and southern, separated by a distance of 20 m in the north–south direction and located at an altitude of 600 m above sea level. Six simple telescopes are installed on each mounting. Until 1997 inclusive, three of the six telescopes had light detectors composed of 37 photomultipliers (37 cells) at their foci, which recorded visible (300–600 nm) images of Cherenkov flashes. A fourth telescope was connected to them in 1998. The field of view was $2^\circ.6$ and $0^\circ.4$ for the entire light detector and a single cell, respectively (see Fig. 1). The signals from the cells of the four telescopes pointed toward the same region of the sky are linearly added. We thus obtain a discretized image of the Cherenkov flash consisting of 37 numbers (the number of detector cells). Flashes are recorded only when the amplitudes of the coincident (in time) signals in any two of the 37 cells exceed the specified threshold. The coincidence circuit has a time resolution of 15 ns. The other two telescopes are intended to record ultraviolet flashes at wavelengths 200–300 nm. The area of the mirrors designed for recording optical light on each mounting (section) was 13.5 m^2 and 18 m^2 since 1998. The control system moves the installation with a tracking accuracy of $\pm 1'$. Observations can be carried out both in the mode of coincidence between the two sections and independently with each section. The gamma-ray energy detection threshold is 1.0 TeV. The telescope sensitivity to gamma-ray flux detection is 5 standard deviations in 8.5 hours of Crab observations [9].

OBSERVATIONS AND DATA ANALYSIS

The observations of Mk 501 ($\alpha = 16^h53^m47^s$ and $\delta = 39^\circ45'50''$, 1998) were performed with two aligned sections in coincidence mode with a time resolution of 100 ns. By contrast to single telescopes, using a dual installation in the mode of coincidence between the sections [10] rules out almost completely the recording of events caused by individual charged particles as they pass through the light detectors. We tracked the object by comparing observations of the gamma-ray source with background observations shifted in time from each other by 30 min. The source and background were observed at the same azimuth and zenith angles. We conducted a total of 59 and 39 sessions in 1997 and 1998, respectively (the duration of one session was 25 min). Sessions conducted under bad weather conditions were excluded from the data analysis. As the selection criterion, we chose the dispersion of count rates in 1 min during the session and the mean count rate. Sessions in which the dispersion of count rates differed from the theoretical one by more than two standard deviations were excluded. In addition, we did not consider sessions in which the count rate was less than half its maximum value at a given zenith angle. We analyzed the data from a total of 53 and 34 observing sessions in 1997 and 1998, respectively. The data were subjected to the following reduction: (1) we excluded data in which the total signal from the light detectors of all telescopes was larger than the signal saturating the analog-to-digital converter (about 150 photoelectrons) at least in one of the 37 channels; (2) we adjusted the signal amplitudes in individual channels using calibration coefficients; (3) we excluded flashes whose maximum amplitude was in the outer annulus of the detector cells; (4) we excluded events during which failures of the telescope tracking system were recorded (the telescope optical axis deviated by more than $3'$ from the specified direction). As a result of this preliminary data analysis, 30 139 source and 29 345 background events and 17 803 source and 17 393 background events observed in 1997 and 1998, respectively, were left for the subsequent analysis.

For the remaining events, we computed the first and second moments of the light distribution, from which we inferred the parameters of Cherenkov flashes: effective length *A*, effective width *B*, orientation φ characterizing the direction of maximum elongation of the flash image, and coordinates X_c, Y_c of the flash centroid (see Fig. 1). Having obtained these parameters, we can also infer other parameters of Cherenkov flashes [8].

Parameters *A* and *B* do not depend on the source position with respect to the flash and are called *coordinate-independent*. The effective length and width of the flash image and its orientation with respect to the direction of the presumed gamma-ray source, angle *ALPHA* (Fig. 1), are used to distinguish gamma-ray showers against the background of showers from charged particles (*p*-showers). This angle depends on the source position and is called a *coordinate-dependent parameter*. It is also used to calculate other coordinate-dependent parameters, for example, *AZWIDTH* (see Fig. 1). *DIST* is equal to the angular distance from the image centroid to the source position in the focal plane. Having determined the parameters of the flashes in the northern and southern sections, we averaged them. Averaging the flash parameters over two sections causes their relative fluctuations to decrease and, consequently, leads to a better separation of the flashes from gamma rays and those from charged cosmic-ray particles. We use this method for the first time.

As was already noted above, the parameters of the Cherenkov flashes from VHE gamma rays differ only slightly from the parameters of the flashes produced by charged cosmic-ray particles. The problem is that the distributions of parameters of the flashes, both from gamma rays and from charged particles, are broad and overlap considerably. However, selection by several different parameters makes it possible to exclude up to ≳99% of the flashes from charged particles. In this case, it is necessary to properly adjust the critical (boundary) values of the parameters to obtain an optimum signal-to-noise ratio = $(N_s - N_b)/\sqrt{N_s + N_b}$, where N_s is the number of gamma-like flashes selected in given source observations, and N_b is the number of gamma-like flashes in given background observations. The difference $N_s - N_b$ is interpreted as the number of gamma rays, and $\sqrt{N_s + N_b}$ is the statistical error of this number.

Our analysis of the observations shows that the optimum selection parameters for the 1998 data differ from those for the 1997 data. These differences are attributable to the changes in equipment characteristics resulting from the connection of the fourth telescope to each section.

Gamma-like events were selected by the following parameters: (1) by length *A*, we selected flashes with $A < 0.^\circ275$ for the 1997 data and $A < 0.^\circ315$ for the 1998 data; (2) by width *B*, we selected flashes with $B < 0.^\circ150$ for the 1997 data and $B < 0.^\circ165$ for the 1998 data; (3) we selected flashes with $AZWIDTH < 0.^\circ15$ for the 1997 data and $AZWIDTH < 0.^\circ225$ for the 1998 data; and (4) flashes with $0.^\circ55 < DIST < 1.^\circ00$ and $0.^\circ2 < DIST < 0.^\circ8$ were left in the 1997 and 1998 data, respectively. Our results are presented in the table.

We did not use other parameters, including parameter *UV* associated with the detection of ultraviolet emission, for the selection, because this did not lead to a considerable increase in the statistical significance of the results. Previously, we successfully used parameter *UV* in the reduction of Crab observations [9]. However, detection of ultraviolet emission depends strongly on observing conditions: zenith angle and atmospheric transmission, which differ markedly for the Crab nebula and Mk 501. This is apparently the reason why the selection by *UV* did not improve the results significantly.

We performed calculations of the gamma-ray flux using gamma-ray and *p*-shower simulations [11]. The flux averaged over the observation time in 1997 at energies $E > 1$ TeV was found to be $(5.0 \pm 0.6) \times 10^{-11}$ cm^{-2} s^{-1}. In 1998, the flux was $(3.7 \pm 0.6) \times 10^{-11}$ cm^{-2} s^{-1} (the errors are the total statistical observational and modeling errors).

The multichannel light detectors of second-generation gamma-ray telescopes allow the region of the sky in which a gamma-ray source is located to be pinpointed by the method of trial sources [12–14]. This method is based on the fact that, in the telescope focal plane, the images of the flashes from gamma rays are oriented toward the source, i.e., usually toward the camera center, while the major axes of the ellipsoids of *p*-shower images are oriented uniformly in all directions. Consequently, if we select flashes by taking an arbitrary point in the focal plane as the direction of the trial source, and if we use selection by angle *ALPHA*, then, to a first approximation, the number of remaining *p*-showers will not depend on the source position. At the same time, the number of images from gamma-ray showers will depend markedly on the position of the presumed source and will be at a maximum in the direction of the true source. We can construct the distribution of the number of selected flashes over the detector field of view and, thus, determine the position of the true

The number of recorded and selected events

Selection criterion	Number of on-source events	Number of background events	Difference	Difference-to-error ratio	Year
Without selection	30139	29345	794	3.26	1997
Selection by *A*, *B*	2446	2049	397	5.92	1997
Selection by *AZWIDTH*	819	423	396	11.24	1997
Without selection	17803	17393	410	2.19	1998
Selection by *A*, *B*	3107	2759	348	4.54	1998
Selection by *AZWIDTH*	1410	1054	356	7.17	1998

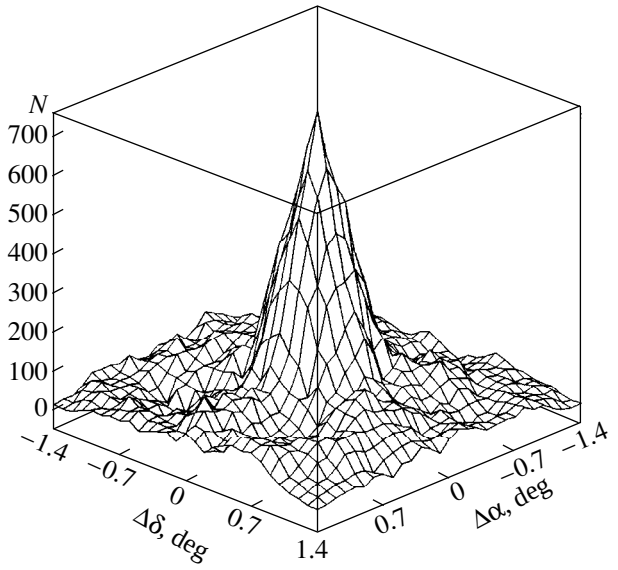

Fig. 2. Stereo "map" of the distribution of gamma-ray arrival directions. The map center coincides with the Mk 501 position; $\Delta\delta$ and $\Delta\alpha$ are the deviations from the source in declination and right ascension, respectively, and N is the number of events.

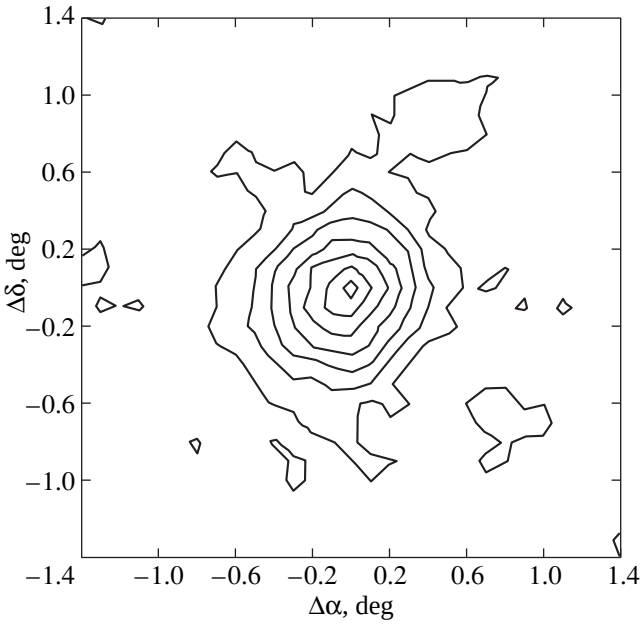

Fig. 3. Isophotes of the distribution of gamma-ray arrival directions. The notation is the same as in Fig. 2. The isophote step is 100 events.

gamma-ray source. We constructed three-dimensional histograms of selected sources based on the source (N_s) and background (N_b) observations using the parameters *A*, *B*, *DIST*, and *AZWIDTH*. Next, we subtracted the histogram for the background from the histogram for the source. Figure 2 shows a three-dimensional histogram for the sum of 1997 and 1998 data, and Fig. 3 shows isophotes of this distribution. The distribution maximum coincides with the position of Mk 501.

TIME VARIATIONS OF THE GAMMA-RAY FLUX

The gamma-ray flux from Mk 501 is known to be highly variable [3–6, 11]. Figure 4 shows our data on time variations in the flux of VHE gamma rays for 1997 and 1998. For comparison, the figure also shows the Whipple Observatory data kindly provided by T.C. Weekes. In 1997, the observations at the two observatories were performed almost on the same days with a difference in the detection times of ~10 h. In Fig. 4, we see a clear correlation (the correlation coefficient is 0.70 ± 0.13) between the Whipple and CrAO gamma-ray fluxes, which exhibited substantial variations in 1997. Only one gamma-ray burst was observed at the Whipple Observatory over the period of 1998 observations [Modified Julian Date (MJD) 50950–51050]. Unfortunately, no observations were made in Crimea at this time because of bad weather conditions. Since the flux variations were small during the simultaneous observations, there is no correlation between the Whipple and CrAO data.

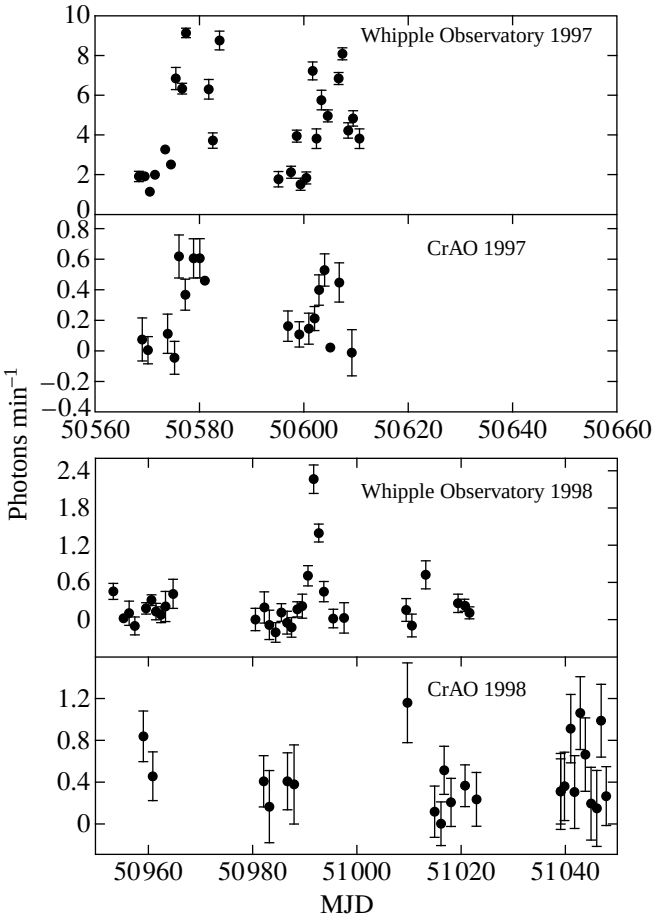

Fig. 4. Time variations in the (nightly mean) flux of gamma rays with energies $E > 1$ TeV and $E > 0.35$ TeV, as inferred from the CrAO and Whipple data for 1997 and 1998, respectively. Statistical errors are also given.

CONCLUSION

We may thus conclude that the active nucleus of the galaxy Mk 501 was a source of VHE gamma rays during 1997 and 1998. In quiescence, i.e., before 1997, the gamma-ray and X-ray fluxes were approximately 10^{43} and 10^{45} erg s^{-1}, respectively (see [15]). However, during gamma-ray bursts, the energy released in the form of gamma rays was comparable to the X-ray energy, which only doubles compared to that in quiescence. If the gamma-ray flux is assumed to be isotropic, then the total intensity of the $E > 1$ TeV gamma-ray emission is $\sim 3 \times 10^{44}$ erg s^{-1}. In active state, the flux of VHE gamma rays may be nonisotropic but have a narrow beam. The intensity of the emission per unit solid angle, 2×10^{43} erg s^{-1} sr^{-1}, seems more definite. The data obtained do not allow any conclusions to be reached about the angular width of the flux.

ACKNOWLEDGMENTS

We are grateful to N.A. Zhogolev, who operated the gamma-ray telescope, and to Z.N. Skiruta and S.G. Kochetkova for help with the data reduction and preparation of the paper.

REFERENCES

1. D. J. Thompson, D. L. Bertsch, B. L. Dingus, *et al.*, Astrophys. J., Suppl. Ser. **101**, 259 (1995).
2. J. Quinn, C. W. Akerlof, S. Biller, *et al.*, Astrophys. J. Lett. **456**, L83 (1996).
3. F. Krennrich, J. Boyle, J. H. Buckley, *et al.*, *The Kruger National Park Workshop on TeV Gamma Ray Astrophysics*, Ed. by O. C. de Jager (Potchefstroom Univ., Potchefstroom, 1997), p. 38.
4. F. Aharonian, A. G. Akhperjanian, J. A. Barrio, *et al.*, Astron. Astrophys. **327**, L5 (1997).
5. A. Djannati-Atai, *The Kruger National Park Workshop on TeV Gamma Ray Astrophysics*, Ed. by O. C. de Jager (Potchefstroom Univ., Potchefstroom, 1997), p. 21.
6. N. Hayashida, H. Hirasawa, F. Ishikawa, *et al.*, Astrophys. J. Lett. **504**, L71 (1998).
7. O. R. Kalekin, N. N. Chalenko, Yu. L. Zyskin, *et al.*, Izv. Ross. Akad. Nauk, Ser. Fiz. **63**, 606 (1999).
8. B. M. Vladimirskiĭ, Yu. L. Zyskin, A. P. Kornienko, *et al.*, Izv. Krym. Astrofiz. Obs. **91**, 74 (1995).
9. O. R. Kalekin, Yu. I. Neshpor, A. A. Stepanian, *et al.*, Pis'ma Astron. Zh. **21**, 184 (1995).
10. M. F. Cawley, J. Clear, D. J. Fegan, M. J. Lang, *et al.*, Exp. Astron. **1**, 173 (1990).
11. O. R. Kalekin, Izv. Krym. Astrofiz. Obs. **95**, 167 (1999).
12. C. W. Akerlof, M. F. Cawley, M. Chantell, *et al.*, Astrophys. J. Lett. **377**, L97 (1991).
13. Yu. I. Neshpor, A. P. Kornienko, A. A. Stepanian, and Yu. L. Zyskin, Exp. Astron. **5**, 405 (1994).
14. V. P. Fomin, S. Fennell, R. C. Lamb, *et al.*, Astroparticle Phys. **2**, 151 (1994).
15. M. Catanese, S. M. Bradbury, A. C. Breslin, *et al.*, Astrophys. J. Lett. **487**, L143 (1997).

Translated by A. Dambis

Astronomy Letters, Vol. 26, No. 4, 2000, pp. 204–207. Translated from Pis'ma v Astronomicheskiĭ Zhurnal, Vol. 26, No. 4, 2000, pp. 249–252.

Observations of Extragalactic Radio Sources at 36 GHz

N. S. Nesterov, A. E. Volvach*, and I. D. Strepka

Crimean Astrophysical Observatory, p/o Nauchnyĭ, Crimea, 334413 Ukraine

Received May 21, 1999; in final form, July 26, 1999

Abstract—The observations of 34 extragalactic radio sources with the 22-m Crimean Astrophysical Observatory radio telescope at 36 GHz in 1985–1994 are presented. Intensity variations were detected in 27 objects, which may result from the appearance of new components in their cores. © *2000 MAIK "Nauka/Interperiodica".*

Radio bursts from extragalactic radio sources are often accompanied by the appearance of new components near their cores (see, e.g., the review by Kellermann and Pauliny-Toth [1]). These components are directly revealed by VLBI observations. However, VLBI observations are carried out fairly rarely and with inadequate frequency coverage. For this reason, the data on spectral variability of active galactic nuclei obtained with single dishes provide additional valuable information about the physics of their activity.

Bursts usually develop first at short waves and then at long ones. An earlier detection of radio bursts and, consequently, the associated sources in the cores requires observations, for example, in the millimeter band. Variability studies of extragalactic radio sources at millimeter waves are continued at the Crimean Astrophysical Observatory (CrAO) [2]. Here, we present our observations of 34 objects at 36 GHz (a wavelength of 8.3 mm), which show the behavior of the flux densities from these sources in 1985–1994.

The observations were carried out with the 22-m CrAO radio telescope. The beam FWHM was 100″ at 8 mm. For our measurements, we used the superheterodyne radiometer with a degenerate parametric amplifier at its input produced at the Space Research Institute (Russian Academy of Sciences) and described by Strukov and Skulachev [3]. The sensitivity of the receiving system was about 0.5 Jy at a time constant of 1 s. The beam was modulated (switched) between two directions separated by 300″ in azimuth. The antenna temperatures from sources were measured by the standard ON–ON method described by Efanov *et al.* [4]. Before measuring the intensity, we determined the source position by scanning. The radio telescope was then pointed at the source alternately by the principal and reference (arbitrary) beam lobes formed during beam modulation and having mutually orthogonal polarizations. The antenna temperature from a source was defined as the difference between the radi-

The radio sources in which variations in radio intensity were observed

Source	Burst date, year	Burst amplitude, Jy	Source	Burst date, year	Burst amplitude, Jy
0106+013	<86.0	1.0	1253–055	91.1	15.8
	92.8	1.5		>94.3	10.5
0234+285	>87.3	3.7	1308+326	<85.7	>2.6
	92.8	1.6	1334–127	<86.1	>2.3
0235+164	>87.2	2.9		91.4	3.0
	91.1	2.3		>94.4	3.9
	92.8	6.6	1510–089	>87.3	2.8
0316+413	<86.2	34.9		90.3	4.1
0336–019	86.1	0.6		93.2	2.0
0355+508	<86.2	1.3		94.3	3.1
	91.2	1.0	1641+399	91.5	11.6
0415+379	91.7	1.3	1730–130	86.7	2.4
	92.8	1.3		90.2	3.9
	>94.3	1.7		93.2	3.1
0420–014	86.1	2.1		93.8	1.9
	91.7	4.7	1741–038	86.1	2.6
	92.8	1.7	1749+096	<85.7	7.0
0430+052	<86.0	1.4	1921–293	87.2	6.5
	90.3	2.7		92.4	6.3
	>93.9	1.1		>94.3	8.0
0528+134	86.0	1.7	2037+511	<90.0	1.1
	92.7	3.3	2145+067	<85.7	3.4
	93.7	2.6		87.6	3.4
0552+398	89.9	3.0		>94.4	3.8
	91.0	1.7	2200+420	>87.7	4.3
0735+178	91.2	3.4		89.9	3.7
0851+202	86.5	8.5		92.4	2.0
	<90.0	5.4	2223–052	>87.6	3.4
	91.7	2.7		90.0	6.2
	92.8	1.6	2251+158	90.8	3.7
0923+392	>94.4	7.2		93.2	7.4
1055+018	<86.0	2.1		>94.3	7.3
	92.2	1.3			
1226+023	91.5	30.2			
	93.8	5.2			

* E-mail address for contacts: volvach@crao.crimea.ua

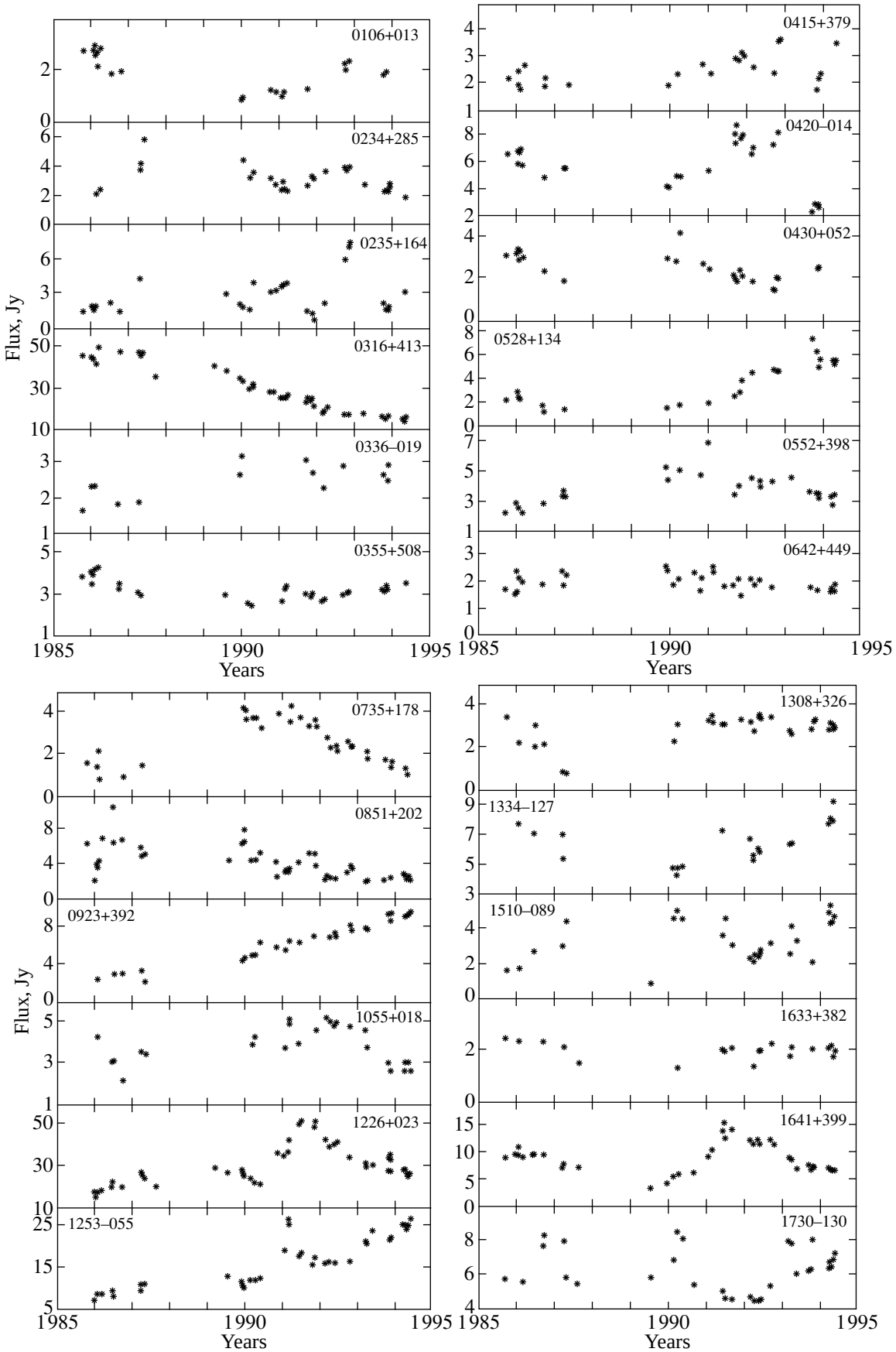

Fig. 1. Measured flux densities of the observed radio sources in 1985–1994.

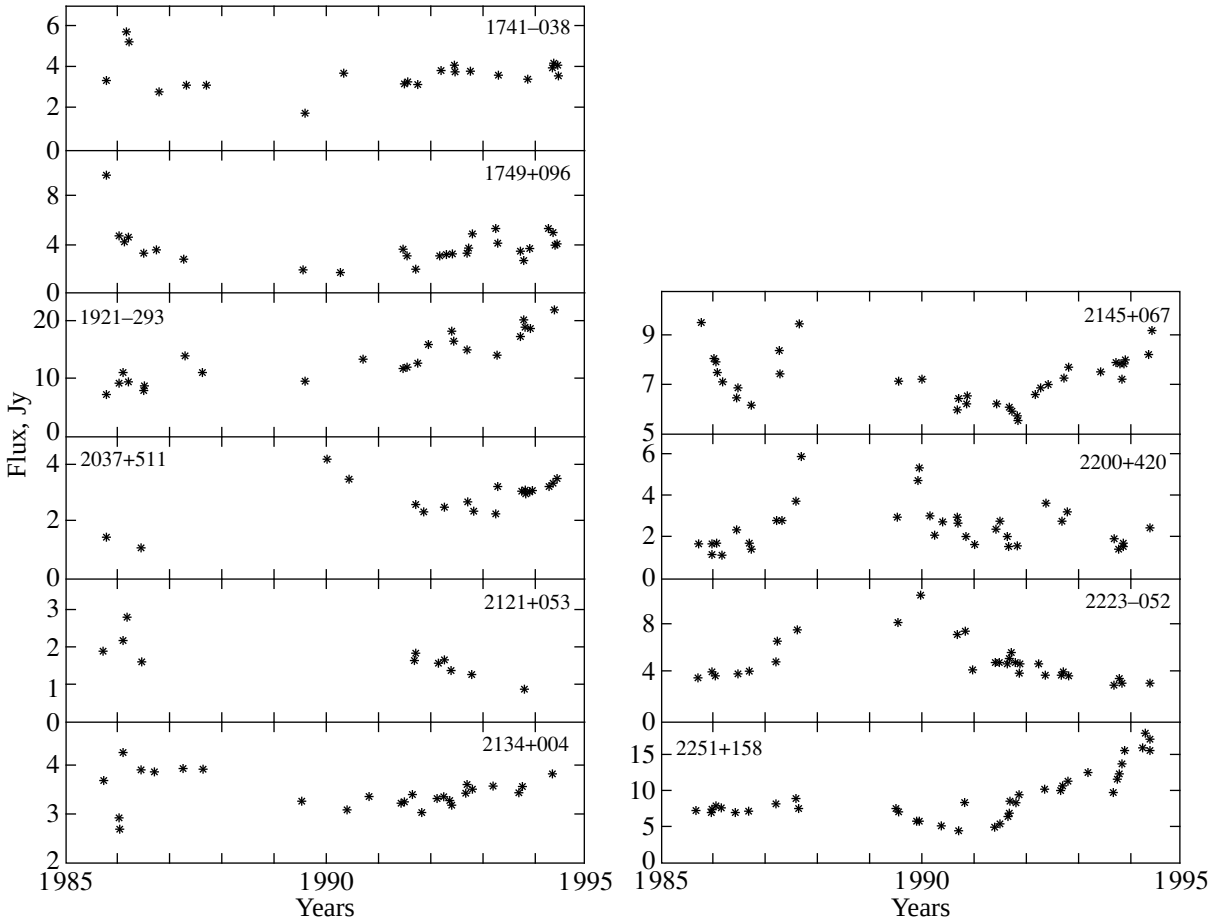

Fig. 1. (Contd.)

ometer responses averaged over 30 s at two different antenna positions. Depending on the intensity of the emission from sources, we made a series of 6–20 measurements and then calculated the mean signal intensity and estimated the rms error of the mean. The orthogonal polarization of the lobes allowed us to measure the total intensity of the emission from sources, irrespective of the polarization of this emission. Absorption in the Earth's atmosphere was taken into account by using atmospheric scans made every 3–4 hours.

The fluxes from the objects under study were calibrated by using measurements of the calibration sources 3C 123, 3C 274, DR 21, NGC 7027, and the planets Jupiter and Saturn, whose flux densities or brightness temperatures are given in [5]. When converting antenna temperatures to flux densities, we took into account the dependence of effective antenna area $A_{\rm eff}$ on elevation. According to our measurements of the calibration sources, the effective area of RT 22 decreased by ~20% as it was repointed from the zenith to an elevation of 15°. The error in the correction for changes in $A_{\rm eff}$, i.e., the scatter of points about the fitting curve, was about 2.5%, on the average.

In the figure, measured flux densities of the observed radio sources are plotted against time. The IAU source name is indicated in the upper right (or left) corner of each plot. The rms errors of the measured flux densities σ were determined by taking into account the following errors:

$\sigma_{\rm mean}$—the rms error of the mean estimated from a series of ON–ON measurements (noise and inaccurate telescope guiding);

$\sigma_{\rm ng}$—the measurement error of the signal from the noise generator used to track variations in radiometer gain (usually, $\sigma_{\rm ng} < 1\%$);

$\sigma_{\rm abs}$—the error introduced by uncertainty in the atmospheric absorption coefficient;

$\sigma_{\rm eff}$—the error in the correction for the dependence of $A_{\rm eff}$ on RT-22 position in elevation (on the average, $\sigma_{\rm eff} \approx 2.5\%$).

In most cases, the resulting errors are comparable to the symbol sizes in the figure.

The first column of the table lists the thirty radio sources in which we observed variations in radio intensity. Dates of the burst maxima and estimated burst amplitudes are given in the second and third columns,

respectively. The estimated burst amplitudes were defined as the difference between the flux density at burst maximum and its preburst minimum value. When the preburst minimum value was not recorded, the burst amplitude was defined as the difference between the flux density at burst maximum and its postburst minimum value.

The sources 0336–019, 0355+508, 0642+449, and 2134+004 exhibited slow variations in radio intensity over the entire period of observations. The appearance of new components in the cores of most objects in the table should apparently be expected; these components can be revealed by VLBI observations.

REFERENCES

1. I. I. Kellermann and I. I. K. Pauliny-Toth, Ann. Rev. Astron. Astrophys. **19**, 373 (1981).
2. E. Salonen, H. Terasranta, S. Urpo, *et al.*, Astron. Astrophys., Suppl. Ser. **79**, 409 (1987).
3. I. A. Strukov and D. P. Skulachev, *Itogi Nauki i Tekhniki, Ser. Astronomiya* (VINITI, Moscow, 1986), Vol. 31, p. 37.
4. V. A. Efanov, I. G. Moiseev, and N. S. Nesterov, Izv. Krym. Astrofiz. Obs. **60**, 3 (1979).
5. I. G. Moiseev and N. S. Nesterov, Izv. Krym. Astrofiz. Obs. **73**, 154 (1985).

Translated by V. Astakhov

Astronomy Letters, Vol. 26, No. 4, 2000, pp. 208–218. Translated from Pis'ma v Astronomicheskiĭ Zhurnal, Vol. 26, No. 4, 2000, pp. 253–265.

On the Internal Structure of Relativistic Jets

V. S. Beskin[1]* and L. M. Malyshkin[2]

[1] *Lebedev Physical Institute, Russian Academy of Sciences, Leninskiĭ pr. 53, Moscow, 117924 Russia*
[2] *Princeton University Observatory, Princeton, USA*

Received February 19, 1999; in final form, October 1, 1999

Abstract—A magnetohydrodynamic model is constructed for a cylindrical jet embedded in an external uniform magnetic field. It is shown that, as in the force-free case, the total electric current within the jet can be zero. The particle energetics and the magnetic-field structure are determined in a self-consistent way; all jet parameters depend markedly on the physical conditions in the external medium. In particular, we show that a region with subsonic flow can exist in the central jet regions. In real relativistic jets, most of the energy is transferred by the electromagnetic field only at a sufficiently large magnetization parameter $\sigma > 10^6$. We also show that, in general, the well-known solution with a central core $B_z = B_0/(1 + \varpi^2/\varpi_c^2)$ cannot be realized in the presence of an external medium. © *2000 MAIK "Nauka/Interperiodica".*

Key words: *accretion, jet theory and stellar wind*

1. INTRODUCTION

The formation mechanism of jets is a key issue in the study of the magnetospheric structure of compact astrophysical objects. Indeed, jets are observed in most compact sources, ranging from active galactic nuclei (AGNs), quasars, and radio galaxies [1] to accreting neutron stars, solar-mass black holes (SS 433, X-ray novae) [2], and young stellar objects [3]. Moreover, jets have also been recently discovered in young radio pulsars [4, 5]. At the same time, in most studies devoted to the magnetohydrodynamic (MHD) model of such objects [6–11], in which the formation of jets is associated with the attraction of longitudinal currents flowing in the magnetosphere, attention was focused on intrinsic collimation in the sense that the effect of the external medium was assumed to be marginal. However, such a situation is possible only for a nonzero total current I flowing within the jet [12], so the question of its closure in the outer parts of the magnetosphere arises. On the other hand, the longitudinal current is often constrained by the regularity condition at the fast magnetosonic surface, which by no means always leads to the sufficiently large longitudinal currents required for collimation [13]. In other words, with the exception of the force-free case [14], as yet no working model of a jet in which, on the one hand, the total electric current would be zero, and, on the other hand, the total magnetic flux Ψ_0 in the jet would be finite, has been constructed. However, the force-free approximation, in which, by definition, the particle energy density is disregarded, does not allow the fraction of energy transferred by the outflowing plasma to be determined.

At the same time, the question of collimation cannot be solved in isolation from the external conditions (see, e.g., [15, 16]. In particular, this is clear even from a popular example of the magnetosphere of a compact object with a monopole magnetic field, because for any arbitrarily weak external regular magnetic field, the monopole solution (for which the magnetic field falls off as r^{-2}) cannot be extended to infinity. Moreover, as is well known from an example of moving cosmic bodies, such as Jupiter's moons [17] or artificial Earth satellites [18, 19], as well as radio pulsars [20], the external magnetic field can serve as an effective transfer link, which occasionally determines overall energy losses of the system. For this reason, constructing a consistent magnetospheric model for compact objects embedded in an external magnetic field is, in our view, of undeniable interest, especially since, as was noted above, such a jet model was previously constructed in the force-free approximation [14].

Undoubtedly, the existence of an external regular magnetic field in the vicinity of compact objects is largely open to question. The regular magnetic field in our Galaxy, i.e., the field that is constant on scales comparable to the sizes of our Galaxy, is known to be

$$B_{\rm ext} \sim 10^{-6}\ {\rm G} \qquad (1)$$

and essentially matches the random magnetic-field component, which varies even on scales of several parsecs [21]. However, if the collimation is assumed to be actually produced by an external magnetic field, it becomes possible to estimate the jet radius. Indeed, assuming the magnetic field in the jet to be similar to

* E-mail address for contacts: beskin@lpi.ru

the external magnetic field (1), we obtain from the condition for the conservation of magnetic flux

$$r_j \sim R\left(\frac{B_{in}}{B_{ext}}\right)^{1/2}, \quad (2)$$

where R and B_{in} are the radius and magnetic field of the compact object, respectively. For example, for AGNs ($B_{in} \sim 10^4$ G, $R \sim 10^{13}$ cm), we have

$$r_j \sim 1 \text{ pc}, \quad (3)$$

which corresponds to the observed jet radii [1]. One might expect such a picture to also hold for an external medium with pressure $P \sim B^2/8\pi$; therefore, it seems of interest to consider the internal structure of a one-dimensional jet embedded in an external uniform magnetic field. However, a discussion of the more realistic case of a medium with pressure is beyond the scope of this study. Nor do we discuss the collimation itself, but only consider the internal structure of observed one-dimensional jets. This issue has become particularly urgent because of the new possibilities offered by space radio interferometry, which enables the internal structure of such jets to be resolved. The effect of an external medium on the internal structure of relativistic jets in the MHD model discussed here was previously studied only by Appl and Camenzind [15, 16]. They considered only a special case with a constant angular velocity of the plasma, in which the solution with a zero total electric field flowing inside the jet could not be constructed. As we show below, it is for the case of an angular velocity decreasing toward the jet periphery (which, incidentally, is typical of all models with a magnetic field passing through the accretion disk) that the solution with finite magnetic flux Ψ_0 and zero total current $I(\Psi_0) = 0$ can be constructed.

On the other hand, many authors [22–25] obtained a universal solution with a central core for a cylindrical jet:

$$B_z = \frac{B_0}{1 + \varpi^2/\varpi_c^2}, \quad (4)$$

where, in the relativistic case,

$$\varpi_c = \frac{c\gamma}{\Omega} \quad (5)$$

is the size of the central core, Ω is the angular velocity of the compact object, and γ is the characteristic Lorentz factor of the outflowing plasma. As can be easily seen, such a solution results in a rapid falloff of the poloidal field $B_z \propto \varpi^{-2}$ far from the rotation axis $\varpi \gg \varpi_c$. However, this solution is in conflict with the force-free approximation, in which the poloidal magnetic field remains essentially constant [14]. Indeed, when the energy density of the electromagnetic field exceeds appreciably the plasma energy density (and it is this case that was considered), it would be natural to assume that the internal jet structure must be similar to the force-free one.

The examples given above show that a more detailed study with allowance for all possible solutions, is required even in the simplest case of a one-dimensional cylindrical jet considered in terms of ideal magnetohydrodynamics. Our study aims at a consistent investigation of this issue.

Several features that we use when studying the structure of relativistic jets typical of AGNs and radio pulsars should be immediately noted. First of all, the jet radius r_j in all real cases proves to be considerably larger than the light-cylinder radius $R_L = c/\Omega$. This implies that, when the internal structure of jets is investigated, the corresponding equations must be written in complete relativistic form. On the other hand, the gravitational forces can be disregarded in them far from the compact object. Finally, for simplicity, we consider below a cold plasma, which is justifiable because thermal processes in the magnetospheres of radio pulsars play no crucial role. As for the jets from AGNs, this approximation is applicable here in those magnetospheric regions in which the plasma density is low. In any case, this is true for the field lines passing through the surface of a black hole.

The one-dimensional solutions describing collimated jets are obtained in Sect. 2; analytic and numerical solutions for the basic physical quantities characterizing the structure and physics of jets are given in Sect. 3. The problem is solved in straightforward statement; i.e., all jets characteristics are determined by a set of parameters in the compact source and, most importantly, by the physical conditions in the external medium. As a result, we have found the conditions under which most of the energy in real relativistic jets must be transferred by the electromagnetic field, while a region with subsonic flow exists in the central jet regions. We also show that the solution with a central core (4) and (5) cannot be realized in an external magnetic field. Finally, some astrophysical implications of the theory developed for one-dimensional jets are discussed in Sect. 4.

2. BASIC EQUATIONS

Let us consider the structure of a one-dimensional jet where all quantities depend only on radius ϖ; in what follows, the temperature of the matter is assumed to be zero, and $c = 1$. As in the general axisymmetric case, it is convenient to describe the magnetic-field structure in terms of magnetic-flux function $\Psi(\varpi)$, which is related to the longitudinal magnetic field by

$$B_z(\varpi) = \frac{1}{2\pi\varpi}\frac{d\Psi}{d\varpi}. \quad (6)$$

Accordingly, it is convenient to write the toroidal magnetic field, the electric field, and the 4-velocity vector of the matter as

$$B_\varphi(\varpi) = -\frac{2I}{\varpi}, \quad (7)$$

$$\mathbf{E} = -\frac{\Omega_F}{2\pi}\frac{d\Psi}{d\varpi}\mathbf{e}_\varpi, \quad (8)$$

$$\mathbf{u} = \frac{\eta}{n}\mathbf{B} + \gamma\Omega_F\varpi\mathbf{e}_\varphi, \quad (9)$$

where $I(\varpi_0)$ is the total current within $\varpi < \varpi_0$. In the case of a cold plasma at cylindrical Ψ = const magnetic surfaces, four "integrals of motion" [26] can be introduced, which should be considered precisely as functions of magnetic flux Ψ in the most general statement. These are primarily $\Omega_F(\Psi)$ and $\eta(\Psi)$ in the definitions (8) and (9), as well as the z component of angular momentum $L(\Psi) = I/2\pi + \mu\eta\varpi u_\varphi$ and the energy flux $E(\Psi) = \Omega_F I/2\pi + \gamma\mu\eta$. Here, μ is the relativistic specific enthalpy, which is equal to the mass of particles for a cold plasma. The specific form of the integrals of motion must be determined from boundary conditions in the compact source and from critical conditions at singular surfaces.

As a result, the trans-field equation for magnetic surfaces far from gravitating bodies (Grad–Shafranov equation) can be written as (see, e.g., [27])

$$\frac{1}{\varpi}\frac{d}{d\varpi}\left(\frac{A}{\varpi}\frac{d\Psi}{d\varpi}\right) + \Omega_F(\nabla\Psi)^2\frac{d\Omega_F}{d\Psi} + \frac{64\pi^4}{\varpi^2}\frac{1}{2M^2}\frac{d}{d\Psi}\left(\frac{G}{A}\right) - \frac{32\pi^4}{M^2}\frac{d(\mu^2\eta^2)}{d\Psi} = 0, \quad (10)$$

where

$$G = \varpi^2 e^2 + M^2 L^2 - M^2\varpi^2 E^2,$$

$$A = 1 - \Omega_F^2\varpi^2 - M^2,$$

$$e(\Psi) = E(\Psi) - \Omega_F(\Psi)L(\Psi).$$

Here, $M^2 = \mathbf{u}_p^2/\mathbf{u}_a^2 = 4\pi\eta^2/n$ is the square of the Mach number with respect to the Alfven velocity $u_a = B_z/(4\pi n\mu)^{1/2}$, and the derivative $d/d\Psi$ acts only on the integrals of motion. The remaining jet parameters are given by well-known algebraic relations (see, e.g., [27]):

$$\frac{I}{2\pi} = \frac{L - \Omega_F\varpi^2 E}{1 - \Omega_F^2\varpi^2 - M^2}, \quad (11)$$

$$\gamma = \frac{1}{\mu\eta}\frac{(E - \Omega_F L) - M^2 E}{1 - \Omega_F^2\varpi^2 - M^2}, \quad (12)$$

$$u_\varphi = \frac{1}{\varpi\mu\eta}\frac{(E - \Omega_F L)\Omega_F\varpi^2 - LM^2}{1 - \Omega_F^2\varpi^2 - M^2}. \quad (13)$$

Equation (10) contains four integrals of motion; this equation has no singularity at the fast magnetosonic surface, because it depends only on coordinate ϖ. As for the Alfven $A = 0$ surface, this question generally requires a further study outside the province of ideal magnetohydrodynamics. At the same time, for the fairly large currents $I \approx I_{GJ}$ considered here, this surface can also be always passed via a small change in the integrals of motion near the Alfven $\Psi \approx \Psi_A$ surface. Consequently, equation (10) requires six boundary conditions. These boundary conditions primarily include the external uniform magnetic field

$$B_z(r_j) = B_{ext}, \quad (14)$$

and the regularity condition at the magnetic axis $\varpi \longrightarrow 0$

$$\Psi(\varpi) \longrightarrow C\varpi^2. \quad (15)$$

In addition, all four integrals Ω_F, E, L, and η must be specified. As for the remaining quantities characterizing the flow, such, for example, as the jet radius r_j and the outflowing-plasma energy, they must be determined as a solution to the problem formulated above. Similarly, the solution of the problem must also give an answer to the question of whether the flow in the jet is supersonic.

Let us now consider the determination of the integrals of motion in more detail. It would be natural to assume that, at the jet boundary where there is no longitudinal motion of the matter, all four integrals of motion become zero

$$\Omega_F(\Psi_0) = 0, \quad E(\Psi_0) = 0, \quad L(\Psi_0) = 0, \quad \eta(\Psi_0) = 0, \quad (16)$$

where Ψ_0 is the finite total magnetic flux concentrated in the jet. This case corresponds to the absence of tangential discontinuities at the jet boundary; according to (11), the total electric current within the jet is automatically equal to zero.

We use the integrals of motion $\Omega_F(\Psi)$, $L(\Psi) = I(\Psi)/2\pi$, and $E(\Psi) = \Omega_F(\Psi)L(\Psi)$ derived by Beskin *et al.* [28] for the force-free magnetosphere of a black hole, which satisfy the conditions (16) and, consequently, can be directly used to study the jet structure. The only, but, as we show below, very important refinement here is the fact that, at finite magnetization parameter σ [29],

$$\sigma = \frac{\Omega_F^2(0)}{8\pi^2}\frac{\Psi_0}{\mu\eta(0)}, \quad (17)$$

which tends to infinity in the force-free approximation, the particle contribution must be added to the energy integral $E(\Psi)$, because the energy flux of the electromagnetic field near the rotation axis must inevitably vanish. As a result, we have, to within terms $\sim\sigma^{-1}$,

$$\Omega_F(\Psi) = \frac{2\sqrt{1 - \Psi/\Psi_0}}{1 + \sqrt{1 - \Psi/\Psi_0}}\Omega_F(0), \quad (18)$$

$$L(\Psi) = \frac{1}{2\pi^2}\frac{\sqrt{1 - \Psi/\Psi_0}}{1 + \sqrt{1 - \Psi/\Psi_0}}\Omega_F(0)\Psi, \quad (19)$$

$$E(\Psi) = \gamma_{in}\mu\eta + \Omega_F(\Psi)L(\Psi); \quad (20)$$

below, we assume, for simplicity, that

$$\gamma_{in} = \text{const}. \quad (21)$$

We emphasize that γ_{in} in expression (20) has the meaning of Lorentz factor for injection in the region of the compact object and does not match the Lorentz factor of the jet particles.

Thus, we see from the formula for the energy flux $E(\Psi)$ that the contribution of the electromagnetic field becomes dominant only at $\Psi > \Psi_{in}$, where

$$\Psi_{in} = \frac{\gamma_{in}}{\sigma}\Psi_0. \quad (22)$$

At low values of Ψ, most of the energy is transferred by relativistic particles; as directly follows from relation (20), their Lorentz factor is constant and equal to their initial value γ_{in}. As for the integral $\eta(\Psi)$, the particle-to-magnetic flux ratio, we chose it in the form

$$\eta(\Psi) = \eta_0(1 - \Psi/\Psi_0), \quad (23)$$

which satisfies the condition (16)

We emphasize that the very possibility of using the integrals of motion obtained when analyzing the inner magnetospheric regions is not trivial. Indeed, the flow outside the fast magnetosonic surface is completely determined by four boundary conditions at the surface of a rotating body. At the same time, a one-dimensional flow can be produced by the interaction with the external medium, which gives rise (see, e.g., [30]) to perturbations or shock waves propagating from "acute angles" and other irregularities. Therefore, in these regions where the conditions for the validity of ideal magnetohydrodynamics are without doubt violated, a significant redistribution of energy E and angular momentum L is possible, let alone the fact that part of them can be lost altogether via radiation. Nevertheless, we assume here, for simplicity, that the integrals of motion $E(\Psi)$ and $L(\Psi)$ as functions of flux Ψ remain exactly the same as those in the inner magnetospheric regions.

In the one-dimensional case we consider, it is convenient to immediately reduce the second-order equation (10) to a set of two first-order equations for $\Psi(\varpi)$ and $M^2(\varpi)$. Multiplying equation (10) by $2A(d\Psi/d\varpi)$ yields

$$\frac{d}{d\varpi}\left[\frac{A^2}{\varpi^2}\left(\frac{d\Psi}{d\varpi}\right)^2\right] + A\left(\frac{d\Psi}{d\varpi}\right)^2\frac{d'\Omega_F^2}{d\varpi} + \frac{64\pi^4 A}{\varpi^2 M^2}\frac{d'}{d\varpi}\left(\frac{G}{A}\right) - \frac{64\pi^4 A}{M^2}\frac{d}{d\varpi}(\mu^2\eta^2) = 0, \quad (24)$$

with the derivative $d'/d\varpi$ acting only on the integrals of motion. Finally, we use "Bernoulli's relativistic equation" $\gamma^2 - \mathbf{u}^2 = 1$, which, given the definitions of the integrals of motion $E(\Psi)$ and $L(\Psi)$, can be written as

$$A^2\left(\frac{dy}{dx}\right)^2 = \frac{e^2}{\mu^2\eta^2}\frac{x^2(A - M^2)}{M^4} + \frac{x^2E^2}{\mu^2\eta^2} - \frac{\Omega_F^2(0)L^2}{\mu^2\eta^2} - \frac{x^2A^2}{M^4}, \quad (25)$$

where we introduced the dimensionless variables

$$x = \Omega_F(0)\varpi = \Omega\varpi, \quad (26)$$

$$y = \sigma\Psi/\Psi_0. \quad (27)$$

As a result, substituting the right-hand part of (25) in the first term of (24) and performing simple differentiation yield

$$\left[\frac{e^2}{\mu^2\eta^2} + \frac{\Omega_F^2}{\Omega_F^2(0)}x^2 - 1\right]\frac{dM^2}{dx} = \frac{M^6}{x^3A}\frac{\Omega_F^2(0)L^2}{\mu^2\eta^2} - \frac{xM^2}{A}\frac{\Omega_F^2}{\Omega_F^2(0)}\left(\frac{e^2}{\mu^2\eta^2} - 2A\right) + \frac{M^2}{2}\frac{dy}{dx} \times \left[\frac{1}{\mu^2\eta^2}\frac{de^2}{dy} + \frac{x^2}{\Omega_F^2(0)}\frac{d\Omega_F^2}{dy} - 2\left(1 - \frac{\Omega_F^2}{\Omega_F^2(0)}x^2\right)\frac{1}{\eta}\frac{d\eta}{dy}\right]. \quad (28)$$

The second equation is Bernoulli's equation (25), which should now be considered as an equation for the derivative dy/dx. The set of equations (25) and (28) allows a general solution to be constructed for a one-dimensional jet embedded in an external magnetic field.

We emphasize one important advantage of the set of first-order equations (25) and (28) over the initial second-order equation (10). The point is that the relativistic equation (10), which is basically the force balance equation, contains the electromagnetic force

$$\mathbf{F}_{em} = \rho_e\mathbf{E} + \mathbf{j}\times\mathbf{B}, \quad (29)$$

in which the electric and magnetic contributions virtually cancel each other out far from the rotation axis $\varpi \gg R_L$. Using Bernoulli's equation (25), we can derive [31]

$$\frac{|\rho_e\mathbf{E} + \mathbf{j}\times\mathbf{B}|}{|\mathbf{j}\times\mathbf{B}|} \sim \frac{1}{\gamma^2}. \quad (30)$$

When analyzing (10), we therefore have to retain all terms of a higher order of smallness $\sim\gamma^{-2}$, while the zero-order quantities $\rho_e\mathbf{E}$ and $\mathbf{j}\times\mathbf{B}$ in (28) are analytically removed using Bernoulli's equation, so all terms of this equation have the same order of smallness.

Finally, it is also important that the exact equation (28) has no singularity near the rotation axis. In other words, its solution contains no δ-shaped current $I \propto \delta(\varpi)$ flowing along the jet axis; several authors pointed to the need for its introduction [7, 32].

3. EXACT SOLUTIONS AND NUMERICAL RESULTS

Let us consider the basic properties of the set of equations (25) and (28). As can be easily verified, in the relativistic case under consideration, we may assume $\gamma = u_z$ for a high-accuracy estimate. Far from the rotation axis $x \gg \gamma_{in}$ ($\varpi \gg \gamma_{in} R_L$), equation (25) for $M^2 \ll x^2$ can then be rewritten in general form as

$$\frac{d\Psi}{d\varpi} = \frac{8\pi^2 E(\Psi)}{\varpi \Omega_F^2(\Psi)} \tag{31}$$

or, equivalently,

$$B_z(\varpi) = \frac{4\pi E(\Psi)}{\varpi^2 \Omega_F^2(\Psi)}. \tag{32}$$

As we see, equation (31) does not contain M^2 at all and can therefore be integrated independently. This must be the case, because equation (31) must coincide with the asymptotics of the force-free equation, which is derived from (25) by passing to the limit $M^2 \longrightarrow 0$. Assuming now that $B_z(r_j) = B_{ext}$ in (32), we obtain, in particular, for the jet radius

$$r_j^2 = \lim_{\Psi \to \Psi_0} \frac{4\pi E(\Psi)}{\Omega_F^2(\Psi) B_{ext}}. \tag{33}$$

Consequently, the jet radius is determined by the limit of the $E(\Psi)/\Omega_F^2(\Psi)$ ratio as $\Psi \longrightarrow \Psi_0$. In particular, for $E(\Psi)$ and $\Omega_F(\Psi)$ given by (18)–(20), we have

$$\lim_{\Psi \to \Psi_0} \frac{E(\Psi)}{\Omega_F^2(\Psi)} = \frac{1}{4\pi^2}\Psi_0, \tag{34}$$

so the limit (33) actually exists. As a result, we obtain

$$r_j = \sqrt{\frac{\Psi_0}{\pi B_{ext}}}, \tag{35}$$

which essentially matches the estimate (2). This is no surprise, because we show below that equations (25) and (28) for the integrals of motion (18)–(20), and (23) have a constant magnetic field as their solution over a wide range of ϖ.

Let us now consider in more detail the behavior of the solution in the inner jet region, where $\Psi \ll \Psi_0$ and, hence, the integrals of motion can be written with sufficient accuracy as

$$L(\Psi) = \frac{\Omega_F}{4\pi^2}\Psi, \tag{36}$$

$$\Omega_F(\Psi) = \Omega = \text{const}, \tag{37}$$

$$\eta(\Psi) = \eta_0 = \text{const}, \tag{38}$$

with $E(\Psi) = \gamma_{in}\mu\eta_0 + \Omega_F L$ and $e = \gamma_{in}\mu\eta_0 = \text{const}$. As a result, $\Omega_F L/\mu\eta_0 = 2y$, and we can rewrite equations (25) and (28) as

$$(1 - x^2 - M^2)^2\left(\frac{dy}{dx}\right)^2 = \frac{\gamma_{in}^2 x^2}{M^4}(1 - x^2 - 2M^2) + x^2(\gamma_{in} + 2y)^2 - 4y^2 - \frac{x^2}{M^4}(1 - x^2 - M^2)^2, \tag{39}$$

$$(\gamma_{in}^2 + x^2 - 1)\frac{dM^2}{dx} = 2xM^2 - \frac{\gamma_{in}^2 x M^2}{(1 - x^2 - M^2)} + \frac{4y^2 M^6}{x^3(1 - x^2 - M^2)}. \tag{40}$$

Equations (39) and (40) describing the internal jet structure can be solved analytically. It can be verified by direct substitution that we have the following asymptotics for $x \ll \gamma_{in}$:

$$M^2(x) = M_0^2 = \text{const}, \tag{41}$$

$$y(x) = \frac{\gamma_{in}}{2M_0^2}x^2, \tag{42}$$

which corresponds to a constant magnetic field

$$B_z = B_z(0) = \frac{4\pi\gamma_{in}\mu\eta_0}{M_0^2} = \frac{\gamma_{in}}{\sigma M_0^2}B(R_L) = \text{const}, \tag{43}$$

where $B(R_L) \approx \Psi_0/R_L^2$. Here, we assume that $\gamma_{in} \gg 1$, typical of the jets from AGNs and radio pulsars.

The solution of (39) and (40) for $x \gg \gamma_{in}$, i.e., at $\varpi \gg \gamma_{in} R_L$, depends markedly on the relationship between γ_{in} and $M_0 = M(0)$. For example, at $M_0^2 > \gamma_{in}^2$, when, according to (43), the axial magnetic field is fairly weak, the total magnetic flux within $\varpi < \gamma_{in} R_L$

$$\Psi(\gamma_{in} R_L) \approx \pi\gamma_{in}^2 R_L^2 B_z(0) \tag{44}$$

can be written as

$$\Psi(\gamma_{in} R_L) \approx \frac{\gamma_{in}^2}{M_0^2}\Psi_{in}, \tag{45}$$

where the flux Ψ_{in} is given by (22). We see that, if the condition $M_0^2 > \gamma_{in}^2$ is satisfied, the total magnetic flux within $\varpi < \gamma_{in} R_L$ is lower than Ψ_{in}; so, outside this region, the particles also make the main contribution to $E(\Psi)$ as before, while the contribution of the electromagnetic field may be disregarded. As a result, at $\varpi \gg \gamma_{in} R_L$, the solution of (39) and (40) yields a quadratic rise in M^2 and a power-law falloff of the magnetic field [22–24]:

$$M^2(x) = M_0^2 \frac{x^2}{\gamma_{in}^2} \gg x^2, \tag{46}$$

$$B_z(x) = B_z(0)\frac{\gamma_{in}^2}{x^2}. \quad (47)$$

Consequently, the magnetic flux increases very slowly (logarithmically) with distance from the rotation axis:

$$\Psi(x) \propto \ln(x/\gamma_{in}). \quad (48)$$

Such a behavior of the magnetic field, in turn, shows that the transition flux $\Psi = \Psi_{in}$ is reached exponentially far from the rotation axis, in conflict with the estimate (2) corresponding to the assumption of jet collimation.

We may thus conclude that an external constant magnetic field limits above the Mach number at the rotation axis

$$M^2(0) < M_{max}^2 = \gamma_{in}^2. \quad (49)$$

Accordingly, as follows from (43), the magnetic field at the rotation axis cannot be weaker than

$$B_{min} = \frac{1}{\sigma\gamma_{in}}B(R_L). \quad (50)$$

If, however, the Mach number at the rotation axis does not exceed γ_{in}, then, as for the similar asymptotics $\varpi \ll \gamma_{in}R_L$, the solution of (39) and (40) for $\gamma_{in}R_L \ll \varpi \ll r_j$ gives the constant magnetic field (43), which corresponds to

$$y(x) = \frac{\gamma_{in}}{2M_0^2}x^2. \quad (51)$$

At the same time, in this case, we have only a linear increase in the square of the Mach number

$$M^2(x) = M_0^2\frac{x}{\gamma_{in}} \ll x^2. \quad (52)$$

According to (27) and (51), the jet radius can be written as

$$r_j = \sqrt{\frac{\sigma M_0^2}{\gamma_{in}}}R_L, \quad (53)$$

which is equivalent to (35). Moreover, as can be easily verified, the constant magnetic field $B_z = B(0)$ for the invariants (18)–(20) proves to be an exact solution to (31), and $\varpi = r_j$ in the entire jet up to the jet boundary. Here, we may therefore assume $B(0) = B_{ext}$. Consequently, according to (43), we obtain

$$M_0^2 = \frac{\gamma_{in}}{\sigma}\frac{B(R_L)}{B_{ext}}. \quad (54)$$

Using relation (54), we can also express all the remaining jet parameters in terms of the external magnetic field.

Note that the absence of a declining solution $B_z \propto \varpi^{-2}$ [see (4)] is associated with the first term on the right-hand side of (28) proportional to L^2. This term, which changes appreciably the behavior of the solution, appears to have been missed previously. As was already emphasized above, this is no surprise when we analyze the second-order equation (10) in which the corresponding term is small. On the other hand, far from the rotation axis $\varpi \gg \gamma_{in}R_L$, equation (28) can be rewritten as

$$\frac{d}{dx}\left[\frac{\mu\eta\Omega_F x^2}{M^2}\right] + \frac{\Omega_F^4(0)M^2}{\Omega_F\mu\eta x^3(x^2+M^2)}L^2 = 0, \quad (55)$$

in which both terms have the same order of smallness. Disregarding now the term proportional to L^2, we arrive at the solution (46) $M^2 \propto x^2$ for Ω_F = const and η = const. The conservation of

$$H = \frac{\mu\eta\Omega_F x^2}{M^2} \quad (56)$$

was first found by Heyvaerts and Norman [7] for conical solutions, when all quantities depend only on spherical coordinate θ, but has also been repeatedly discussed when analyzing cylindrical flows. However, as we see, H is generally not conserved in the cylindrical geometry for relativistic jets. To be more precise, the second term in (55) turns out to be significant for all models with a nearly constant density of the longitudinal electric current in the central jet region, when the invariant $L(\Psi)$ for $\Psi \ll \Psi_0$ linearly increases with magnetic flux Ψ.

Thus, we conclude that the solution with a central core (4) cannot be realized in the presence of an external medium—a finite regular magnetic field. This conclusion appears to be also valid in the presence of a medium with finite pressure P. Indeed, since the magnetic flux (48) increases very slowly (logarithmically), the solution (4) yields an exponentially large jet radius $r_j \sim R_L\exp(\Psi_0/\Psi_{in})$. Accordingly, the magnetic energy density must also be low at $\varpi \sim r_j$. However, this configuration cannot exist in the presence of an external medium with finite pressure P, irrespective of whether it is produced by a magnetic field or a plasma. We may therefore conclude that the solutions with a central core can be realized only for a special choice of the integral $L(\Psi)$, which increases only slightly with magnetic flux, and only in the absence of an external medium. For the most natural (from our point of view) models with a constant current density in the central jet regions, the solution with a central core cannot be realized even in the absence of an external medium.

In order to derive now the energy distribution in the jet and the particle Lorentz factor, it is convenient to introduce the quantity

$$g(x) = \frac{M^2}{x^2}. \quad (57)$$

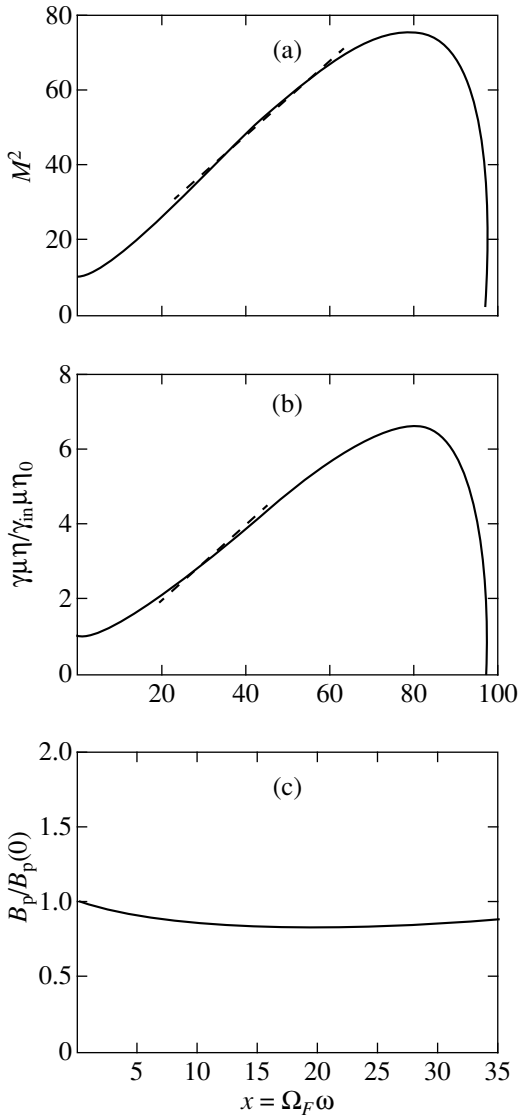

Fig. 1. The dependences of Mach number M^2 (a), energy flux $\gamma\mu\eta$ concentrated in particles (b), and poloidal magnetic field B_z (c) derived by numerically integrating equations (25) and (28) for $M_0^2 = 16$, $\gamma_{in} = 8$, and $\sigma = 1000$. The dashed lines indicate the behavior of these quantities that follows from analytic asymptotics.

Since at large distances $\varpi \gg \gamma_{in}R_L$, according to (12), we have

$$\frac{\gamma\mu\eta}{E} = \frac{g}{g+1}, \tag{58}$$

g is simply the ratio of the energy flux transferred by particles W_{part} to the energy flux of the electromagnetic field. As a result, from relation (52) for $x \gg \gamma_{in}$, we obtain

$$\frac{W_{part}}{W_{tot}} \approx \frac{M_0^2}{\gamma_{in}}x^{-1} \ll 1. \tag{59}$$

Accordingly, from (57) and (58) for the particle Lorentz factor at $x \gg \gamma_{in}$, we derive

$$\gamma(x) = x. \tag{60}$$

Finally, expression (13) for the 4-velocity vector u_φ yields the following toroidal velocity $v_\varphi = u_\varphi/\gamma$ at $x \gg \gamma_{in}$:

$$v_\varphi(x) = \frac{1}{x}. \tag{61}$$

We see that the particle energy approaches the universal asymptotic limit (60) at $\varpi \gg \gamma_{in}R_L$. Naturally, such a simple asymptotics can also be derived from simpler considerations. Indeed, using the frozen-in equation $\mathbf{E} + \mathbf{v} \times \mathbf{B} = 0$, we obtain for the drift velocity

$$U_{dr}^2 = \frac{|\mathbf{E}|^2}{|\mathbf{B}|^2} = \left(\frac{B_\varphi^2}{|\mathbf{E}|^2} + \frac{B_z^2}{|\mathbf{E}|^2}\right)^{-1}. \tag{62}$$

In our case, however, according to (6) and (7), we have

$$B_\varphi^2 \approx |\mathbf{E}|^2. \tag{63}$$

$$|\mathbf{E}|^2 \approx x^2 B_z^2. \tag{64}$$

As a result, relations (62)–(64) immediately lead to the exact asymptotics (60). It thus follows that, for example, for electron–positron jets from AGNs, the jet particle energy is typically

$$E \approx m_e c^2 \frac{r_j}{R_L} \sim (10^4\text{–}10^5)\ \text{MeV}. \tag{65}$$

On the other hand, according to (57), we reach a very important conclusion that, for large enough σ far from the light cylinder,

$$g \ll 1. \tag{66}$$

Consequently, according to (58), the particle contribution to the general energy flux balance proves to be minor. For example, at $B_{ext} \sim B_{min}$ for $r \sim r_j$, we have

$$\frac{W_{part}}{W_{tot}} \sim \sqrt{\frac{\gamma_{in}}{\sigma}}, \tag{67}$$

while in the general case, we obtain

$$\frac{W_{part}}{W_{tot}} \sim \frac{1}{\sigma}\left[\frac{B(R_L)}{B_{ext}}\right]^{1/2}. \tag{68}$$

Thus, we reach a fairly nontrivial conclusion that the fraction of energy transferred by particles in a one-dimensional jet must be determined by the parameters of the external medium.

Let us now discuss the results of exact calculations obtained by numerically integrating equations (25) and (28) for the integrals of motion (18)–(20) and (23). In Figs. 1a and 1b, the Mach number and the energy flux concentrated in particles $\gamma\mu\eta$ are plotted against x for $M_0^2 = 16$, $\gamma_{in} = 8$, and $\sigma = 1000$. The dashed lines indi-

cate the behavior of these quantities that follows from the analytic asymptotics (52) and (60). As we see, at sufficiently small x, when the integrals of motion (18)–(20) and (23) are similar to (36)–(38), the analytic expressions match their exact values. On the other hand, as expected, $\gamma\mu\eta$ and M^2 are zero at $\Psi = \Psi_0$, i.e., at the jet edge. Figure 1c shows the dependence of poloidal field $x^{-1}dy/dx$ for the inner parts of the jet, $\Psi < \Psi_0$. We see from this figure that the magnetic field is nearly constant at $x > \gamma_{in}$, in agreement with the analytic estimates (43) and (51). Of course, the structure of the poloidal magnetic field is generally determined by the specific choice of integrals $E(\Psi)$ and $L(\Psi)$.

In conclusion, it is of interest to compare the jet particle energy with the limiting energy acquired by the particles as they outflow from the magnetosphere of a compact object with a monopole magnetic field. According to [33], the particle Lorentz factor outside the fast magnetosonic surface $r > \sigma^{1/3}R_L$ in the absence of an external medium can be written as

$$\gamma(y) = y^{1/3}, \quad y > \gamma_{in}^3, \tag{69}$$

$$\gamma(y) = \gamma_{in}, \quad y < \gamma_{in}^3, \tag{70}$$

where y is given by (27). On the other hand, relations (51) and (60) for the jet yield

$$\gamma(y) = \left(\frac{M_0^2}{\gamma_{in}}\right)^{1/2} y^{1/2}, \quad y > \frac{\gamma_{in}^3}{M_0^2}, \tag{71}$$

$$\gamma(y) = \gamma_{in}, \quad y < \frac{\gamma_{in}^3}{M_0^2}. \tag{72}$$

As shown in Fig. 2a, for $M_0^2 > 1$, i.e., for $B_{ext} < B_{cr}$, where

$$B_{cr} = \frac{\gamma_{in}}{\sigma} B(R_L), \tag{73}$$

the Lorentz factor of the jet particles (71) is always larger than the Lorentz factor acquired by the particles as they outflow from a magnetosphere with a monopole magnetic field, but, of course, is always smaller than the critical Lorentz factor

$$\gamma_{in} = y, \tag{74}$$

which corresponds to complete transformation of the electromagnetic energy into the particle energy. This implies that, at $B_{ext} < B_{cr}$, the particles must be additionally accelerated during the collimation coupled with the interaction of the outflowing plasma with the external medium. If, alternatively, $B_{ext} > B_{cr}$, then, in the inner jet regions at

$$\varpi < \frac{\gamma_{in}}{M_0^2} R_L \tag{75}$$

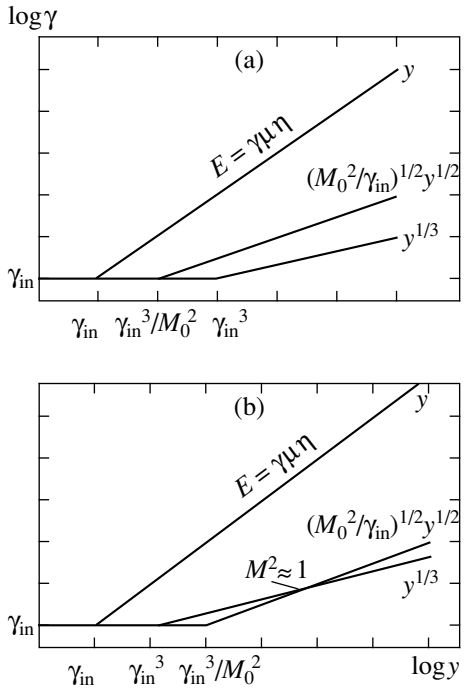

Fig. 2. Logarithmic dependence of the particle Lorentz factor on magnetic flux for a monopole field $\gamma \sim y^{1/3}$, for a one-dimensional jet $\gamma \sim (M_0^2/\gamma_{in})^{1/2} y^{1/2}$, and for complete transformation of the electromagnetic energy into the particle energy $\gamma \sim y$ at (a) $M_0^2 > 1$ ($B_{ext} < B_{cr}$) and (b) $M_0^2 < 1$ ($B_{ext} > B_{cr}$). The intersection of the straight lines ($M^2 \approx 1$) determines the position of the fast MHD point.

the particle energy on a given field line turns out to be even lower than that for a monopole magnetic field, as shown in Fig. 2b.

The latter result can be easily explained. Indeed, for the integrals of motion (36)–(38) we consider, the factor D, whose zero value determines the location of the fast MHD surface (see [27] for more detail), can be rewritten in the case of a cold plasma as

$$M^2 D \equiv A + \frac{B_\varphi^2}{B_p^2} = A + \frac{4x^2y^2M^4}{4y^2M^4 - 2x^2M^2 - x^4}. \tag{76}$$

It is easy to show that expression (76) for y and M^2 given by (51) and (52) becomes negative at

$$M^2 \sim 1, \tag{77}$$

i.e., at x corresponding to (75). Consequently, we may reach yet another important conclusion that, for sufficiently strong external magnetic fields $B_{ext} > B_{cr}$ (73) when $M_0^2 < 1$, a region with subsonic flow inevitably emerges in the inner jet regions $\varpi < r_s$ where

$$r_s \approx \sigma\left[\frac{B_{ext}}{B(R_L)}\right]^{3/2} R_L. \quad (78)$$

At the same time, a region with subsonic flow can be produced far from the compact object either by a shock wave or by a strong distortion of the magnetic field within the fast magnetosonic surface located in the vicinity of the compact object. In both cases, the magnetic-field perturbation causes the particle energy to decrease.

4. DISCUSSION

Thus, we conclude that the exact equations (25) and (28) actually allow a self-consistent model to be constructed for a jet embedded in an external uniform magnetic field. Their advantage over equation (10) stems from the fact that all terms in (28) are of the same order of smallness. In this case, the uniformity of the poloidal magnetic field within the jet (43) results from the choice of integrals (36)–(38). In general, the poloidal magnetic field depends on the specific form of the integrals. A full analysis of possible solutions is beyond the scope of this study.

We have shown that the fraction of energy transferred by the particles W_{part}/W_{tot} must be largely determined by the parameters of the external medium. In this case, for $\sigma \gg \sigma_{cr}$, where

$$\sigma_{cr} = \left[\frac{B(R_L)}{B_{ext}}\right]^{1/2}, \quad (79)$$

the energy transferred by the particles is only a small fraction of the energy flux W_{em} transferred by the electromagnetic field. Consequently, the jet is strongly magnetized ($W_{part} \ll W_{tot}$) only at sufficiently large σ. If, however, the magnetization parameter does not exceed σ_{cr}, then, in this case, an appreciable part of the energy in the jet is transferred by the particles. This, in turn, implies that a considerable part of the energy must be transferred from the electromagnetic field to the plasma particles during jet collimation. Interestingly, σ_{cr} turns out to be approximately the same both for AGNs and for fast radio pulsars:

$$\sigma_{cr} \approx 10^5–10^6. \quad (80)$$

We have shown that the central part of the jet must be subsonic for sufficiently strong external magnetic fields. Thus, the theory gives direct predictions whose validity can be verified by observations. It should also be noted that the results obtained above are applicable both to electron–positron and to electron–proton jets. Recall, however, that direct evidence that the jets in AGNs are actually electron–positron ones has recently appeared [34, 35].

In our view, an important result is also the assertion that, if the external regular magnetic field is taken into account, the MHD equations allow a self-consistent model to be constructed for a jet with a zero total longitudinal electric current $I(\Psi_0)$. In this case, a uniform magnetic field that matches the external magnetic field can also be a solution for the inner jet regions. As was already emphasized above, the radii of the jets from AGNs can thus be also explained in a natural way. Concurrently, since only a small fraction of the electromagnetic energy is transformed into the particle energy, the energy transfer from the compact object in the region of energy release can be explained as well. At the same time, extending the MHD solution to the jet region requires very high particle energies (~10^4 MeV), which have not yet been recorded. However, a consistent discussion of the outflowing-plasma energy requires a proper allowance for the particle interaction with the surrounding medium (for example, with background radiation), which may cause a significant change in particle energy.

As for the quantitative predictions about the real physical parameters of jets, they, as we showed above, essentially depend only on the following three quantities: magnetization parameter σ (17), Lorentz factor γ_{in} in the generation region, and external magnetic field B_{ext}. In this case, the main uncertainty for electron–positron jets from AGNs ($B_{in} \sim 10^4$ G, $R_{in} \sim 10^{14}$ cm) is contained in the magnetization parameter. Indeed, this quantity depends on the efficiency of pair production in the magnetosphere of a black hole, which, in turn, is determined by the density of hard gamma-ray photons. As a result, if the density of hard gamma-ray photons with energies $E_\gamma > 1$ MeV near a black hole is high enough, then the particles will be produced by direct collisions of photons $\gamma + \gamma \longrightarrow e^+ + e^-$ [36]. This causes an abrupt increase in multiplicity parameter $\lambda = n/n_{GJ} \sim 10^{10}$–$10^{12}$, where $n_{GJ} \approx \Omega B/2\pi ce$ is the characteristic particle density required to screen the longitudinal electric field. Using the well-known estimate (see, e.g., [31])

$$\sigma \sim \frac{\Omega e B_{in} R_{in}^2}{\lambda m_e c^3}, \quad (81)$$

we obtain

$$\sigma \sim 10–10^3, \quad \gamma_{in} \sim 3–10. \quad (82)$$

On the other hand, for low densities of gamma-ray photons, when an electron–positron plasma can be produced only in regions with a nonzero longitudinal electric field equivalent to the outer gap in the magnetospheres of radio pulsars [37, 38], the multiplicity of particle production is fairly small: $\lambda \sim 10$–100. In this case, we obtain

$$\sigma \sim 10^{11}–10^{13}, \quad \gamma_{in} \sim 10. \quad (83)$$

Finally, for fast Crab- or Vela-type radio pulsars ($B_{in} \sim 10^{13}$ G, polar-cap radius $R_{in} \sim 10^5$ cm, and $\lambda = n/n_{GJ} \sim 10^4$) in which jets are observed, we have [31]

$$\sigma \sim 10^6–10^7, \quad \gamma_{in} \sim 10^2–10^3. \quad (84)$$

Relations (82) and (83) show that the properties of the jets from AGNs depend markedly on magnetization parameter σ. For example, according to (79), the jet particles for sources with large $\sigma \sim 10^{12}$ transfer only a small fraction of the energy compared to the electromagnetic flux, so the flow within the jet differs only slightly from a force-free one. In addition, the external magnetic field $B_{ext} \sim 10^{-6}$ G in this case exceeds the critical magnetic field $B_{cr} \sim 10^{-7}$ G. According to (43) and (73), this implies that a subsonic region must exist in the inner regions of such jets. On the other hand, a substantial part of the energy in sources with magnetization parameter $\sigma \sim 100$ during jet collimation must be transferred by plasma particles, and no subsonic region is formed near the rotation axis. As for the fast radio pulsars, $B_{ext} \ll B_{cr}$ for them, so a subsonic region in the central parts of jets is not achieved either. On the other hand, the estimate (79) shows that an appreciable part of the total energy contained in the jet must be coupled with particles.

We emphasize that, since the jet radius (53) for AGNs always exceeds the light-cylinder radius by several orders of magnitude,

$$r_j \sim (10^4 - 10^5) R_L, \tag{85}$$

the toroidal magnetic field B_φ within the jet must exceed the poloidal magnetic field B_p in the same proportion,

$$B_\varphi \approx \frac{r_j}{R_L} B_p \sim (10^4 - 10^5) B_{ext}. \tag{86}$$

Consequently, detection of such a strong toroidal component would be a crucial argument for the picture discussed here. Unfortunately, determination of the actual physical conditions in jets currently involves considerable difficulties. Nevertheless, not only data on the direct detection of such a structure [39], but also evidence for the existence of magnetic fields $B \sim 0.1$ G, closely matching the estimate (36) [34], have recently appeared.

ACKNOWLEDGMENTS

We wish to thank A.V. Gurevich for interest in this study, a useful discussion, and support. We also wish to thank S.V. Bogovalov, L.I. Gurvits, and S.A. Lamzin for fruitful discussions. This study was supported in part by the INTAS grant no. 96-154 and the Russian Foundation for Basic Research (project no. 99-02-17184). L. Malyshkin is also grateful to the International Science Foundation.

REFERENCES

1. M. C. Begelman, R. D. Blandford, and M. J. Rees, Rev. Mod. Phys. **56**, 255 (1984).
2. A. M. Cherepashchuk, Usp. Fiz. Nauk **166**, 809 (1996).
3. C. J. Lada, Ann. Rev. Astron. Astrophys. **23**, 267 (1985).
4. C. B. Markwardt and H. Ögelman, Nature **375**, 40 (1995).
5. J. J. Hester, P. A. Scowen, R. Sankrit, *et al.*, Astrophys. J. **448**, 240 (1995).
6. R. D. Blandford and D. G. Payne, Mon. Not. R. Astron. Soc. **199**, 883 (1982).
7. J. Heyvaerts and J. Norman, Astrophys. J. **347**, 1055 (1989).
8. M. E. Sulkanen and R. V. E. Lovelace, Astrophys. J. **350**, 732 (1990).
9. G. Peletier and R. E. Pudritz, Astrophys. J. **394**, 117 (1992).
10. Zh.-Yu. Li, T. Chiueh, and M. C. Begelman, Astrophys. J. **394**, 459 (1992).
11. C. Sauty and K. Tsinganos, Astron. Astrophys. **287**, 893 (1994).
12. S. Nitta, Mon. Not. R. Astron. Soc. **276**, 825 (1995).
13. A. Tomimatsu, Publ. Astron. Soc. Jpn. **46**, 123 (1994).
14. Ya. N. Istomin and V. I. Pariev, Mon. Not. R. Astron. Soc. **281**, 1 (1996).
15. S. Appl and M. Camenzind, Astron. Astrophys. **256**, 354 (1992).
16. S. Appl and M. Camenzind, Astron. Astrophys. **274**, 699 (1993).
17. V. V. Zheleznyakov, *Radio Emission from the Sun and Planets* (Nauka, Moscow, 1964).
18. Ya. L. Al'pert, A. V. Gurevich, and L. P. Pitaevskiĭ, *Artificial Satellites in a Rarefied Plasma* (Nauka, Moscow, 1964).
19. A. V. Gurevich, A. L. Krylov, and E. N. Fedorov, Zh. Éksp. Teor. Fiz. **75**, 2132 (1978).
20. A. I. Tsygan, Mon. Not. R. Astron. Soc. **292**, 317 (1997).
21. L. S. Marochnik and A. A. Suchkov, *Galaxy* (Nauka, Moscow, 1984).
22. T. Chiueh, Zh.-Yu. Li, and M. C. Begelman, Astrophys. J. **377**, 462 (1991).
23. D. Eichler, Astrophys. J. **419**, 111 (1993).
24. S. V. Bogovalov, Pis'ma Astron. Zh. **21**, 633 (1995) [Astron. Lett. **21**, 565 (1995)].
25. M. Camenzind, *Herbig–Haro Flows and the Birth of Low Mass Stars*, Ed. by B. Reipurth and C. Bertout (Kluwer Academic, Dordrecht, 1997), p. 241.
26. J. Heyvaerts, *Plasma Astrophysics*, Ed. by C. Chiuderi and G. Einaudi (Springer, Berlin, 1996), p. 31.
27. V. S. Beskin and V. I. Pariev, Usp. Fiz. Nauk **163**, 95 (1993).
28. V. S. Beskin, Ya. N. Istomin, and V. I. Pariev, *Extragalactic Radio Sources—From Beams to Jets*, Ed. by J. Roland, H. Sol, and G. Peletier (Cambridge Univ. Press, Cambridge, 1992), p. 45.
29. F. C. Michel, Astrophys. J. **158**, 727 (1969).
30. L. D. Landau and E. M. Lifshitz, *Hydrodynamics* (Nauka, Moscow, 1986).
31. S. V. Bogovalov, Pis'ma Astron. Zh. **24**, 393 (1998) [Astron. Lett. **24**, 321 (1998)].

32. Yu. E. Lyubarskii, Mon. Not. R. Astron. Soc. **285**, 604 (1997).
33. V. S. Beskin, I. V. Kuznetsova, and R. R. Rafikov, Mon. Not. R. Astron. Soc. **299**, 341 (1998).
34. C. S. Reynolds, A. C. Fabian, C. Celotti, and M. J. Rees, Mon. Not. R. Astron. Soc. **283**, 873 (1996).
35. J. F. C. Wardle, D. C. Homan, R. Ojha, and D. H. Roberts, Nature **395**, 457 (1998).
36. R. Swensson, Mon. Not. R. Astron. Soc. **209**, 175 (1984).
37. V. S. Beskin, Ya. N. Istomin, and V. I. Pariev, Pis'ma Astron. Zh. **69**, 1258 (1992).
38. K. Hirotani and I. Okamoto, Astrophys. J. **497**, 563 (1998).
39. D. Gabuzda, A. V. Pushkarev, and T. Cawtorne, Mon. Not. R. Astron. Soc. **307**, 725 (1999).

Translated by V. Astakhov

Astronomy Letters, Vol. 26, No. 4, 2000, pp. 219–224. Translated from Pis'ma v Astronomicheskiĭ Zhurnal, Vol. 26, No. 4, 2000, pp. 266–272.

Photometric Deprojection of Edge-on Galaxies

D. V. Bizyaev*

Sternberg Astronomical Institute, Universitetskiĭ pr. 13, Moscow, 119899 Russia

Received June 1, 1999; in final form, September 24, 1999

Abstract—Photometric deprojection is used to determine the stellar-disk and bulge parameters for several edge-on galaxies from the FGC catalog. The assumption that the galaxies of our sample belonging to the fourth (i.e., lowest) surface-brightness class in the FGC are edge-on, low-surface-brightness (LSB) galaxies is considered. © *2000 MAIK "Nauka/Interperiodica".*

Key wards: *galaxies, structure and photometry of galaxies*

INTRODUCTION

The central brightness μ_0 of the disks in most spiral galaxies varies over a relatively narrow range and is, on the average, $21–22^m$ in the photometric *B* band [1]. However, some of the galaxies have disks with a considerably lower central surface brightness. Such objects were called low-surface-brightness (LSB) galaxies to distinguish them from high-surface-brightness (HSB) galaxies, whose μ_0 do not differ markedly from $21–22^m$. McGaugh [2] suggested a more detailed classification of galaxies depending on μ_0; however, the simple division into LSB and HSB objects is also widely used in the literature.

According to [3–5], the LSB disk galaxies are distinguished by their structure and evolution. The main properties of LSB galaxies include the following: low surface and volume densities of their stellar disks; large disk sizes compared to HSB galaxies; heavy-element underabundance; high gas mass-to-light ratios; a large extent of the rising portion of the rotation curve; and low star-formation rates. In contrast to HSB galaxies, dark halos can play a crucial role in the formation and evolution of LSB galaxies [3, 6].

The fact that there are low-surface-brightness objects among edge-on galaxies is mentioned in the description of the Flat Galaxy Catalogue (hereafter FGC [7]) and by Reshetnikov and Combes [8] (hereafter RC97). Karachentsev *et al.* [9] analyzed radial brightness profiles of 120 flat galaxies and showed some of them to have disks of low central surface brightness. After this paper had already been submitted and returned with the referee's comments, the preprint by Matthews *et al.* [10] with the results of a study of UGC 7321, an edge-on LSB galaxy, appeared in the SISSA database.

Reshetnikov and Combes [11] (hereafter RC96) and RC97 report the results of photometric studies for a number of edge-on galaxies. Several galaxies considered by RC97 were included in the FGC, and their inclinations do not differ significantly from 90°.

In this study, we consider a small sample of galaxies, some of which presumably have disks of low surface brightness. Since edge-on LSB galaxies have not yet been studied in detail, our goal here is to compare the disk and bulge parameters for the LSB and HSB galaxies from our sample. To determine these parameters, we use deprojection, which is based on modeling the surface-brightness distributions for the disks and bulges of edge-on galaxies.

SAMPLE OF GALAXIES

We use the *B*, *V* (Johnson) and *I* (Cousins) images of galaxies obtained on July 21–23, 1993, with the 1.2-m telescope at the Obsertvatoire de Haute Provence (OHP) in France. The observations were performed by Reshetnikov and Combes [11]. The CCD detector, observing conditions, and image calibration were described in more detail by RC96. Reshetnikov kindly provided the galaxy images to the author. Table 1 gives: (1) the objects' names, (2) their distances for the Hubble constant $H = 75$ km s^{-1} Mpc^{-1}, and (3) the FGC surface-brightness classes. Two and four galaxies have high and low surface brightnesses, respectively. One more galaxy, UGC 11132, was not included in the FGC; nevertheless, we performed photometric deprojection for it as well, because its inclination to the plane of the sky is also close to 90°.

We additionally removed cosmic-ray hits from the galaxy images and masked field stars. The galaxy position angles were determined from the condition of maximum axial symmetry.

We measured the total colors of the galaxies within an ellipse with the semimajor axis equal to 0.9 of the

* E-mail address for contacts: dmbiz@sai.msu.su

1063-7737/00/2604-0219$20.00 © 2000 MAIK "Nauka/Interperiodica"

Table 1

UGC	*D*, Mpc	Surface-brightness class
11132	37.9	–
11230	94.7	4
11301	60.0	3
11838	46.3	2
11841	79.9	4
11859	40.2	4
11994	65.0	2

optical radius R_{25} taken from the RC3 catalog [12]. The semiminor axis was assumed to be 0.1 of the semimajor axis, which is close to 1/7, the limiting axial ratio for a galaxy to be included in the FGC.

We computed the *B–V* and *V–I* colors of the galaxies by using calibrations from RC96. The total *B–V* colors uncorrected for extinction in the galaxies themselves differ, on the average, by $0\overset{m}{.}10$ from those in RC97. At the same time, the mean *V–I* color difference is less significant, $0\overset{m}{.}007$. These discrepancies can be explained by different procedures of allowance for the contribution of field stars to the total galaxy color and by the fact that the galaxy colors were determined by RC97 using individual calibration relations for each night, which slightly differ from the average ones in RC96.

UGC 11841 is an exception. For this object, the discrepancies between our results and those of Reshetnikov and Combes are large, $0\overset{m}{.}40$ and $0\overset{m}{.}38$ for *B–V* and *V–I*, respectively. The source of this uncertainty is a bright field star located a mere 8″ from the galaxy center and superimposed on its image.

To determine the *B–V* and *V–I* color indices separately for the galaxy stellar disks, we masked and excluded regions located within two pixels of the galactic plane and regions adjacent to the galaxy center within 1.5 of the optical disk scale. Figure 1 shows the total color indices of the galaxies in comparison with the colors of their disks. The colors were corrected for Galactic extinction using values from the LEDA database (Lyon Observatory). As is evident from the figure, the *B–V* and *V–I* color indices of the stellar disks are, on the average, $0\overset{m}{.}2$ smaller; i.e., they are bluer than the galaxies as a whole. The filled triangles indicate galaxies of the fourth surface-brightness class, and the open triangles indicate objects of the second and third classes, as well as UGC 11132. No systematic differences between the colors of galaxies of different-surface brightness classes are observed. Our sample contains galaxies with disk colors typical both of normal HSB galaxies (see, e.g., [13]) and LSB galaxies with large radial disk scales [14, 15]. The LSB galaxies are generally believed to be bluer. However, according to [16], only the color indices of small LSB galaxies differ significantly from those of HSB galaxies.

PHOTOMETRIC DEPROJECTION OF EDGE-ON GALAXIES

The photometric parameters of the disks and bulges were determined by fitting model components (disk and bulge) to the observed two-dimensional *I* brightness distribution.

The galaxy region used for the fitting was bounded by an ellipse whose major axis was oriented along the previously inferred position angle. The ellipse semiaxes were chosen according to the above criterion ($a \approx 0.9R_{25}$ and $b \approx 0.1a$).

For the model disk, we specified the distribution of volume luminosity density by an exponential law of the form

$$\rho_d(r, z) = \rho_{0d} e^{-\frac{r}{R_e}} e^{-\frac{z}{Z_e}}, \quad (1)$$

where the radial and vertical scales R_e and Z_e and the central luminosity density ρ_{0d} are the model parameters of the problem.

Since all the objects studied were included in the Flat Galaxy Catalogue, we assume that they are seen exactly edge-on. The dust lane in the images is not displaced significantly relative to the galaxy plane. The symmetry of the image about the galaxy plane also provides evidence that the galaxy inclination deviates from 90° by no more than a few degrees.

We obtained the model disk image by integrating equation (1) along the line of sight. The radial extent of the disk was assumed to be $1.3\,R_{25}$, which roughly corresponds to four disk scales R_e (see, e.g., [17]).

To eliminate the effect of dust absorption on the actual surface brightness distribution, we did not consider regions located in the vicinity of the galaxy plane and masked regions within ±2 pixels of it. For the assumed distances to the objects (see Table 1), this is equivalent to excluding regions within 440 pc of the galaxy plane, on the average. We assumed dust absorption to be insignificant in regions outside the two excluded pixels.

When comparing the model disk brightness profile with the observed one, we also excluded the central part of the disk ($R < R_e$), where the bulge can contribute significantly to the luminosity.

The fitting was performed by minimizing the sum of the squares of deviations of the model profile from the observed one. We found the photometric disk parameters thus obtained to depend only slightly on whether the weighting function was used for the minimization or not.

The conversion to surface brightness (in magnitudes) was made by using calibration relations from RC96.

To determine the bulge parameters, we subtracted the model disk from the observed image. The central

part of the remainder was then fitted by the brightness distribution

$$I_b(X, Y) = \frac{I_{b0}}{1 + \frac{X^2 + Y^2}{R_{King}^2}}, \quad (2)$$

where X and Y are the coordinates in the plane of the sky. The central surface brightness I_{b0} and the characteristic bulge radius R_{King} are the model parameters. Apart from bulges whose surface brightness was specified by King's law (2), we considered de Vaucouleurs's law of brightness variations. In this case, however, the frequent divergence during minimization forced us to prefer the law (2). Large-scale images are required to infer the galaxy bulge parameters with a high accuracy. The available images allow the integrated bulge parameters, i.e., their total magnitudes and luminosities, to be estimated without substantial errors.

RESULTS OF DEPROJECTION

Table 2 contains the parameters inferred by deprojection. The table gives the galaxy name, the radial disk scale for the distance in Table 1, the vertical disk scale, the scale ratio Z_e/R_e, and the I central disk surface brightness μ_{d0} reduced to an inclination of 0°. Table 2 also gives the I central bulge surface brightness μ_{b0} (in magnitudes) and the King radius R_{King} of the bulge.

The central disk and bulge surface brightness for face-on galaxies was determined by using calibrations from RC96 and corrected for Galactic extinction by using data from the LEDA database.

The seeing was ~2–3″ during the observations. According to RC96, allowance for atmospheric effects when comparing images with the model causes the disk parameters to change by no more than 20%.

To estimate the errors in the quantities listed in Table 2, we formed several model images composed of disks and bulges whose luminosities were given by formulas (1) and (2). We added the noise typical of the images of our sample galaxies to the model brightness distributions. The parameters of the images formed in this way were obtained by using the deprojection procedure described above. The typical range of admissible photometric disk and bulge parameters was found to be no larger than 10%.

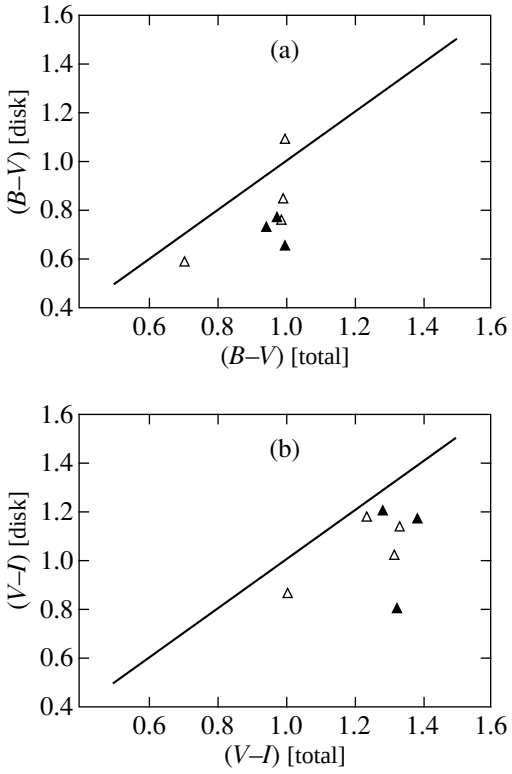

Fig. 1. Total color indices of the galaxies, *B–V* (a) and *V–I* (b), in comparison with the colors of their disks. The colors were corrected for Galactic extinction. The filled triangles represent galaxies of reduced surface brightness belonging to the fourth surface-brightness class in the FGC, and the open triangles indicate all the remaining galaxies of the sample. The straight lines correspond to equality of the color indices for the disks and galaxies as a whole.

To compare our radial and vertical disk scales with those inferred by RC97, who used individual cuts (without modeling), we considered not only the exponential distribution of volume luminosity (1), but also the

Table 2

UGC	R_e, kpc	Z_e, kpc	Z_e/R_e	μ_{d0}	μ_{b0}	R_{King}, kpc
11132	2.8	0.67	0.24	$20^m.9$	$21^m.7$	0.3
11230	8.2	1.96	0.24	21.6	23.3	0.6
11301	8.7	1.37	0.16	20.9	23.0	0.2
11838	4.1	0.82	0.20	21.3	26.9	0.1
11841	11.7	1.58	0.14	21.8	22.3	0.8
11859	3.2	0.51	0.16	22.2	20.9	0.7
11994	4.3	0.95	0.22	19.7	23.6	0.2

Table 3

UGC	This paper			RC96		
	R_e, kpc	Z_e, kpc	Z_e/R_e	R_e, kpc	Z_e, kpc	Z_e/R_e
11132	2.72	0.84	0.31	2.52	0.60	0.24
11230	7.00	2.44	0.35	8.96	1.47	0.16
11301	8.47	1.49	0.18	8.93	0.47	0.05
11838	3.86	1.05	0.27	5.52	0.85	0.15
11841	12.52	1.89	0.15	13.39	1.86	0.14
11859	3.46	0.65	0.19	2.97	0.45	0.15
11994	4.26	1.39	0.33	4.06	1.16	0.29

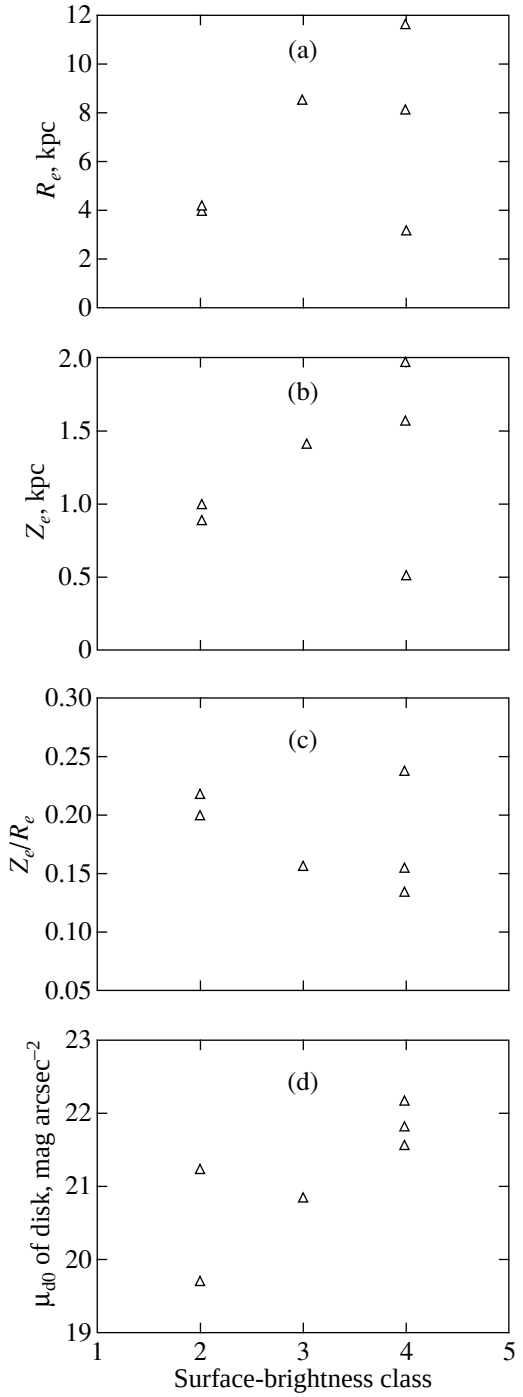

Fig. 2. The parameters of the model galaxy disks determined by fitting the *I*-band images. Radial scale R_e (a), vertical scale Z_e (b), Z_e/R_e ratio (c), and central disk surface brightness μ_{d0} (d) are plotted against FGC surface-brightness class.

$\mathrm{sech}^2\left(\frac{z}{Z_e}\right)$ vertical distribution. Table 3 gives R_e, Z_e, and Z_e/R_e for this case in comparison with the results from RC97. The radial scales match closely, whereas our vertical scale Z_e and Z_e/R_e ratio are systematically higher. This may be because RC97 corrected their Z_e for atmospheric effects; however, allowance for these effects causes Z_e to decrease by no more than 20% (according to RC97). Note also that we determined the photometric parameters for our sample objects in the same way, which allows us to compare the surface brightnesses μ_{d0} and the Z_e/R_e scale ratio of the disks.

To compare the results obtained by the method used here with the data obtained from individual cuts, we determined the disk parameters for the edge-on galaxy NGC 4244. The *I*-band image of this object was taken on February 13, 1994, with the JKT telescope at Observatorio del Roque de los Muchachos (La Palma). The exposure time was 1000 s. The image was provided via the Internet data archive by the Isaac Newton Group. The galaxy image was cleaned from cosmic-ray hits and flat-fielded. The photometric disk parameters were determined by using the procedure described above. The derived radial and vertical disk scales ($R_e = 104''$, $Z_e = 20''.3$) agree well with those obtained in [18] ($R_e = 107''$ and $R_e = 23''.9$, respectively) by analyzing individual cuts of the galaxy image taken on photographic plates.

Figure 2 shows plots of the galaxy disk parameters inferred by deprojection—R_e (Fig. 2a), Z_e (Fig. 2b), Z_e/R_e (Fig. 2c), and the central surface brightness of the galaxy disks μ_{d0} (Fig. 2d)—against surface-brightness class. It is evident from Fig. 2d that the disk surface brightness for the fourth-class galaxies is about $1^m.5$ lower than that for the second-class galaxies. This is in good agreement with the division of galaxies into HSB and LSB, which differ by about $1^m.5$–2^m in surface brightness (see, e.g., [19]).

Figures 2a and 2b suggest that there is no systematic difference between the radial and vertical disk scales of our sample galaxies belonging to different surface-brightness classes. The vertical-to-radial scale ratio tends to slightly decrease as we pass to galaxies of reduced surface brightness.

Thus, three galaxies of the fourth surface-brightness class in our sample have disks with reduced central surface brightness, which allows us to classify them as LSB galaxies. The disk scale of one of these galaxies (UGC 11841) exceeds 10 kpc, typical of large Malin 1-type galaxies (the so-called giant LSB galaxies; see [20]). Remarkably, UGC 11814 shows the lowest value of $Z_e/R_e \approx 0.136$ for our sample, in good agreement with that expected for flat edge-on galaxies [17].

One of the objects of our sample, UGC 11301, belongs to the third surface-brightness class and has a red disk (the *B*–*V* color index of the disk is about $1^m.10$). The value of μ_{d0} for it does not exceed appreciably that found for the second-class galaxies. However, since several faint field stars are superimposed on the UGC 11301 image, the derived disk surface brightness

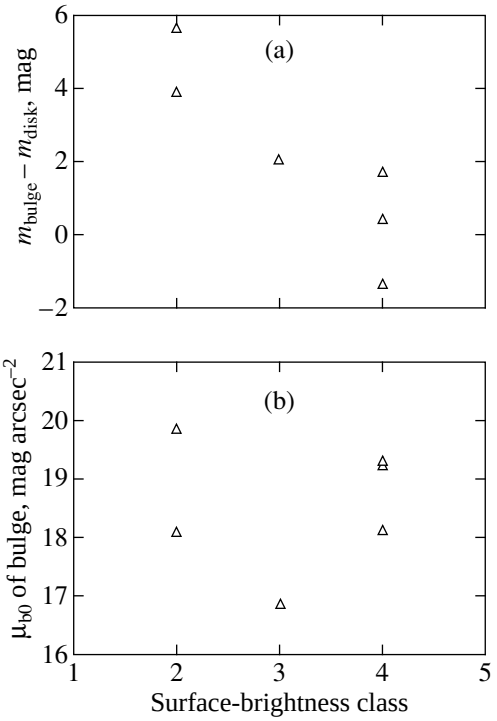

Fig. 3. Total bulge-to-disk luminosity ratio (in magnitudes) (a) and central bulge surface brightness (b) versus surface-brightness class.

is overestimated and represents a lower limit. The radial disk scale for UGC 11301 is 8.7 kpc, which is more typical of large galaxies with reduced surface brightness. This was also pointed out by RC97. In this case, we may be observing an object resembling the so-called red LSB galaxies. According to [21], such objects must also be encountered among LSB galaxies and account for up to 20% of their total number.

Optical rotation curves have been published for three galaxies of our sample: UGC 11132, 11230, and 11944 [22, 23]. They all have an extended rising portion. However, strong extinction in edge-on galaxies distorts the shapes of their rotation curves, and it would be improper to directly compare their shapes on the basis of optical observations.

Figures 3a and 3b show the magnitude differences between the bulge and the disk, as well as the central bulge surface brightness, for different surface-brightness classes. In this case, the bulge parameters were determined by assuming King's brightness distribution (2). As is evident from Fig. 3, the LSB galaxies of our sample have bulges of higher relative luminosities. At the same time, the central bulge surface brightness does not depend on the mean disk surface brightness.

For UGC 11132, 11859, and 11994, the remainders obtained by subtracting the model disk and bulge from the observed brightness distribution suggest the presence of additional components in the central part of the galaxy. These galaxies probably have a bar or a lens that are not taken into account in the model. However, for these components to be studied in more detail, high-resolution galaxy images must be analyzed.

CONCLUSION

The galaxies of our sample belonging to the fourth surface-brightness class according to the FGC have a number of properties typical of large LSB galaxies, namely, reduced central disk surface brightness and large radial disk scales.

The galaxies studied also show tendencies for the relative and absolute bulge luminosity to increase and for the vertical-to-radial scale ratio to decrease with decreasing mean surface brightness of the galaxy.

Our sample suggests that the FGC galaxies of the fourth surface-brightness class are mostly edge-on LSB galaxies. In that case, at least 3% (149 of 4455) of the FGC galaxies are candidates for galaxies of reduced surface brightness.

The FGC catalog may thus contain a considerable number of LSB galaxies with inclinations close to 90°. Their study will make it possible to reach conclusions about differences in the structure and evolution of the disk and spherical components of HSB and LSB galaxies.

ACKNOWLEDGMENTS

I am grateful to Dr. V.P. Reshetnikov, who provided the galaxy images obtained at the Observatoire de Haute Provence, and to Prof. A.V. Zasov for a discussion and critical remarks, which helped supplement and improve the content of the paper. I am also grateful to the referee for valuable remarks, which helped improve the presentation of material and supplement the content of the paper. The photometry for the galaxy NGC 4244 was found using the Internet data archive operated by the Isaac Newton Group (La Palma). This study was supported by the Russian Foundation for Basic Research (project no. 98-02-17102).

REFERENCES

1. P. van der Kruit, Astron. Astrophys. **173**, 59 (1987).
2. S. McGaugh, Mon. Not. R. Astron. Soc. **280**, 337 (1996).
3. E. De Blok, S. McGaugh, and T. van der Hulst, Bull. Amer. Astro. Soc. **189**, 8402 (1996).
4. G. Bothun, C. Impey, and S. McGaugh, Publ. Astron. Soc. Pacif. **109**, 745 (1997).
5. T. Pickering, C. Impey, J. van Gorkom, and G. Bothun, Bull. Amer. Astron. Soc. **184**, 1208 (1994).
6. W. de Blok and S. McGaugh, Astrophys. J. Lett. **469**, L89 (1996).
7. I. Karachentsev, V. Karachentseva, and S. Parnovsky, Astron. Nachr. **314**, 97 (1993).
8. V. Reshetnikov and F. Combes, Astron. Astrophys. **324**, 80 (1997).
9. I. Karachentsev, Ts. Georgiev, S. Kaĭsin, *et al.*, Astron. Astrophys. Trans. **2**, 265 (1992).

10. L. Matthews, L. Gallagher, and W. van Driel, astro-ph/9909142 (to be published in Astron. J.).
11. V. Reshetnikov and F. Combes, Astron. Astrophys., Suppl. Ser. **116**, 417 (1996).
12. G. de Vaucouleurs, A. de Vaucouleurs, H. Corwin, *et al.*, *Third Reference Catalogue of Bright Galaxies* (Springer, New York, 1991).
13. R. De Jong and P. van der Kruit, Astron. Astrophys., Suppl. Ser. **106**, 451 (1994).
14. J. Vennik, G. Richter, W. Thannert, *et al.*, Astron. Nachr. **317**, 289 (1996).
15. D. Sprayberry, C. Impey, G. Bothun, *et al.*, Astron. J. **109**, 558 (1995).
16. S. McGaugh and G. Bothun, Astron. J. **107**, 530 (1994).
17. A. Zasov, D. Makarov, and E. Mikhaĭlova, Pis'ma Astron. Zh. **17**, 884 (1991).
18. P. van der Kruit and L. Searle, Astron. Astrophys. **95**, 105 (1981).
19. R. Tully and A. Verheijen, Astrophys. J. **484**, 145 (1997).
20. T. Pickering and C. Impey, Bull. Amer. Astron. Soc. **186**, 3907 (1996).
21. J. Gerritsen and W. De Blok, Astron. Astrophys. **342**, 655 (1999).
22. I. Karachentsev, Pis'ma Astron. Zh. **17**, 485 (1991).
23. D. Makarov, I. Karachentsev, N. Tyurina, *et al.*, Pis'ma Astron. Zh. **23**, 509 (1997).

Translated by A. Dambis

Astronomy Letters, Vol. 26, No. 4, 2000, pp. 225–232. Translated from Pis'ma v Astronomicheskiĭ Zhurnal, Vol. 26, No. 4, 2000, pp. 273–281.

Analysis of HST Ultraviolet Spectra for T Tauri Stars: RU Lup

S. A. Lamzin*

Sternberg Astronomical Institute, Universitetskiĭ pr. 13, Moscow, 119899 Russia

Received April 10, 1999; in final form, September 13, 1999

Abstract—The ultraviolet spectra of the star RU Lup obtained with the Hubble Space Telescope are analyzed. Emission lines are identified. The presence of absorption components with a nearly zero residual intensity in the Mg II resonance doublet lines is indicative of mass outflow with a velocity $V_\infty \simeq 300$ km s^{-1}. These lines also exhibit a broad ($\simeq$1400 km s^{-1} at the base) component originating in the star itself. The profiles of the (optically thin) Si II] and Si III] 1892 Å lines for the first time unequivocally prove that these lines originate in an accretion shock wave rather than in the chromosphere, with the gas infall velocity being $V_0 \simeq 400$ km s^{-1}. The intensity ratio of the C IV 1550 Å and Si IV 1400 Å resonance doublet components was found to be close to unity, suggesting a high accreted-gas density, $\log N_0 > 12.5$. Molecular H_2 Lyman lines formed in the stellar wind were detected. The H I $L\alpha$ luminosity of RU Lup was found from their intensities to exceed 10% of L_{bol}. Radiation pressure in the $L\alpha$ line on atomic hydrogen may play a significant role in the initial acceleration of stellar-wind matter, but the effect of $L\alpha$ emission on the dynamics of molecular gas is negligible. *© 2000 MAIK "Nauka/Interperiodica".*

Key words: *stars—variable and peculiar; T Tau stars*

INTRODUCTION

Until now IUE satellite observations (see the reviews [1, 2]) have been virtually the only source of information about the ultraviolet spectra of T Tau stars. However, since the sensitivity of the IUE receiving equipment was low, only low-resolution ($\simeq$6 Å) spectra turned out to be suitable for analysis; they did not allow the emission-line profiles to be judged. Meanwhile, ultraviolet observations of T Tau stars have been carried out with the Hubble Space Telescope (HST) since 1992, but their results have not yet been published. Here, our goal is to perform a preliminary analysis of the HST spectra for the star RU Lup.

RU Lup is an extreme representative of the T Tau stars: the equivalent width of Hα in its spectrum is $\simeq$200 Å. The properties of this star are detailed in [3, 4]; an overview of previous literature is also given in these papers. The observed properties of RU Lup can apparently be described properly in terms of the model of disk accretion onto a magnetized low-mass star. Recent numerical calculations of the accretion-shock structure [5] have opened up possibilities for a quantitative comparison of theory with observations. The ultraviolet range is most suitable for this purpose, because optical emission lines can, in principle, originate not only in the shock wave, but also in the chromosphere and/or the stellar wind. Below, we show what kind of information can be extracted from the HST ultraviolet spectra of the star.

OBSERVATIONAL DATA

The spectra analyzed below were taken from the HST archival database (http://archive.stsci.edu/hst/target_descriptions.html). We reduced the spectra by means of the IRAF v2.11 (http://iraf.noao.edu/iraf) and STSDAS/TABLES v2.0.2 (http://ra.stsci.edu/STSDAS.html) software packages. The standard technique described in Chapter 36 of the HST Data Handbook (http://www.stsci.edu/documents/data-handbook.html) was used; the files recommended in the archival database were used for calibration.

All the analyzed spectra of RU Lup were obtained with the GHRS spectrograph in intermediate-resolution mode on August 24, 1992. Since the COSTAR primary-mirror aberration corrector had not been installed by that time, the spectra have a relatively low signal-to-noise ratio. Table 1 gives the identification numbers of archival spectra, the diffraction grating used, the wavelength range, the number of intermediate exposures (parameter RPTOBS+1), the starting time of the first exposure to within a minute (UT), and the total exposure. All spectra were taken in ACCUM mode on detector 2 through aperture LSA ($D = 2''$) and have the same values of the following service parameters: FP_SPLIT = 'NO', STAPPATT = 5, and COMB_ADD = 'FOUR'. The wavelengths were reduced to the Solar-system bary-

* E-mail address for contacts: lamzin@sai.msu.ru

Table 1. Parameters of the spectra

Spectrum code	Grating	Wavelength range, Å	Number of exposures	t_0, UT	Δt, s
z10t0104m	G160M	1383–1418	3	03:14	82
z10t0105m	G160M	1532–1567	5	03:30	1360
z10t0107m	G160M	1622–1658	5	04:39	1360
z10t0109m	G200M	1879–1920	5	05:05	1496
z10t010bm	G270M	2777–2822	1	06:17	245
z10t010cm	G270M	2301–2349	2	06:22	544

center and are given below for a vacuum. To improve the signal-to-noise ratio, all figures show the spectra that were not only averaged over all intermediate exposures, but also smoothed with a four-point running mean. So, the spectrogram have a formal resolution of ~15 km s^{-1}.

INTERPRETATION OF THE SPECTRA

Figure 1 shows the star's spectrum near the Mg II resonance doublet. We clearly see narrow interstellar absorption lines with the centers at the laboratory wavelengths of the doublet ($\lambda_{c1} = 2796.35$ Å, $\lambda_{c2} = 2803.53$ Å), in agreement with the results of Schwartz and Heuermann [6] who obtained $V_r = -0.5 \pm 2.8$ km s^{-1} from optical absorption lines. The relative intensity of the doublet components is close to unity, with both lines having P Cyg profiles. This is direct evidence for the presence of a nearly spherical, outflowing envelope in the immediate vicinity of the star. The upper level of the 2796.35 Å resonance line ($3p^2P$ with $E_j = 4.4$ eV) is also the lower level of the λ 2798.75 and 2798.82 Å lines ($3p^2P$–$3d^2D$ transition), whose traces are not seen in the spectrum. However, the third line of the same multiplet at λ = 2791.60 Å (lower level $^2P_{1/2}$) may be responsible for the corresponding emission feature.

The red wing of the 2804 Å line is closely fitted by the law $F_\lambda \propto (\lambda - \lambda_{c2})^{-2}$; the corresponding curve is barely seen in the figure. Both doublet lines have virtually the same shape, so the fitting curve displaced by $\lambda_{c1} - \lambda_{c2}$ also describes well the red wing of the 2796 Å line. Moreover, the reflection of this curve with respect to λ_{c2} and λ_{c1} turned out to pass through the emission features observed in the blue wing of each of the lines to the left of the absorption dip (see the dashed–dotted lines in Fig. 1). Hence, it probably follows that the observed shape of the Mg II lines resulted from the superposition of a line originating in the stellar wind on a broader (~1400 km s^{-1} at the base) symmetric emission line originating in the star itself. It is worth noting that the Mg II lines had a similar structure in the IUE spectrum of T Tau in March 1992, whereas there are no traces of the broad component in the November 1980 spectrogram (see Fig. 3 in [7]). If the broad component originates in the stellar atmosphere heated by X-ray and ultraviolet emission from an accretion shock wave [5, 8], then this fact suggests nonsteady accretion.

Note, incidentally, that the Ca II H and K resonance lines and Hα in the RU Lup spectrum are a factor of 2 or 3 narrower and apparently have a similar structure, although the absorption dip in Hα does not sink to the continuum level (see Figs. 3–5, and 9 in [6], Fig. 13 in [9], and Fig. 7 in [3]). This probably implies that, in the case of RU Lup, we have two comparable (in contribution) Ca II and hydrogen emission regions. As a result, previous attempts to determine the parameters of the emitting region from an analysis of these lines proved to be contradictory.

According to Boesgaard [9], more than half of the emission lines observed in the wavelength range 4000–4500 Å belong to Fe II with a lower-level excitation energy $E_i \simeq 2.6$ eV and to Fe I with $E_i \simeq 1$ eV. When identifying emission features in our spectra, we therefore considered lines of singly ionized metals with $E_i <$ 3 eV and of neutral atoms with $E_i < 1.5$ eV as the most likely candidates. In Fig. 1, the lines of the Fe I a^5F–y^5G multiplet (uv 44), as well as Fe II a^4F–z^6D (uv 32) and b^2H–z^2G (uv 234), belong to such lines. This identification strongly suggests the presence of continuum with intensity $F_c \simeq 8 \times 10^{-14}$ erg s^{-1} cm^{-2} Å^{-1} in the spectrogram, whose level is indicated in Fig. 1 by the dashed line.

The spectrum in the range 2300–2350 Å (see Fig. 2) proves to be more difficult to interpret. Only the blend of two intercombination lines, Si II $3s^23p^2P$–$3s3p^2\,^4P$ at λ 2335.12 and 2335.32 Å, is clearly identified in it at a glance. The vicinity of these lines is shown in Fig. 3 on a larger scale. The dashed line represents the profile of the Si III 1892 Å intercombination line (present in Fig. 4a), whose center is shifted to Si II] 2335.32 Å. The red wings of the lines are seen to almost coincide, suggesting that there is virtually no continuum in our spectrogram. The following reasoning serves as an additional argument for this conclusion: the star's continuum energy distribution in the wavelength range 2300–3600 Å is well described by a blackbody curve with $T \sim 7000$ K and $A_V = 0\overset{m}{.}6$ [4]; therefore, extrapolation of the observed continuum intensity near 2800 Å to the wavelength range under consideration yields $F_c \simeq 1 \times 10^{-14}$ erg s^{-1} cm^{-2} Å^{-1}, which roughly corresponds to the minimum intensity in Fig. 2.

Fitting the emission features near 2332, 2334, and 2339 Å with Gaussians (dotted curves in Fig. 3) allows them to be reliably identified with Fe II lines: the Gaussian centers coincide with the laboratory λ of the corresponding lines to within 0.01 Å. The FWHM of these lines is ≃100 km s^{-1}. This is, on the average, 25% smaller than that of the Fe II lines in the blue part of the optical range [9], which are also bell-shaped and symmetric about λ_c. Since $E_i < 3$ eV for the identified Fe II lines, we rest assured that the identification criterion we chose was correct, and it became clear that the broad features in the spectrograms were emission blends of

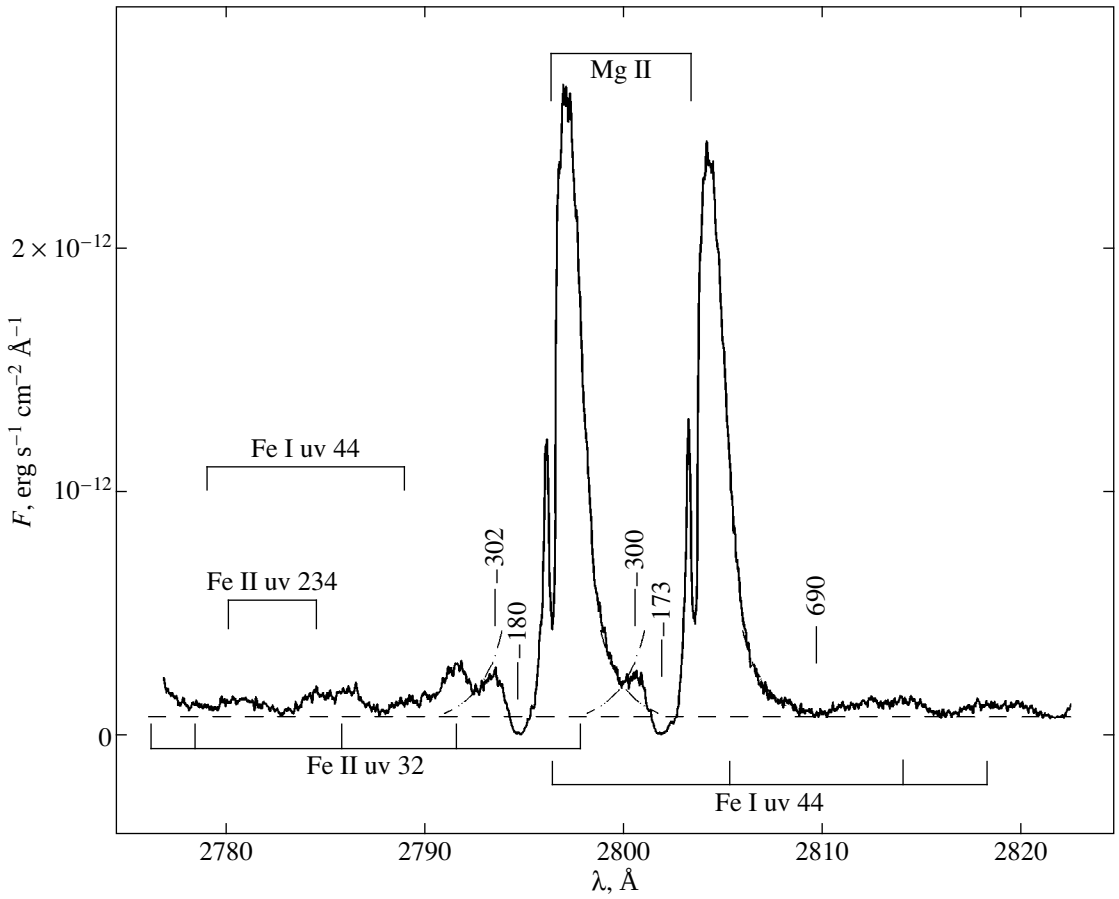

Fig. 1. The spectrum of RU Lup near 2800 Å.

several lines, some of which we identified with Fe II and Ni II lines (see Fig. 2).

Apart from the metal lines, there may be intercombination lines of the quintet C II $2s^2 2p^2 P$–$2s2p^2\,{}^4P$ in the spectrogram. The small Einstein coefficients A_{ij} of these lines (from 1.7 to 65.5 s^{-1}) strongly suggest that they are optically thin, and, consequently, their profiles must reflect only the velocity field in the formation region (the "thermal" line width cannot exceed 10 km s^{-1}). The Si II] lines are probably also optically thin, although their Einstein coefficients A_{ij} are two orders of magnitude larger. Unfortunately, the C II] and Si II] line profiles are severely distorted by blending, and only an unusually extended (almost up to 400 km s^{-1}) red wing of the Si II] 2335.12 + 2335.32 Å blend can be noted. Since the red wings of this feature and Si III] 1892 Å are virtually identical, we are confident that there is a motion of gas away from the observer at a velocity up to 400 km s^{-1}. The star RU Lup is seen almost pole-on and has an opaque gas–dust disk. As a result, the extent of the red wings of [O I] 6300 Å and [S II] 6731 Å, which originate in the stellar wind, apparently does not exceed 50 km s^{-1} (see Fig. 1c in [10]). Thus, our data strongly suggest the accretion of circumstellar matter onto RU Lup.

Unfortunately, neither the shape of the blue wings of the C II] and Si II] lines nor the relative intensity of the lines themselves can be judged because of blending. However, the C II] lines in the stellar spectrum are much weaker than the Si II] lines, while C III] 1909 Å is almost an order of magnitude weaker than Si III] 1892 Å (see Fig. 4a). It thus follows that $N_e > 10^{11}$ cm^{-3} in the formation region of these lines, in agreement with the estimate $\log N_e \simeq 12.5$ obtained by Lamzin *et al.* [4]. In this case, as follows from the diagram in [11], the gas infall velocity V_0 must be close to 400 km s^{-1}.

Line identification in the stellar spectrum near 1900 Å (see Fig. 4a) was made in [12], which aims at studying the geometry of the accretion zone; the spectrogram near 1640 Å (Fig. 4b) contains little information: it only allows the presence of He II 1640 Å to be ascertained. We provide these two spectra merely to elucidate the nature of the emission feature near 1907 Å. It is virtually identical to the feature at $\lambda \simeq 1647$ Å, with both falling on the same photodiodes of the receiving array (342–345). We therefore consider these to be artifacts.

The stellar spectrum near 1550 Å (Fig. 5a) contains much more information, despite the low signal-to-noise ratio. The two H_2 lines corresponding to the $R(3)$ 1547.34 Å and $P(5)$ 1562.39 Å transitions are clearly identified in the spectrogram. Both lines belong to the Lyman series (i.e., to transitions between the

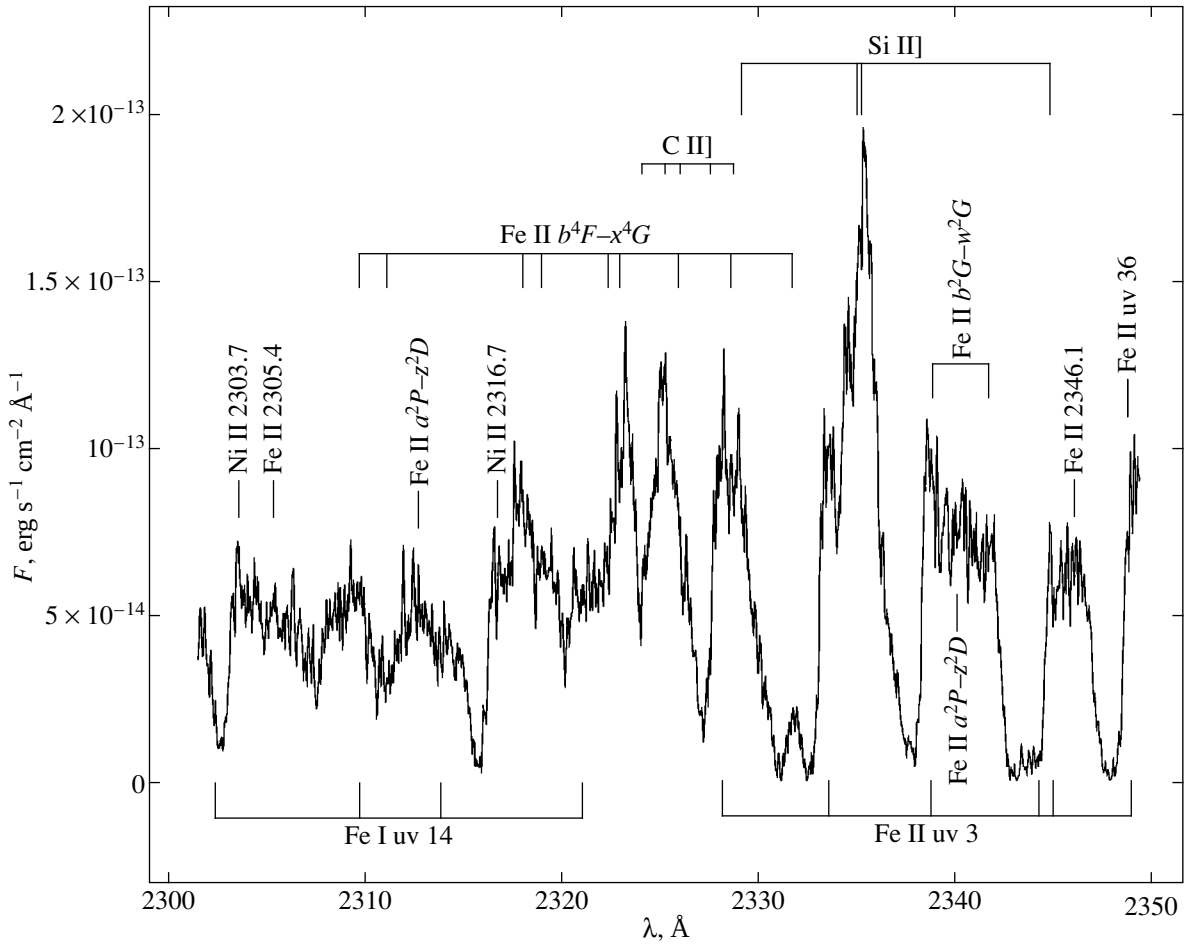

Fig. 2. The spectrum of RU Lup near 2350 Å.

$2p\sigma B^1\Sigma_u^+ \longrightarrow X^1\Sigma_g^+$ electronic configurations) and have a common upper level with $v' = 1$, $J' = 4$ and lower levels with $v'' = 8$, $J'' = 3$ and $v'' = 8$, $J'' = 5$, respectively. Lyman H_2 lines in the spectra of T Tau stars were first detected in T Tau itself [7]; however, an examination of the catalog [2] shows these lines to be apparently present in the spectra of many young stars (see also [13]). The upper level of these lines is excited via resonant absorption of $L\alpha$ emission from the levels of the ground electron configuration $X^1\Sigma_g^+$.

The spectra in Fig. 5 exhibit several more emission features, which can be attributed to H_2 molecular emission. Table 2 gives the following data for each line: quantum numbers v_0'' and J_0'' of the level from which the pumping occurs; pumping transition probabilities A_{ij}^0; wavelength shifts of the pumping photon from $\lambda_{L\alpha}$ (ΔV); quantum numbers of the upper (v_0', J_0') and lower (v'', J'') levels; and transition probabilities A_{ij} of the line under consideration. The values of A_{ij} were taken from [14].

The spectrum quality does not allow the molecular-line profiles to be judged with confidence. However, these lines are seen to be located almost entirely to the left of the central wavelength, i.e., they originate in matter moving away from the star. For the observed lines to emerge, the H_2 levels with energies up to $\simeq$1.5 eV must have a sufficiently large population; hence, it follows that the molecular gas has a temperature $T_m \sim 2000$K and a fairly high density. It would be natural to assume that the region where the ultraviolet H_2 lines originate is identical to the region where the infrared H_2 line at $\lambda = 2.1218$ μm [the $v = 1 \longrightarrow 0$ $S(1)$ transition of the ground electron configuration $X^1\Sigma_g^+$] observed in RU Lup is formed [15].

An analysis of the images of star-forming regions at $\lambda = 2.1$ μm shows that the infrared molecular H_2 emission is associated with the shock waves generated by the interaction of jets with protostellar-cloud remnants (see, e.g., [16] and references therein). The emission regions in all the young stars studied are a set of individual spots surrounding Herbig–Haro objects, which generally form an elongated chain inside a cone with an apex angle $\alpha_j < 15°$. As was pointed out above, the RU Lup spectrum exhibits the blueshifted [O I] 6300 Å and [S II] 6731 Å lines; this is clear evidence for the presence of structures similar to Hebig–Haro near objects in

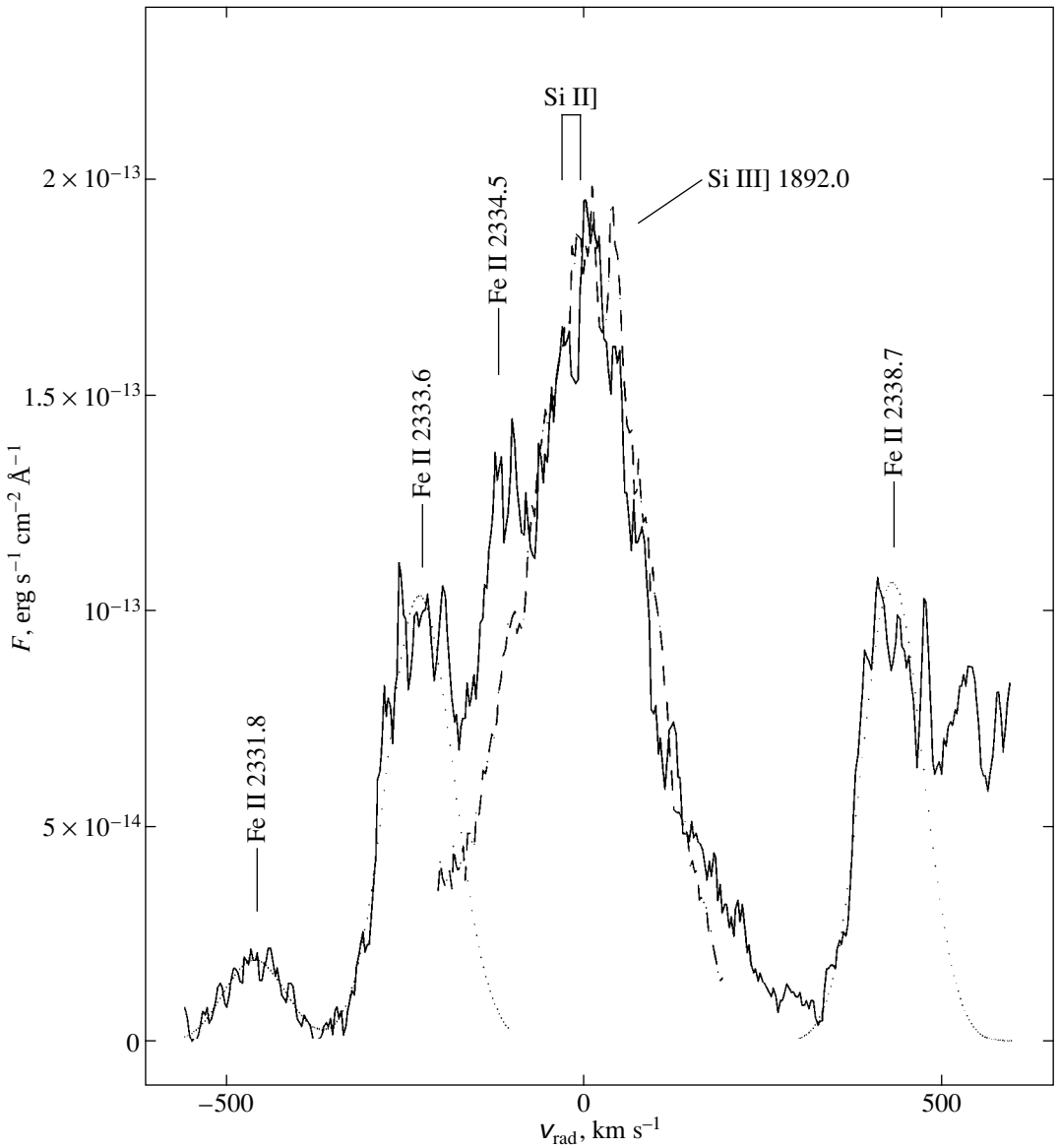

Fig. 3. A portion of the spectrum in Fig. 2. The dashed line indicates the Si III] 1892 Å line profile from Fig. 4a whose center coincide with that of the Si II] 2335.32 Å line, and the dotted lines represent Gaussian fits to the profiles of three emission features.

the star. It would therefore be reasonable to assume that the infrared and ultraviolet molecular H_2 emission in RU Lup also originates inside the jet. (It is unlikely that a direct image of this jet will ever be obtained, because the star is seen nearly pole-on; therefore, the jet must be oriented almost exactly along the line of sight).

Let us estimate the $L\alpha$ luminosity of RU Lup reradiated by molecular hydrogen. It follows from Fig. 5a that the total observed flux in the $R(3)$ 1547.34 Å and $P(5)$ 1562.39 Å lines is ~10^{-13} erg s^{-1} cm^{-2}, which corresponds to a luminosity of 2×10^{30} erg s^{-1} at $d = 200$ pc [17] and $A_V = 0\overset{m}{.}6$. Downward transitions to produce several more lines are possible from the upper level $2p\sigma B^1\Sigma_u^+$, $v' = 1$, $J' = 4$ of the pair of lines under consideration, with the relative probability of 1547.34 and 1562.39 Å line emission being about 1/8 [14]. The total luminosity in the lines with this upper level must then be ~2×10^{31} erg s^{-1}. Since each of these lines is produced by the absorption of one $L\alpha$ photon, we find the $L\alpha$ luminosity L_f absorbed by H_2 molecules to be $>2 \times 10^{31}$ erg s^{-1}. (We put the inequality sign, because $L\alpha$ photons can be absorbed not only from the $v_0'' = 2$, $J_0'' = 5$ level of the ground molecular electronic configuration; see Table 2).

Let us now assume that $L\alpha$ photons are absorbed by molecules only within a cone with an apex angle $\alpha_j \sim 15°$, i.e., in the solid angle $\Omega = \pi\alpha_j^2/4$, because $\alpha_j^2 \ll 1$ if

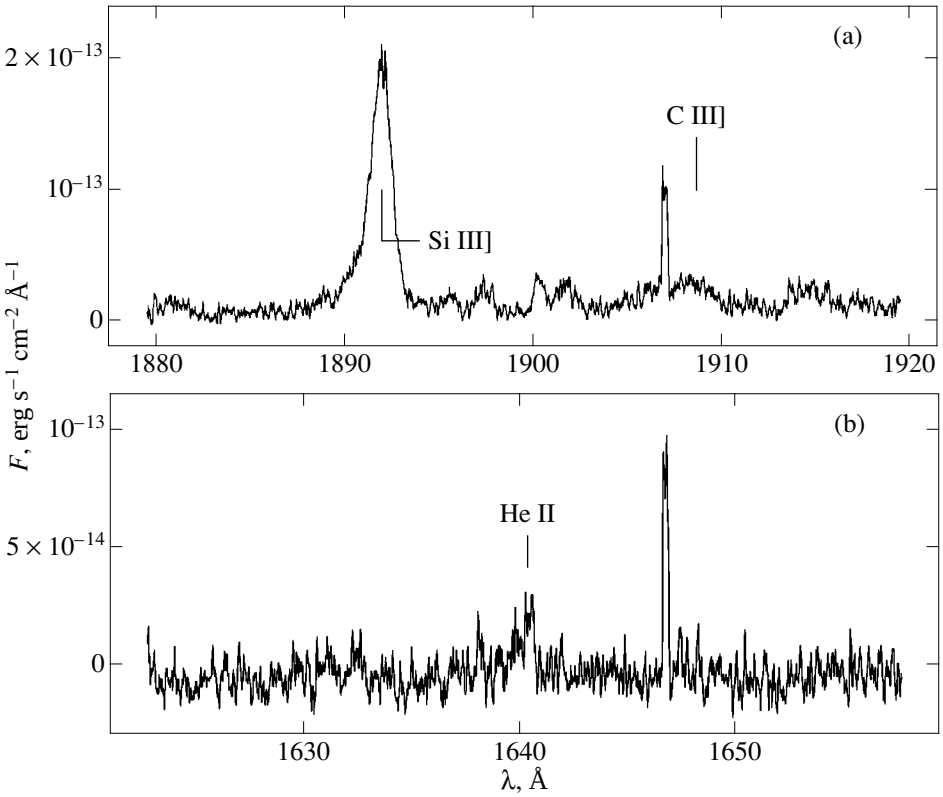

Fig. 4. The spectrum of RU Lup near (a) 1900 Å and (b) 1640 Å.

expressed in radians. Consequently, the total luminosity of RU Lup is $L_{L\alpha} = 4\pi/\Omega L_f \geq 5 \times 10^{33}$ erg s^{-1}, i.e., it exceeds 10% of $L_{\rm bol}$. This is no surprise, given that the star's Hα luminosity exceeds 10^{32} erg s^{-1} [3]. Note, incidentally, that Brown *et al.* [7] estimated $L_{L\alpha}$ for T Tau to be ~4×10^{33}, or 5% of $L_{\rm bol}$.

We get the impression that a high (>10^{33} erg s^{-1}) Lα luminosity is a characteristic feature of the classical T Tauri stars [18]. This circumstance probably plays an important role in the evolution of envelopes around young stars, because the radiation pressure of Lα photons on hydrogen atoms is much larger than the force with which they are attracted by the star:

$$\frac{F_{\rm grav}}{F_{\rm rad}} = \frac{GM_* m_{\rm H}/r^2}{\sigma_0 L_{L\alpha}/4\pi r^2 c} \sim 3 \times 10^{-7}\left(\frac{M_*}{M_\odot}\right) \times \left(\frac{10^{33}}{L_{L\alpha}, \text{ erg s}^{-1}}\right)\left(\frac{T, \text{K}}{1000}\right)^{1/2},$$

where $\sigma_0 \simeq 1.9 \times 10^{-13}$ cm^2 is the coefficient of absorption at the Lα center by hydrogen with temperature $T = 10^3$ K [19]. The pressure of Lα photons on the atmospheric hydrogen atoms of a protoplanetary disk can ensure the initial acceleration of cold matter to the velocity of the order of several km s^{-1} required in magnetic rotation models of mass outflow from the surroundings of young stars. By contrast, the dynamical role of Lα radiation pressure on molecular hydrogen is most likely negligible. The flux in the λ = 2.1218 μm $v = 1 \longrightarrow 0S(1)$ line for RU Lup is $F_{\rm IR} \simeq 2.2 \times 10^{-13}$ erg s^{-1} cm^{-2} [15]; this line is optically thin, because $A_{ij} \simeq 4.2 \times 10^{-7}$ s^{-1} for it [20]. From the relation

$$4\pi d^2 F_{\rm IR} = (M_{\rm H_2}/2m_{\rm H}) n_{1,1} A_{ij} h\nu_{\rm IR},$$

where $n_{1,1}$ is the relative population of the transition upper level, we derive the mass of the molecular hydro-

Table 2. Parameters of the H_2 lines in Fig. 5

λ, Å	Designation	v_0'', J_0''	A_{ij}^0, 10^8 s^{-1}	ΔV, km s^{-1}	v_0', J_0'	v'', J''	A_{ij}, 10^8 s^{-1}
1562.39	$P(5)$	2, 5	1.6	+99	1, 4	8, 5	1.2
1556.87	$R(6)$	2, 6	1.7	+15	1, 7	8, 6	1.3
1556.60	$R(15)$	1, 15	1.0	−295	3, 16	8, 15	0.38
1551.76	$P(17)$	1, 15	1.0	−295	3, 16	7, 17	0.52
1547.34	$R(3)$	2, 5	1.6	+99	1, 4	8, 3	1.1
1393.96	$R(1)$	2, 1	0.78	+490	0, 2	5, 1	1.6
1393.72	$R(0)$	2, 0	0.66	+380	0, 1	5, 0	1.4
1398.95	$P(2)$	2, 0	0.66	+380	0, 1	5, 2	2.6
1402.65	$P(3)$	2, 1	0.78	+490	0, 2	5, 3	2.6

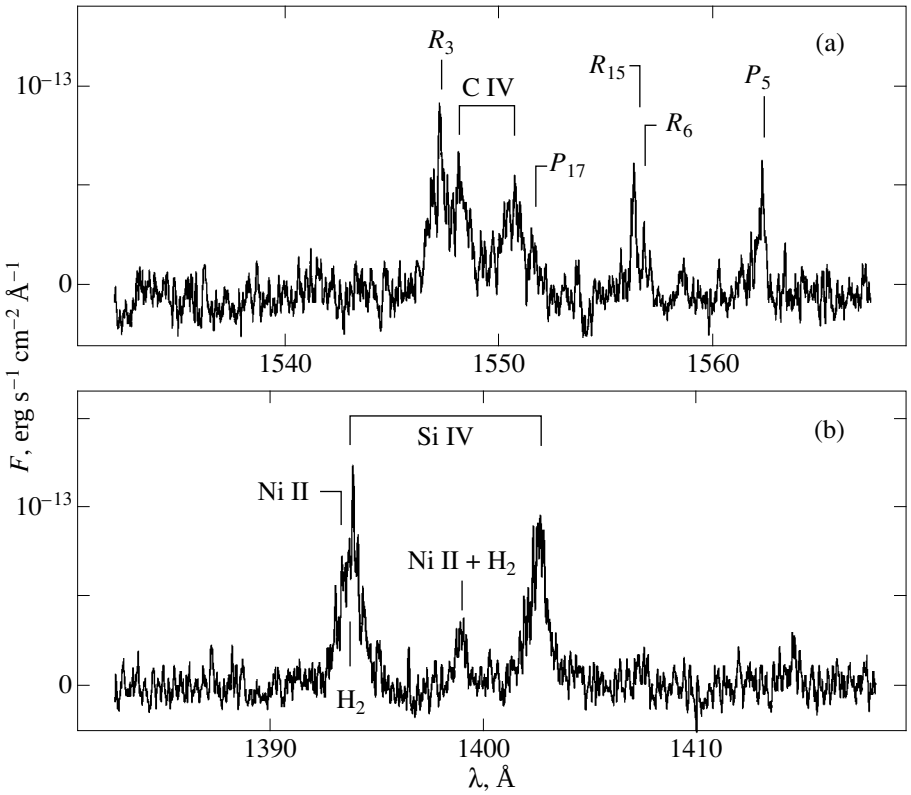

Fig. 5. The spectrum of RU Lup near (a) 1550 Å and (b) 1400 Å.

gen emitting the line in question: $M_{H_2} \sim 10^{25}/n_{1,1}$ g. The excitation energy of the $v = 1$, $J = 1$ level is ~0.6 eV, and the statistical weight is 3. Assuming that its population does not exceed the Boltzmann one at $T = 2000$ K, we therefore obtain $n_{1,1} < 0.1$; hence $M_{H_2} > 10^{26}$ g. We can now estimate the acceleration that the molecular hydrogen absorbing $L\alpha$ photons acquires: $a = L_{\beta}/(c M_{H_2}) < 10^{-5}$ cm s^{-2}. It takes a time $V/a > 3000$ years for the gas to gain a velocity $V \sim 10$ km s^{-1}, which appears to be much longer than the cooling time of the heated post-shock molecular hydrogen; after the molecules cool down, they emerge from the resonance with $L\alpha$, and the acceleration ceases. (In order to avoid misunderstandings, we note that the acceleration of atomic hydrogen is much more effective, because $L\alpha$ is the resonance line.)

Since the $R(3)$ 1547.34 Å line is comparable in intensity to the short-wavelength line of the C IV 1550 Å resonance doublet, the intensity ratio of the doublet components is $F_{1548}/F_{1551} \simeq 1$ rather than 2, as has been argued previously. The situation with the Si IV 1400 Å resonance doublet lines is similar (see Fig. 5b): the component intensity ratio is $F_{1394}/F_{1403} \simeq 1$, because the Ni II 1393.32 Å resonance line indiscernible in the IUE spectra and, possibly, also H_2 lines (see Table 2) are apparently superimposed on the blue wing of Si IV 1393.76 Å. (Incidentally, there is yet another emission feature in the spectrum, which it would be reasonable to consider a blend of H_2 1398.95 Å and Ni II 1399.02 Å with $E_i = 0.19$ eV). This appears to suggest that the emission in the C IV and Si IV doublet lines may be thermalized in the case of RU Lup, which is consistent with the above conclusion about a high density of the gas accreted by the star ($\log N_0 > 12.5$) (see [5] for more detail).

CONCLUSION

The above discussion shows that the HST ultraviolet spectra of T Tauri stars are very informative and allow an appreciable progress to be made in elucidating the nature of activity in young stars. In the case of RU Lup, we have been able to directly verify for the first time that the emission lines originate both in the stellar wind ($V_\infty \simeq 300$ km s^{-1}) and in an accretion shock wave. Despite the low signal-to-noise ratio, we were able to determine the gas infall velocity ($V_0 \simeq 400$ km s^{-1}). The relatively high spectral resolution allowed us to detect H_2 molecular lines in the stellar spectrum and to estimate the $L\alpha$ luminosity of RU Lup, ~10% of L_{bol}. We found evidence for possible thermalization of the emission in the C IV 1550 Å and Si IV 1400 Å doublet resonance lines.

An analysis of archival HST ultraviolet spectra for other young stars will undoubtedly yield much impor-

tant information about these objects. Finally, the launch of a specialized ultraviolet observatory seems of current interest.

ACKNOWLEDGMENTS

I wish to thank the Hubble Space Telescope Science Institute for permission to access the HST archive. I also wish to thank N.G. Bochkarev, A.S. Rastorguev, and A.I. Gomez de Castro for helpful discussions, A. Dalgarno for reporting the paper by Abgrall *et al.* [14], and A.Yu. Zaitsev for help in installing the IRAF-STSDAS software package, which was widely used here along with P. Van Hoff Atomic Line List v.2 database. I am grateful to the referee for useful remarks.

REFERENCES

1. C. L. Imhoff and I. Appenzeller, *Exploring the Universe with IUE Satellite*, Ed. by Y. Kondo (D. Reidel Publ., Dordrecht, 1989), p. 295.
2. A. I. Gómez de Castro and M. Franqueira, *ULDA Access Guide to T Tauri Stars Observed with IUE, ESA SP-1205, ESTEC* (ESA Publications Division, Noordwijk, 1997).
3. F. Giovannelli, A. Vittone, C. Rocci, *et al.*, Astron. Astrophys., Suppl. Ser. **114**, 341 (1995).
4. S. A. Lamzin, G. S. Bisnovatyi-Kogan, L. Errico, *et al.*, Astron. Astrophys. **306**, 877 (1996).
5. S. A. Lamzin, Astron. Zh. **75**, 367 (1998).
6. R. D. Schwartz and R. W. Heuermann, Astron. J. **86**, 1526 (1981).
7. A. Brown, M. C. de Ferraz, and C. Jordan, Mon. Not. R. Astron. Soc. **207**, 831 (1984).
8. S. A. Lamzin, Astron. Astrophys. **295**, L20 (1995).
9. A. M. Boesgaard, Astron. J. **89**, 1635 (1984).
10. F. Hamann, Astrophys. J., Suppl. Ser. **93**, 485 (1994).
11. A. I. Gómez de Castro and S. A. Lamzin, Mon. Not. R. Astron. Soc. **304**, L41 (1999).
12. S. A. Lamzin, Astron. Zh. **25**, 505 (1999).
13. F. Walter, G. Basri, A. Brown, *et al.*, AAS Meeting **186**, 906 (1995).
14. H. Abgrall, E. Roueff, F. Launay, *et al.*, Astron. Astrophys., Suppl. Ser. **101**, 273 (1993).
15. B. A. Wilking, R. D. Schwartz, L. G. Mundy, and A. S. B. Schultz, Astron. J. **99**, 344 (1990).
16. C. J. Devis, J. Eisloffel, and D. Smith, Astrophys. J. **463**, 246 (1996).
17. R. Wichmann, U. Bastian, J. Krautter, *et al.*, Mon. Not. R. Astron. Soc. **301**, L39 (1998).
18. V. G. Kurt and S. A. Lamzin, Astron. Zh. **72**, 364 (1995).
19. S. A. Kaplan and S. B. Pikel'ner, *Interstellar Medium* (Nauka, Moscow, 1963).
20. L. Wolniewicz, I. Simbotin, and A. Dalgarno, Astrophys. J., Suppl. Ser. **115**, 293 (1998).

Translated by V. Astakhov

Astronomy Letters, Vol. 26, No. 4, 2000, pp. 233–243. Translated from Pis'ma v Astronomicheskiĭ Zhurnal, Vol. 26, No. 4, 2000, pp. 282–293.

A Photometric and Spectroscopic Study of the Herbig Ae/Be Star XY Per

S. Yu. Melnikov* and O. V. Ezhkova

Astronomical Institute, Academy of Sciences of Uzbekistan, ul. Astronomicheskaya 33, Tashkent, 700052 Uzbekistan

Received April 5, 1999; in final form, September 13, 1999

Abstract—The *UBVR* photometry of XY Per in 1985–1998 is presented. At this epoch, XY Per exhibited variability with an amplitude of $\approx 1^m$ in *V*. The photometric variability of XY Per can be divided into three components: (1) smooth year-to-year variations in mean brightness; (2) quasi-periodic variations with a characteristic time scale of 20–40 days and an amplitude of $0\overset{m}{.}3$; and (3) Algol-like minima with a duration of 15–20 days and an amplitude of $0\overset{m}{.}6$. The CLEAN algorithm is used to refine the quasi-period of light variations in the interval 1988–1995, $P = 22\overset{d}{.}7252$. The observed variability is assumed to be produced by two mechanisms: circumstellar absorption and nonstationary accretion. An ultraviolet excess was observed in the stellar radiation during the local minimum of 1991, which was associated with an eclipse of the star by a circumstellar formation. The probable reason why it emerged is that part of the eclipsing circumstellar formation fell into the accretion zone. A high-resolution spectrum in the wavelength range 3600–6700 Å contains both photospheric lines and circumstellar shell lines. The shell line profiles suggest mass accretion onto the star at a velocity of 90–140 km s^{-1}. Of the Balmer lines, only Hα is in emission. Its equivalent width is $E(W_\lambda) = -0.8$ Å. The strongest Fe II lines, as well as Mg II 4481.33 Å and He I 5875.65 Å, have an emission component at the line center. The presence of emission components in lines with different excitation potentials suggests the presence of a hot gas shell around the star, which is heated very nonuniformly. © *2000 MAIK "Nauka/Interperiodica".*

Key words: *stars—variable and peculiar*

INTRODUCTION

Currently, more and more binary and multiple systems are being discovered in star-forming regions. For example, 30 of the 68 Herbig Ae/Be stars investigated by Corporon [1] are binaries. Thus, the gap coupled with a deficit of multiple systems among pre-main-sequence stars is gradually bridged. One of such systems is the visual binary XY Per (A+B) (ADS 2788).

XY Per lies at the edge of the dark nebula L1449, with which it is apparently associated and illuminates a bright emission nebula [2]. According to the latest Hipparcos data, the angular separation between the components of XY Per is $\rho = 1\overset{''}{.}331$, and the position angle is $\Theta = 76°$. XY Per has been known as a variable star since 1921 [3]. At the epoch of maximum light, the western component (W) is $0\overset{m}{.}5$–$0\overset{m}{.}6$ brighter than the eastern component (E) [4]. The total variability amplitude reaches $1\overset{m}{.}1$–$1\overset{m}{.}3$, as inferred by different authors. This value exceeds the magnitude difference between the components, suggesting that both components are variable [5].

XY Per was classified as belonging to Herbig Ae/Be stars by Finkenzeller and Mundt [6]. Racine [7] obtained the first distance estimates for this star (r = 1700 pc) by using its spectroscopic parallax. According to other data, XY Per is a member of the RSF Per 4 association, whose distance is 350 pc [8]. The star exhibits an infrared excess [9], suggesting the presence of a fairly large amount of dust in its vicinity. XY Per was also identified with the point infrared source IRAS 03462+3849.

Spectral characteristics for the individual components of XY Per were described in the greatest detail by Herbig and Bell [10]. Previously, Herbig [2] found the brighter western (W) and the fainter eastern (E) components to be of spectral types A2 II and B6, respectively. Subsequently, Herbig and Bell [10] pointed out that the eastern component had the following spectral type: "middle A" and "late B" in the blue and red spectral ranges, respectively. These authors also noted that the western component (W) had a shell spectrum with a set of Fe II and Ti II absorption lines. Both components show emission in Hα. A remarkable feature of the spectrum is the infrared emission band (3.29 μm) of polycyclic aromatic hydrocarbons (PAHs) detected by Brooke *et al.* [11]. Attempts to detect radio activity of the star and circumstellar formations have failed. The star showed no detectable fluxes in the OH

* E-mail address for contacts: stas@astrin.uzsci.net

1063-7737/00/2604-0233$20.00 © 2000 MAIK "Nauka/Interperiodica"

lines at 1665, 1667, 1612 MHz [12] and in radio continuum [13].

Although XY Per has been known as a variable for several decades, its photometric behavior has not been studied adequately. Prolonged, but disconnected observations do not give a full picture of the variability of this star. Based on the long-term *UBVR* photometry of XY Per performed as part of the ROTOR program at Mount Maidanak, we therefore attempt to reveal characteristic features of its photometric behavior and consider a possible explanation in terms of currently available hypotheses. We also qualitatively interpret some of the star's spectral features by using a high-resolution spectrum obtained with the 6-m Special Astrophysical Observatory (SAO) telescope and analyze a CCD image. Preliminary results of our analysis of the photometric observations were published by Shevchenko *et al.* [14].

OBSERVATIONS

The *UBVR* photometry of XY Per was performed from 1985 until 1998 at Mount Maidanak using a pulse-counting photometer mounted on the 48-cm AZT-14 reflector. The instrumentation, observing and reduction techniques were described in more detail by Shevchenko [15]. The observations were carried out by a differential method [16] with the comparison star BD+38°812 ($V = 10\overset{m}{.}058$, $U–B = 0\overset{m}{.}025$, $B–V = 0\overset{m}{.}587$, $V–R = 0\overset{m}{.}544$). More than 850 measurements were obtained for this star over the entire period of its observations. The rms error of a single measurement was $V = B–V = 0\overset{m}{.}01$, $U–B = 0\overset{m}{.}03$, and $V–R = 0\overset{m}{.}015$. The *UBVR* photometry of XY Per is accessible via Internet from anonymous ftp://sun.astro.wesleyan.edu/pub/ttauri/HAEBE.

The spectroscopic observations of XY Per were carried out with the spectrograph of the 6-m SAO telescope. The spectrum in the wavelength range 3600–6700 Å was taken on November 18, 1991 (JD 2448579), on A700u film with a signal-to-noise ratio of 60/1, a dispersion of 27 Å mm^{-1} near Hγ, and resolution of 0.7 Å. The spectrum was reduced on the measuring–computing systems at SAO (Russian Academy of Sciences) and Astronomical Institute (Academy of Sciences of Uzbekistan).

Direct CCD images of XY Per were obtained on September 2, 1998 (JD 2451694), at Mount Maidanak on the AZT-22 (D = 1.5 m) reflector using the Meade Pictor 416XT CCD camera (768 × 512 pixels, the pixel size is 9 μm). We obtained two images in *R* (the exposure times were 60 and 180 s) and one image in *I* (60 s) at the *f*/7.7 focus, which provides a $0\overset{''}{.}16$ pixel^{-1} scale.

CCD OBSERVATIONS

Our CCD observations aimed at surveying the immediate vicinity of the star. Figure 1 shows two images of the XY Per field on different scales. Figure 1a is a reproduction of part of the Palomar Observatory Sky Survey (POSS) map retrieved from the Digital Sky Survey database. The image was taken in the red, and the field is $10' \times 10'$ in size. The image in Fig. 1b is a portion of the CCD image in *R*.

Collectively, these images show a complex structure of the emission nebula surrounding XY Per. On the blue POSS map, this nebula is brighter than on the red one. The positions and orientation of the emission-nebula fragments relative to the absorbing-cloud fragments seen in Fig. 1a confirm that XY Per lies at the edge of the dust cloud L1449. A nebular fragment closer to the star which is barely seen on the POSS map, becomes visible on the CCD image (Fig. 1b). Goodrich [17] provides a CCD image of this region in the [Si II] 6725 Å line. Only this fragment has a fairly high surface brightness on this image, whereas the remaining nebular fragments are unseen. We see from Figs. 1a and 1b that the major axis of the fragment close to the star roughly coincides in direction with the major axis of the fragment further from the star. We may therefore assume that they are the remnants of two different shells ejected at different epochs.

ANALYSIS OF THE PHOTOMETRIC OBSERVATIONS

The photometric behavior of the star was analyzed by many authors, including Boyd [5], Beyer [18], Hoffmeister [19], and Martynov [20]. These authors pointed out that XY Per could be at maximum light for years, while during activity periods its brightness varied with an amplitude of $1^m – 1\overset{m}{.}3$ and exhibited 18–36 and 300–500-day waves. Over the period of our observations, the brightness of XY Per was not in quiescence. The peak-to-peak variability amplitude was $\approx 1^m$ in *V*. The overall light curve for fourteen years of observations is shown in Fig. 2. As we see from the figure, the mean brightness of the star varied from year to year. Both average points and points of maximum light reveal this effect.

Our light curve, like that of Beyer [18], exhibits waves with characteristic time scales of several tens of days. The most typical portions of the light curve for 1988 and 1993 showing this phenomenon are displayed in Fig. 3. The light variations in Fig. 3a are nonharmonic in shape and increase in amplitude. A wave with a characteristic time scale of ≈38 days is seen on the 1993 light curve (Fig. 3b). In our search for a period, we identified several epochs at which waves of approximately equal duration were observed. This set included the 1988, 1989, 1994, and 1995 observations.

We used the CLEAN algorithm [21, 22] to refine the period of the light variations. The significance of the period was estimated by analyzing the LS spectrum in Lomb's representation [22]. The formal parameter *Q* [22] generalized to unevenly sampled time series was

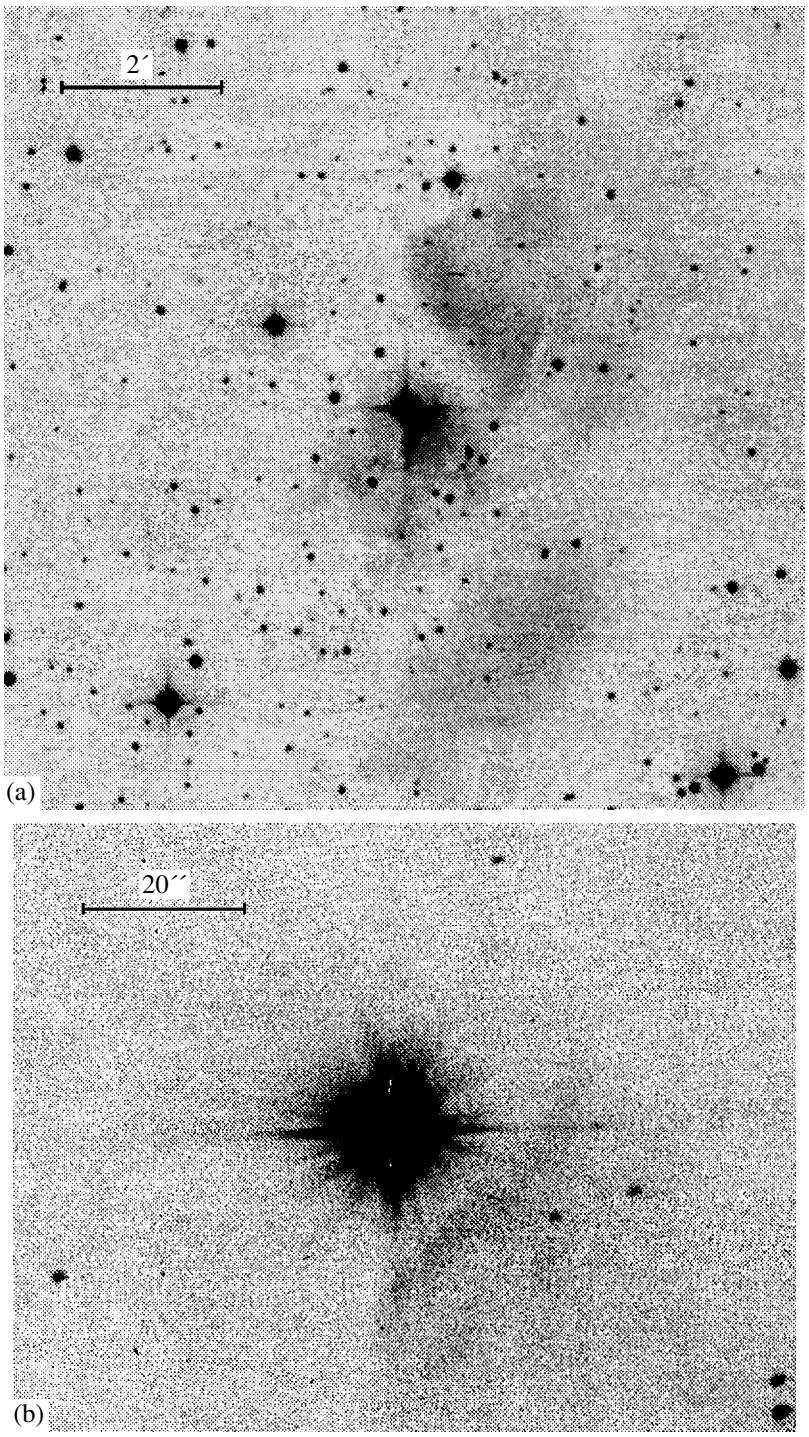

Fig. 1. Images of the XY Per field from different sources with different resolutions: (a) a $10' \times 10'$ region of the sky in the red retrieved from the Digital Sky Survey database; (b) the CCD image of XY Per in *R* obtained with the Meade Pictor 416XT CCD camera.

used as the significance test; this parameter is obtained after Lomb's periodogram has been analyzed. The normalized parameter *Q* shows the percentage of cases in which a random time series exhibits peaks of the same height as those detected in the series under study. Thus, the smaller the parameter *Q*, the higher the probability of the existence of a period. We consider a period to be significant if $Q < 5\%$. The procedure for CLEAN application and estimating the significance of detected periodicities was described in [23].

The power spectrum obtained after analyzing the set of 1988–1995 observations is shown in Fig. 4a. The peak corresponding to the probable period $P = 22^{d}.7252 \pm 0^{d}.002$ can be identified in the power spectrum. An analysis of the same data using the LS spectrum also reveals a peak at this frequency, but the peak is slightly split in this case. This probably suggests that the observed periodicity is a superposition of two close (in frequency) periodicities present at different epochs. The significance of the period $P = 22^{d}.7252$ was estimated by using the LS spectrum to be $Q = 0.11\%$, suggesting a high significance of this period. Figure 4b shows the phase *V* light curve folded with the period found. The periodicity amplitude is $0^{m}.3$ (*V*). The period we found can also be identified in *B* and *R*.

In addition, the light curve of XY Per exhibits irregular Algol-like minima 15–20 days in duration. We recorded two such minima sequentially in 1991 and 1992. Figure 5a shows a portion of the *R* light curve for 1991, in which one of such minima is seen. The amplitude of this minimum in *V* is $0^{m}.5$. After egress from the minimum, the star was still in a state of reduced brightness for some time, which is also typical of other UX Ori stars. Voshchinnikov and Grinin [24] believe this pattern of photometric behavior to suggest that the circumstellar formation eclipsing the star has a compact central core and an extended shell. In addition, asymmetry in the photometric behavior before and after the minimum suggests that the shell surrounding the central core is elongated in shape. In the case of the 1991 minimum, the light variations immediately after egress from the local minimum were almost periodic in pattern, which shows up most clearly in *R*. We do not compare the photometric and color behaviors of XY Per during the 1991 and 1992 minima, because, unfortunately, no observations in the central part of the 1992 minimum are available.

The color behavior in a two-color (*U–B*)–(*B–V*) diagram during the 1991 minimum is shown in Fig. 5b. The arrows indicate the direction of change in color indices; the points are numbered sequentially. We see from Fig. 5b that, initially, the color variations were generally consistent with the hypothesis in which the reddening was attributed to an eclipse of the star by dust circumstellar formations [25]. We also see from the figure that the color indices do not turn blueward at minimum light. This apparently stems from the fact that the minimum is not deep enough, because this effect is usually observed for Algol-like minima with amplitudes $>1^{m}.0$–$1^{m}.5$. Points *8* and *9* correspond to minimum light. Two days later, an ultraviolet excess appeared with *B–V* increased only slightly. This color behavior during the appearance of an ultraviolet excess is typical of the radiation from a heated gas shell. Below, we consider a possible reason for the appearance of this ultraviolet excess.

ANALYSIS OF THE SPECTROSCOPIC OBSERVATIONS

Our spectrum of XY Per contains spectral lines of both its components. A large number of lines both with excitation potentials corresponding to the spectral classification A2 II + B6 [7] and with lower excitation potentials are seen in the spectrum. A list of detectable lines and equivalent widths of the most intense lines are given in the table. The table also gives the correspond-

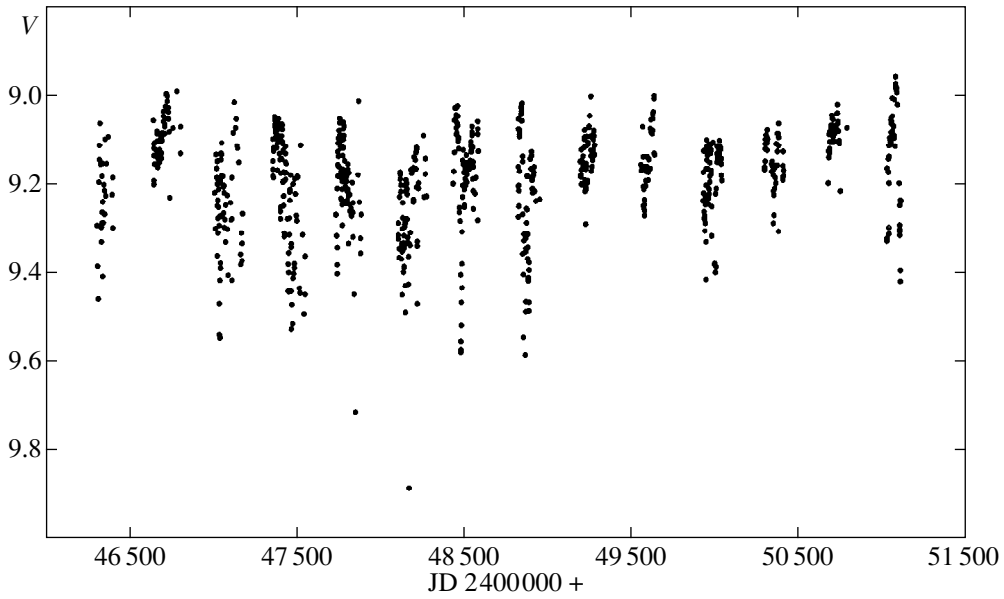

Fig. 2. The *V* light curve of XY Per for 1985–1998.

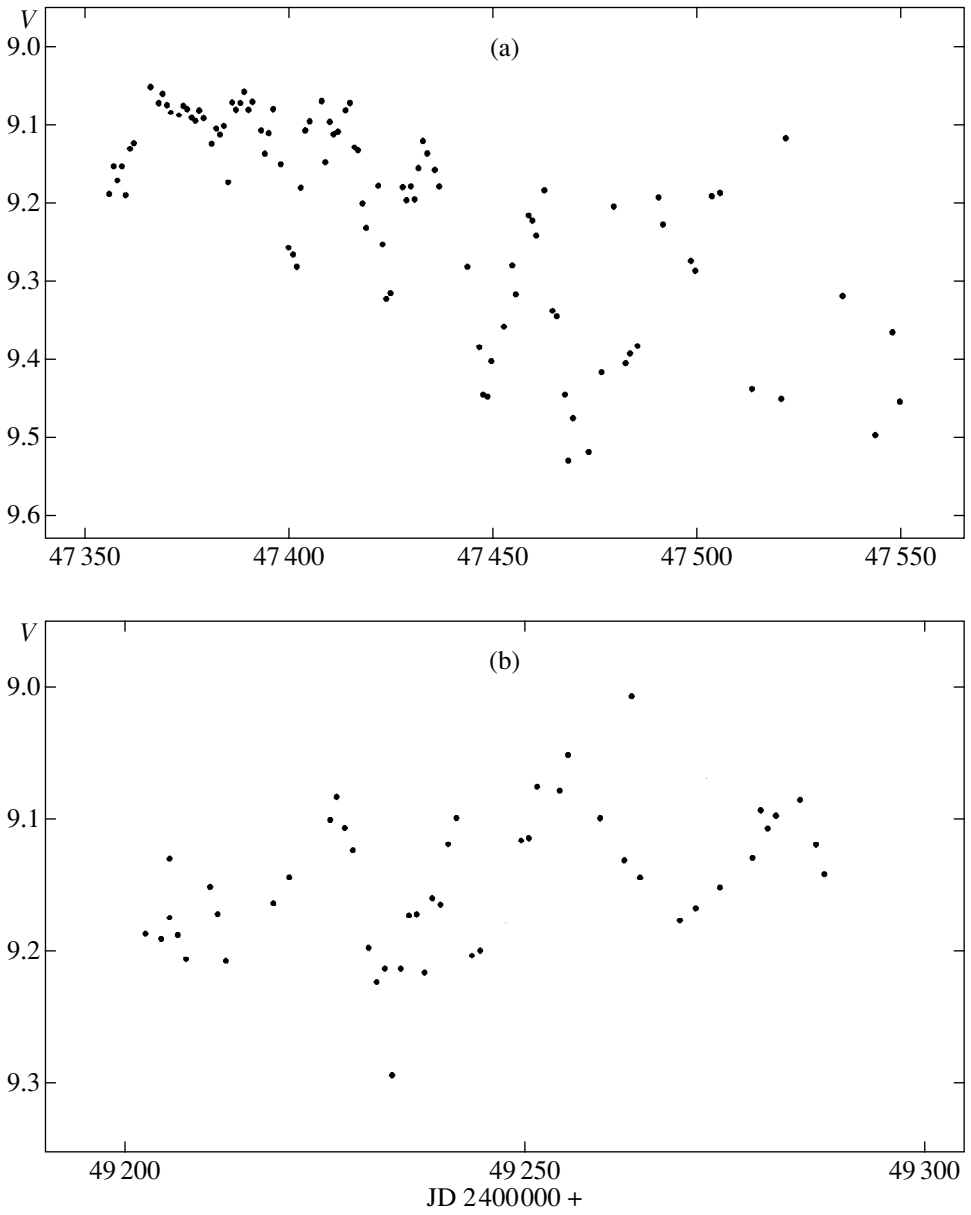

Fig. 3. Portions of the *V* light curve for XY Per showing a quasi-periodicity in (a) 1988 and (b) 1993.

ing excitation potentials (in eV). The Balmer series up to the H18 line is well represented. Of all hydrogen lines, only Hα is in emission; its equivalent width is $E(W_\lambda) = -0.8$ Å. The Hα profile is shown in Fig. 6a. The Hα line has a double peak separated by a central absorption. Although no photometric observations were performed on this date (JD 2448579), the star was apparently at maximum light, because observations on adjacent dates are available: $V = 9^m.19$ (JD 2448575) and $V = 9^m.08$ (JD 2448584). In comparison with the data of other authors, this is the lowest line intensity. The highest intensity is given by Avramenko and Pugach [4]: $E(W_\lambda) = -7.8$ Å. As we see from the comparison, although Hα has a moderate intensity, its equivalent width can change by almost an order of magnitude.

As we see from the table, there are a large number of Fe I and Fe II lines in the spectrum. According to Herbig and Bell [10], these lines, along with Ti II lines, belong to the western (W) component and its shell. The strongest green Fe II 4583.89, 5018.44, and 5169.03 Å absorption lines have an asymmetric profile (Figs. 7a–7c) with a more pronounced red wing. The red wings of these lines stretch from the line center to velocities of 240–290 km s^{-1}, while their blue wings reach a mere 150 km s^{-1}, on the average. Thus, the red wings of these shell lines suggest gas accretion onto the star with

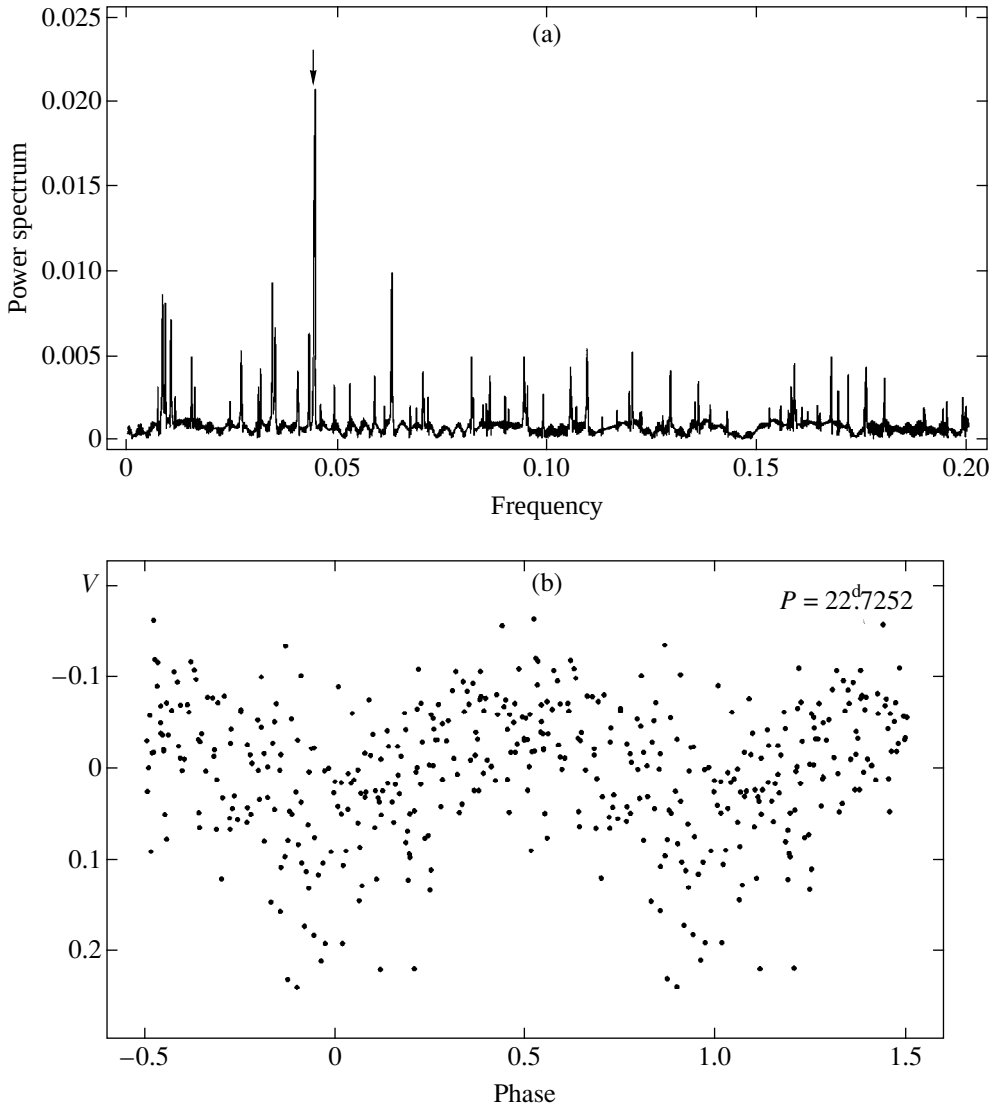

Fig. 4. (a) The power spectrum obtained by using the CLEAN algorithm from the set of 1988–1995 observations and (b) the phase light curve folded with period $P = 22^{d}.7252$. The peak corresponding to the probable period is marked by an arrow in the power spectrum.

velocities of 90–140 km s^{-1}. Small emission peaks, which are also redshifted, are seen at the center of these lines. The infrared Ca II triplet lines [26] also have such features in their profiles. Of course, it may well be that these peaks are spurious and result from a superposition of the main line profile and the profile of the redshifted line component. However, the presence of more pronounced peaks in the Mg II 4481.33 and He I 5875.65 Å (Fig. 6b, 6c) lines, as well as the existence of the Fe II 6247.56 Å emission line (Fig. 7f), suggests that these emission components are real. The presence of emission components in lines with different excitation potentials indicate that the gas shell in which they originate is heated very nonuniformly.

The spectrum also exhibits broad Mg II 4481.33 Å and He I 5875.65 Å absorption lines (Fig. 6b, 6c) with narrow emission components at their centers. We believe the nature of these emission peaks to be the same as that for the iron lines. In addition, the He I 5875.65 Å line has a characteristic blueshifted emission bulge. Mg II 4481.33 Å is a photospheric line, while He I 5875.65 Å, according to Boehm and Catala [27], is not photospheric in nature, because its intensity exceeds appreciably the line intensity for a B6 star. At the same time, He I 5875.65 Å has a width corresponding to a B6 star, suggesting the formation of this line near the photosphere. However, Boehm and Catala [27] believe the blueshifted emission bulge to originate in the heated expanding chromosphere.

Apart from Hα, the spectrum of XY Per exhibits several more emission lines, two of which were identified with Fe I 3554.929 Å and Fe II 6247.56 Å (Figs. 7e, 7f). The Fe I 3554.929 Å line is broad and, like Hα, is separated by a central absorption. It appears to be formed in the same region.

Absorption bands of an as yet unidentified interstellar agent were also detected in the spectrum of XY Per (Figs. 6a, 6d). Lines of unidentified interstellar molecules are listed in [28]. They are also encountered in other Herbig Ae/Be stars [29, 30]. At the same time, no broad absorption dip of a similar nature has been detected near λ4430 Å. The spectrum exhibits narrow Na I 5889.95 and 5895.92 Å interstellar lines (Fig. 6c); however, weak absorption components, which could be circumstellar in origin, can be suspected to be present in the red wings. In the opinion of Sorelli *et al.* [31], the formation of the circumstellar Na I 5889.95 and 5895.92 Å lines is coupled with the evaporation of cometary bodies rotating around the star.

DISCUSSION

The small angular separation between the components (1″.3) in the binary system XY Per complicates a separate photometric study of the components, while the lack of such observations does not allow its fundamental parameters, such as luminosity, radius, distance, etc., to be determined more accurately.

In the course of our studies, we failed to separate different types of variability between the components. XY Per exhibited a stochastic variability for about 10% of the observing time, which can be attributed to the simultaneous photometric variability of both components. Smoother variations caused by the variability of both components are also possible. Although the smooth year-to-year variations in the mean brightness of XY Per can be caused by light variations of the same order of magnitude in one of the components, such a phenomenon is also observed in other Herbig Ae/Be stars [23]. We may therefore assume this phenomenon to have a different nature. Since a certain part of the stellar luminosity is associated with the accretion of circumstellar material, the slow variations in mean brightness can be attributed to variations in the mean rate of nonstationary accretion. Grinin *et al.* [32] believe that such a long-term photometric variability of Herbig Ae/Be stars has two-component activity cycles and can be caused by the existence in binary systems of unequal (in power) mass flows accreted onto the binary components. The existence of such flows in binary systems was hypothesized by Artymovicz and Lubov [33].

The Algol-like minima on the light curve of XY Per appear to have the same nature as those in UX Ori, which is the prototype of a whole class of stars. The nature of such minima is associated with an eclipse of the star by circumstellar formations in an inhomogeneous dust disk [25]; the disk must be seen edge-on or

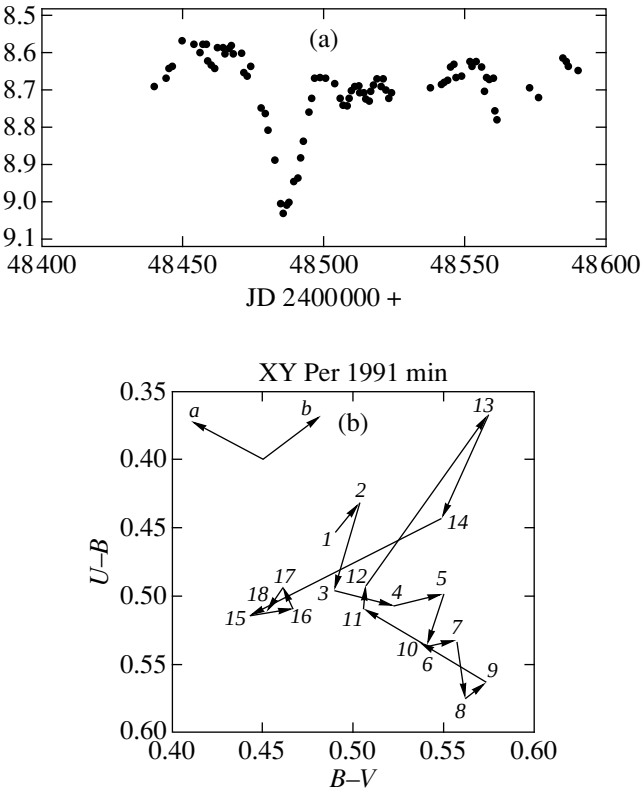

Fig. 5. (a) A portion of the *R* light curve of XY Per for 1991 and (b) the color behavior in a *U–B*, *B–V* diagram during the Algol-like minimum of 1991. The arrows (*a* and *b*) in the upper left corner indicate the effect of interstellar dust and gas radiation on the color indices, respectively.

nearly edge-on. Lamzin [34] believes that there is a flattened gas–dust shell instead of the disk. In comparison with other stars of this type, the minima in XY Per have a smaller amplitude, and their frequency of occurrence is lower. This implies that either the disk has already strongly evolved and does not contain a great number of large dust fragments, or it has a larger inclination to the line of sight than that for other stars of this type. At the same time, according to Finkenzeller and Mundt [6] and other authors, the magnitude difference between the components can occasionally reach $2^m - 2^m.5$. Since the spectral type of most stars with Algol-like minima is later than B9, these minima may be assumed to belong to the western (W) component of spectral type A2 II. However, there is evidence for the existence of a very deep photometric minimum in XY Per with a total amplitude up to $3^m.5$ [35], suggesting that Algol-like minima may occur in both components.

During the 1991 minimum, an ultraviolet excess appeared in the radiation from XY Per. This effect was also observed during the minima of WW Vul by Zaitseva and Lyuty [36]. These authors believe that the appearance of an ultraviolet excess is coupled with an increase in the contribution of the hot gas component to

Intense lines in the XY Per spectrum

Species	λ, Å	EW_λ, Å	eV	Species	λ, Å	EW_λ, Å	eV	Species	λ, Å	EW_λ, Å	eV
Absorption lines											
Fe I	3631.46	0.1	4.37	Fe I	3998.05		5.79	Ti II	4501.27		3.87
Ti II	3685.20		3.96	Ti II	4025.14			Fe II	4508.28		5.60
H 18	3691.55		13.55	Fe II	4032.95			Fe II	4522.62		5.58
H 17	3697.15	0.1	13.54	Fe I	4065.39		6.32	Ti II	4533.97		
H 16	3703.86	0.2	13.54	Cr II	4077.50			Fe II	4549.47	0.1	5.55
H 15	3711.98	0.3	13.53	Hδ	4101.74	2.9	13.21	Fe II	4583.85	0.2	5.51
H 14	3721.95	0.4	13.52	Si II	4130.96		12.83	Hβ	4861.33	3.3	12.74
H 13	3734.37	0.6	13.51	Fe I	4132.06		4.61	Fe II	4923.92	0.1	5.41
Ti II	3741.64		4.89	Fe II	4173.47		5.55	Fe II	5018.44	0.2	5.36
H 12	3750.15	0.7	13.50	Fe II	4178.87		5.54	Fe II	5169.03	0.3	5.29
Ti II	3759.20		3.91	Ca I	4226.76		2.93	Fe II	5316.71	0.1	
Ti II	3761.32		3.87	Fe II	4233.17	0.1	5.51	ISA*	5780.5		
H 11	3770.63	1.1	13.48	Fe I	4271.76		4.39	ISA	5797.13		
H 10	3797.91	1.7	13.45	Fe II	4273.32			He I D3	5875.62		23.06
Fe II	3814.12			Ti II	4290.23		4.06	Na I D2	5889.95	0.1	2.11
Ti II	3814.58			Ti II	4301.93			Na I D1	5895.92	0.1	2.10
H 9	3835.40	2.4	13.42	Fe II	4303.17		5.58	ISA	6283.0		
Si II	3856.09		10.07	Ti II	4314.98			Fe II	6456.38		
Fe II	3872.76			Fe II	4385.38			ISA	6615		
H 8	3889.06	2.9	13.38	Fe II	4416.82			Emission lines			
Ti II	3913.46		4.28	Hγ	4340.47	2.5	13.01				
Ca II K	3933.66	0.8	3.15	Ti II	4444.56			Fe I	3554.93	−0.8	6.32
Fe I	3955.35		6.42	Ti II	4468.49		3.90	Fe II	6247.56		
Ca II H	3968.47		3.15	Mg II	4481.33		11.63	Hα	6562.85	−0.8	12.09
Hε	3970.07	3.1	13.31	Fe II	4491.40						

* ISA denotes unidentified interstellar absorption lines.

the total stellar radiation and bears no relation to the dust component. However, the appearance of an ultraviolet excess in a certain segment of the minimum leads us to conclude (at least in the case of XY Per) that this relationship does exist. Such a color behavior can be explained by assuming that the eclipsing dust fragment or its part fell in the accretion zone. The associated energy release caused an additional heating of the surrounding gas shell, which gave rise to the ultraviolet excess. In this case, however, it is required that the circumstellar formation move in a highly eccentric orbit, but this assumption in our study is premature.

The detected quasi-periodic light variations with an amplitude of $0^m.3$ and period $P = 22^d.7252$, which had been observed for several years, are most difficult to interpret. This period is too long to be coupled with the rotation of the star itself, because, according to Herbig and Bell [10], XY Per has $V\sin i$ = 95–130 km s^{-1}, which corresponds to a period <1^d if the star rotates as a solid body. If the mass of the central object is assumed to be (3–4)$M_\odot$ (as is the case for Herbig Ae/Be stars), then a separation of ≈0.2 AU (48$R_\odot$) and a velocity of ≈100 km s^{-1} correspond to a period of ≈23^d in the case

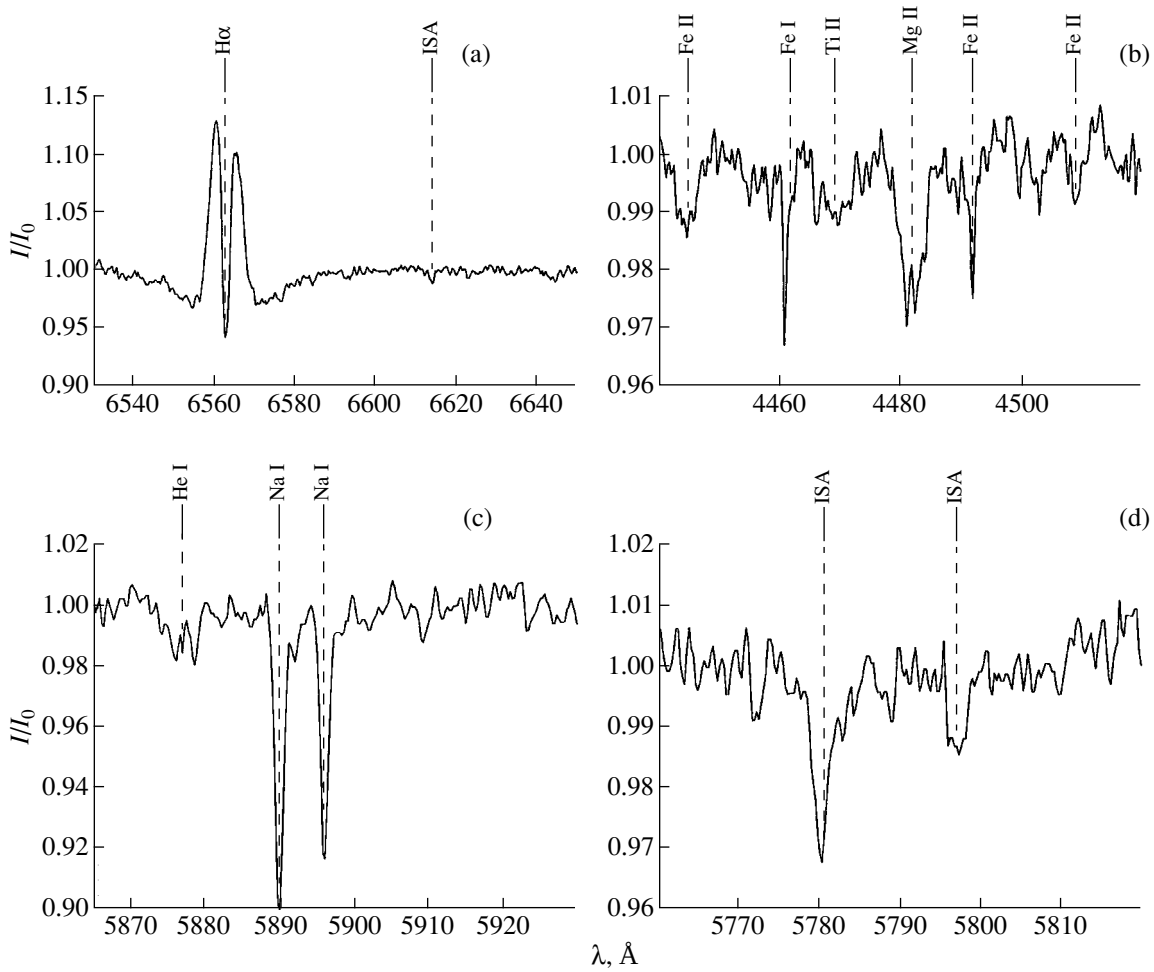

Fig. 6. Portions of the XY Per spectrum near the following lines: (a) Hα, (b) Mg II 4481.33 Å, (c) He I 5875.65 Å, and (d) diffuse interstellar molecular absorption bands (ISA) at λ5780.55 Å and 5797.13 Å.

of Keplerian rotation. If the nature of the quasi-periodic variations is associated with the rotation of circumstellar formations around the central star, the light variations must be similar in shape to harmonic oscillations, which is not observed (Fig. 3a).

Quasi-periodic variations in the rate of energy release can be one of the possible sources of periodic light variations if the accreted circumstellar formations are regular in structure. The existence of regular structures in circumstellar formations is indirectly confirmed by the light-curve shape after egress from the Algol-like minimum of 1991 (Fig. 4a), where quasi-periodic light variations are also observed. This interpretation slightly differs from that offered by Melnikov [23]. The decline in mean brightness during the periodic light variations in 1988 (Fig. 2a) is consistent with the assumption of periodic variations in accretion rate, because we see the accretion disk nearly edge-on and such a brightness decline implies a larger amount of accreted matter on the line of sight. At the same time, the variations in mean brightness may be coupled with variability of the other component.

The separation between the components in XY Per is large. Even at a minimum distance estimate of 350 pc for this system, the separation between the components is approximately 500 AU. The components with their circumstellar environments may therefore be assumed to affect each other only slightly. The western component of XY Per (W) of spectral type A2 II shows evidence of a supergiant and apparently has a more developed gas–dust shell than the eastern component (E) of spectral type B6. Accordingly, the problem of the evolutionary status of each component arises. According to the calculations by Palla and Stahler [37], A stars become visible during their contraction, when they have not reached the zero-age main sequence (ZAMS), whereas B stars become visible only when they are very close to the ZAMS. It should thus be assumed that, if the components of XY Per have the same age, then the eastern component (E), which is of an earlier spectral

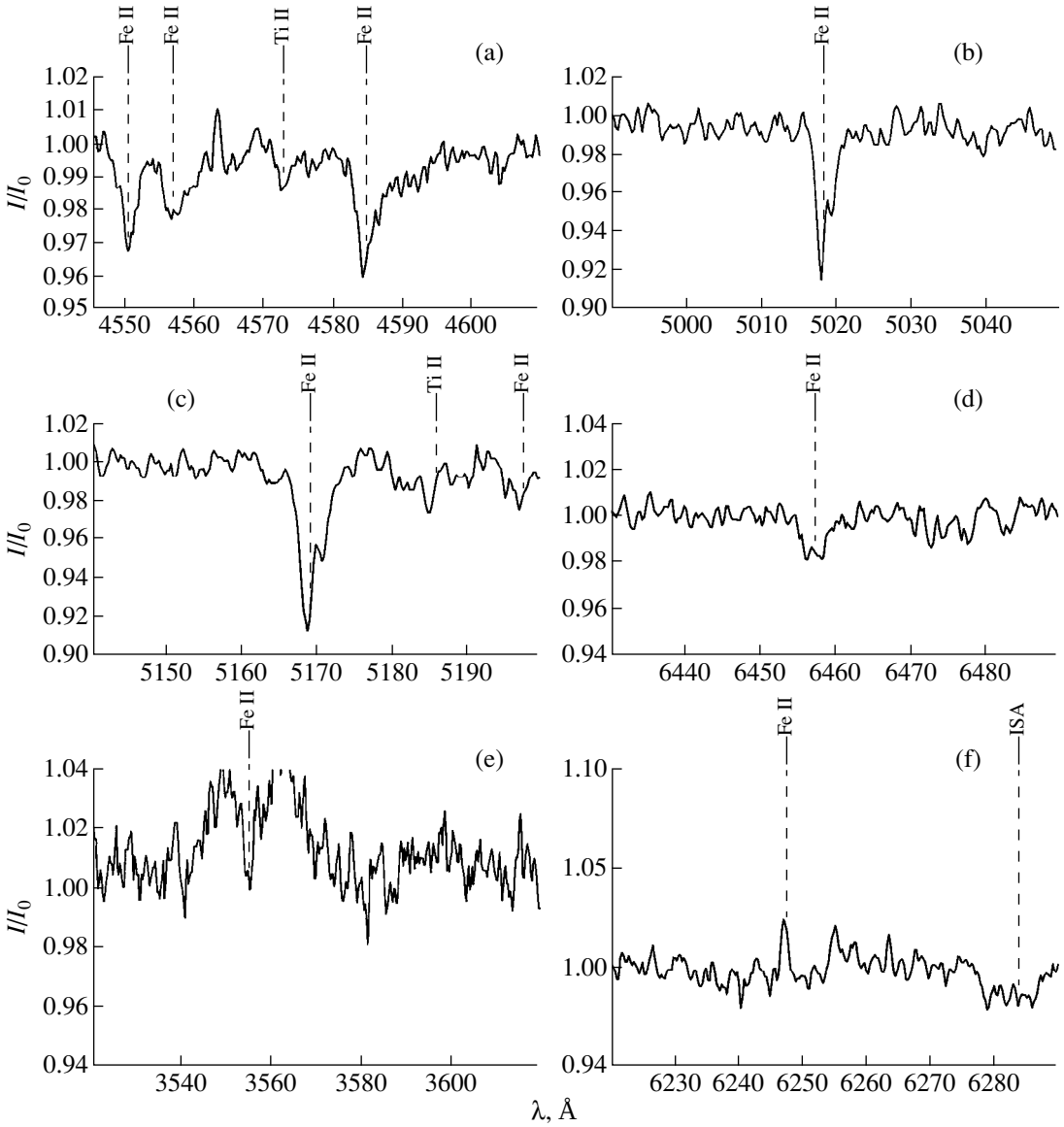

Fig. 7. Portions of the XY Per spectrum near the following iron lines: (a) Fe II 4583.89, (b) Fe II 5018.44, (c) Fe II 5169.03, (d) Fe II 6456.38, (e) Fe I 3554.929, and (f) Fe II 6247.56.

type, evolved toward the ZAMS more rapidly than the (W) component.

CONCLUSION

Our analysis of the 14-year-long series of observations has shown that the observed photometric variability of XY Per can be divided into three components:

(1) smooth year-to-year variations in mean brightness;

(2) quasi-periodic variations with a characteristic time scale of 20–40 days and an amplitude of $0^m.3$;

(3) Algol-like minima with a duration of 15–20 days and an amplitude of $0^m.5$ in *V*.

During the Algol-like minimum of 1991, an ultraviolet excess appeared on the ascending branch of the light curve. The color behavior suggests that the ultraviolet excess can be caused by an increase in the contribution of the radiation from a hot gas shell. The required energy could have been released through the accretion of an additional portion of circumstellar material.

Our spectroscopic observations reveal both photospheric lines, including Fe I ones, and numerous Fe II and Ti II shell lines in the spectrum. There are emission peaks at the centers of the Mg II 4481.33 and He I 5875.62 Å absorption lines and the strongest Fe II lines. Asymmetry in the shell-line profiles suggests the accretion of circumstellar material with a velocity

of ≈100 km s^{-1}. The Hα emission line is separated by a central absorption and has the equivalent width $E(W_\lambda) = -0.8$ Å. A comparison with the data of other authors shows that its intensity changed by almost an order of magnitude.

We did not set the objective of performing theoretical calculations which would confirm a particular hypothesis. We only attempted to qualitatively describe particular observational facts in terms of currently available hypotheses. More specifically, we believe that an approach is possible in which the observed phenomena differing in behavior (for example, different patterns of photometric variability) can be explained by invoking different hypotheses.

ACKNOWLEDGMENTS

This study was supported by the Civil Research Foundation (grant no. ZP1-341). We wish to thank K.N. Grankin, who carried out the photometric observations, E.L. Chentsov for help with the spectroscopic observations, and A. Zheleznyak for help with the CCD observations. We are also grateful to M.A. Ibragimov for a discussion. We used data from the SIMBAD (Strasbourg, France) and Digital Sky Survey (USA) databases.

REFERENCES

1. P. Corporon, Candidate's Dissertation (1998).
2. G. H. Herbig, Trans. IAU **8**, 807 (1954).
3. S. I. Bailey, Harv. Circl. **225**, 1 (1921).
4. S. I. Avramenko and A. F. Pugach, Astrometr. Astrofiz. **44**, 9 (1981).
5. C. D. Boyd, Harv. Bull. **904**, 18 (1936).
6. U. Finkenzeller and R. Mundt, Astron. Astrophys., Suppl. Ser. **55**, 109 (1984).
7. R. Racine, Astron. J. **73**, 233 (1968).
8. R. Herbertz, H. Ungerechts, and G. Winnewisser, Astron. Astrophys. **249**, 483 (1991).
9. D. A. Allen, Mon. Not. R. Astron. Soc. **161**, 145 (1973).
10. G. H. Herbig and K. R. Bell, Lick Obs. Bull., No. 1111 (1988).
11. T. Y. Brooke, A. T. Tokunaga, and S. E. Strom, Astron. J. **106**, 656 (1993).
12. G. M. Rudnitskii, Astron. Zh. **53**, 1225 (1976).
13. S. L. Skinner, A. Brown, and R. T. Stewart, Astrophys. J., Suppl. Ser. **87**, 217 (1993).
14. V. S. Shevchenko, K. N. Grankin, M. A. Ibragimov, *et al.*, Astrophys. Space Sci. **202**, 137 (1993).
15. V. S. Shevchenko, *Herbig Ae/Be Stars* (FAN, Tashkent, 1989).
16. V. Straizis, *Multicolor Stellar Photometry* (Mokslas, Vilnius, 1977).
17. R. W. Goodrich, Astrophys. J., Suppl. Ser. **86**, 499 (1993).
18. M. Beyer, Astron. Nachr. **263**, 71 (1937).
19. C. Hoffmeister, Astron. Nachr. **278**, 24 (1949).
20. D. Ya. Martynov, Izv. Astron. Obs. Engelgardta **26**, 20 (1951).
21. D. H. Roberts, J. Lehár, and J. W. Dreher, Astron. J. **93**, 968 (1987).
22. V. Yu. Terebizh, *Analysis of Astrophysical Time Series* (Nauka, Moscow, 1992).
23. S. Yu. Melnikov, Pis'ma Astron. Zh. **23**, 918 (1997).
24. N. V. Voshchinnikov and V. P. Grinin, Astrofizika **34**, 181 (1991).
25. W. Wenzel, *Non-Periodic Phenomena in Variable Stars*, IAU Coll. No. 4, Ed. by. L. Detre (Acad. Press, Budapest, 1969), p. 61.
26. F. Hamann and S. E. Persson, Astrophys. J., Suppl. Ser. **82**, 285 (1992).
27. T. Boehm and C. Catala, Astron. Astrophys. **301**, 155 (1995).
28. S. A. Kaplan and S. B. Pikel'ner, *Interstellar Medium* (Izd. Fiz.-Mat. Lit, Moscow, 1963).
29. R. Poetzel, R. Mundt, and T. P. Ray, Astron. Astrophys. **262**, 229 (1992).
30. S. Yu. Melnikov, V. S. Shevchenko, K. N. Grankin, *et al.*, Astron. Zh. **73**, 390 (1996).
31. C. Sorelli, V. P. Grinin, and A. Natta, Astron. Astrophys. **309**, 155 (1996).
32. V. P. Grinin, A. N. Rostopchina, and D. N. Shakhovskoi, Pis'ma Astron. Zh. **24**, 925 (1998).
33. P. Artymovicz and S. H. Lubov, Astrophys. J. Lett. **467**, L77 (1996).
34. S. A. Lamzin, Private communication (1999).
35. G. P. Zakharov, Perem. Zvezdy **9**, 396 (1954).
36. G. V. Zaitseva and V. M. Lyuty, Pis'ma Astron. Zh. **23**, 277 (1997).
37. F. Palla and S. W. Stahler, Astrophys. J. **418**, 414 (1993).

Translated by V. Astakhov

Astronomy Letters, Vol. 26, No. 4, 2000, pp. 244–249. Translated from Pis'ma v Astronomicheskiĭ Zhurnal, Vol. 26, No. 4, 2000, pp. 294–300.

Continuum Spectrum of the Star Θ^1 Ori C

E. A. Vitrichenko*

Space Research Institute, Russian Academy of Sciences, ul. Profsoyuznaya 84/32, Moscow, 117810 Russia

Received August 16, 1999

Abstract—Published photoelectric measurements over a wide wavelength range (0.36–18 μm) are used to study the continuum spectrum of the star Θ^1 Ori C. The model that assumes the following three radiation sources is consistent with observations: (1) a zero-age main-sequence O7 star (object 1) of mass $M_1 = 20\ M_\odot$, radius $R_1 = 7.4\ R_\odot$, effective temperature $T_1 = 37\,000$ K, and absolute bolometric magnitude $M^1_{\rm bol} = -7\overset{m}{.}7$; (2) object 2 with $M_2 = 15\ M_\odot$, $R_2 = 16.2\ R_\odot$, $T_2 = 4000$ K, and $M^2_{\rm bol} = -5\overset{m}{.}1$; and (3) object 3 with $R_3 = 10\,700\ R_\odot$, $T_3 = 190$ K, and $M^3_{\rm bol} = -0\overset{m}{.}6$. The visual absorption toward the system is $A_V = 0\overset{m}{.}95$ and obeys a normal law. The nature of objects 2 and 3 has not been elucidated. It can only be assumed that object 2 is a companion of the primary star, its spectral type is K7, and it is in the stage of gravitational contraction. Object 3 can be a cocoon star and a member of the system, but can also be a dust envelope surrounding the system as a whole.

Key words: *stars—structure and evolution*

INTRODUCTION

The star Θ^1 Ori C (=HD 37022) is the most interesting member of the Orion Trapezium. It excites the glow of the Orion Nebula, possibly, together with the star Θ^2 Ori A. Several remarkable features of the star attract particular attention.

First, the star is very young. The age of the Trapezium stars is estimated to be $\sim(2–3) \times 10^5$ years [1, 2]. According to Conti [3], Θ^1 Ori C lies near the zero-age main sequence (ZAMS) in the Hertzsprung–Russell diagram.

Second, the star is peculiar in that, on the one hand, there is no clear evidence of its binary nature, because its radial velocity is constant [3], and, on the other hand, it exhibits periodic variations in several physical parameters.

Spectral variations were first detected by Conti [3]. The He II 4686 line profile changed radically on a characteristic time scale of several days. These variations involved the appearance and disappearance of a violet-shifted emission component in the line. Stahl *et al.* [4] investigated the emission component of Hα and found it to vary with a period of 15.4 days. Walborn and Nichols [5] detected variations in the C IV 1548 and 1551 line profiles with a period of 15.41 ± 0.02 days, which is in excellent agreement with the period of variations in the Hα emission. The systematic change of the spectral type from O6 to O4 in seven days [6] also agrees with this period. Gagne *et al.* [7] made the most startling discovery. They found the X-ray flux from the star to vary with a period of 16.0 ± 3.8 days, in agreement with the above period. Babel and Montmerle [8] proposed a model of an oblique rotator with the star's surface magnetic field B = 300 G to explain this phenomenon.

Here, our objective is to construct the star's continuum spectrum and to determine which system's components contribute to the formation of the observed continuum by using published photometric data.

OBSERVATIONAL DATA

The observations were taken from [9, 10] (see Table 1). The bands, as designated by Straizis [11], and effective wavelengths are listed in the first and second columns, respectively. The third column gives the colors from [9]; we assumed $V = 5\overset{m}{.}13$. The fourth column contains the colors from [10]. The colors for an unreddened O7 star [11] are given in the fifth column. The content of the last four columns is described below.

An examination of Table 1 reveals a discrepancy in the *KL*-band data taken from the two sources. This can be explained both by a difference in the photometric systems and by variability of the star in these bands.

Ney *et al.* [10] observed the star on four dates. We averaged these observations, but the scatter of individual observations is rather large. For example, three measurements were made in *Q*. The first two were performed with a 25″ aperture, and the *Q* magnitudes are $-5\overset{m}{.}1$ and $-4\overset{m}{.}8$. Both measurements are in satisfactory agreement. The third measurement was made with a

* E-mail address for contacts: vitrich@nserv.iki.rssi.ru

12″ aperture, and the Q magnitude is $-1\overset{m}{.}9$. If an extended source emitted radiation in this band, then the star would be fainter through a smaller aperture, while actually it is brighter. So, this is not the point. No measurement errors are given in the paper, but an excessively large scatter of measurements confirms the assumption that the star is variable in the infrared.

The H magnitude of the star was taken from [12], because it is absent in other papers.

Stebbins and Whitford [13] provide photometric *UVBRGI* measurements of the star, but we did not use them here, because the spectral range of these bands is covered by the *UBVRI* observations [9].

ANALYSIS OF THE CONTINUUM SPECTRUM

Let us determine the interstellar absorption. For an O star, the colors in *UBVR* depend weakly on temperature, while their wavelength dependence is strong. This makes it possible to determine both the interstellar reddening A_V and the dereddened magnitude V_0 of the primary star with a high accuracy. We make use of the fact that the contribution of the other two components in the system is small for the above bands.

The method of determining A_V and V_0 was described by Vitrichenko and Larionov [14]. In our case, this method involves forming a set of four equations for photometric *UBVR* measurements:

$$\Delta m(\lambda) = x\mathrm{A}(\lambda) + V_0. \quad (1)$$

Here, $\Delta m(\lambda)$ is the difference between the observed magnitudes and the magnitudes for an unreddened O7 star with a V magnitude of 0^m. The quantity x is the equivalent geometrical thickness of the interstellar dust, which is equal to unity for a normalized interstellar reddening law $\mathrm{A}(\lambda)$.

The differences $\Delta m(\lambda)$ are given by

$$\Delta m(\lambda) = V + (m_i - V) - (m_i - V)_0, \quad (2)$$

where $V = 5\overset{m}{.}13$ is the observed magnitude of Θ^1 Ori C [9], and the other two terms are the observed and unreddened color indices (see Table 1). The normal normalized interstellar reddening law $\mathrm{A}(\lambda)$ was taken from [11].

Figure 1 shows a dependence of the form (1). The straight line is a least-squares fit. As a result, we obtained

$$x = 1.07(2), \quad A_V = 1\overset{m}{.}05(2), \quad V_0 = 4\overset{m}{.}03(2). \quad (3)$$

The error, in units of the last digit, is given in parentheses. Our value of A_V is in good agreement with the visual absorption obtained by Walborn [6] under the assumption of $R = 3$. However, A_V turns out to be considerably larger than that for the stars BM Ori [14] and V1016 Ori [15]: $A_V = 0\overset{m}{.}70(5)$ and $0\overset{m}{.}85(5)$, respectively. This difference can be attributed to the fact that, apart from the interstellar absorption, additional absorption arises in the cloud surrounding the star. Another reason is that the other radiation sources cannot be ignored. Below, we refine the visual absorption.

Table 1. Input data for constructing the continuum spectrum and the system's radiation budget

Band	λ, μm	m_i–V	m_i–V	$(m_i$–$V)_0$	O7	Ob2	Ob3	O–C
U	0.36	$-0\overset{m}{.}95$		$-1\overset{m}{.}44$	0.98	0.00	0.00	$0\overset{m}{.}02$
B	0.44	0.00		−0.32	1.01	0.01	0.00	−0.02
V	0.55	0.00		0.00	1.00	0.04	0.00	−0.04
R	0.70	−0.22		0.15	0.89	0.10	0.00	0.00
I	0.88	−0.40		0.46	0.75	0.20	0.00	0.05
J	1.25	−0.55		0.77	0.54	0.32	0.00	0.14
H	1.62	−0.64		0.85:	0.54	0.53	0.00	−0.06
K	2.2	−0.77	$-0\overset{m}{.}6$	0.93	0.47	0.66	0.00	−0.13
L	3.4	−0.98	−0.9	1.00	0.38	0.61	0.00	0.01
M	4.7		−1.0	1.16:	0.32	0.67	0.03	−0.02
N'	8.6		−4.5	1.18:	0.01	0.03	1.07	−0.11
N''	10.7		−6.5	1.15:	0.00	0.01	0.79	0.21
P	12.2		−6.5	1.29:	0.00	0.00	1.44	−0.45
Q	18		−9.0	1.21:	0.00	0.00	0.79	0.31

Let us consider the continuum spectrum of the star. Figure 2 shows the observed absolute flux from Θ^1 Ori C (asterisks) for 14 bands. This flux was computed by using the calibration coefficients from [9, 10].

The dashed line in this figure indicates the energy distribution for an unreddened O7 star. Some of the color indices were taken from [11]. We computed the infrared colors absent in [11] by using a blackbody model with effective temperature $T_1 = 37\,000(2000)$ K. In what follows, the errors are given in parentheses, in units of the last digit. These errors are not exact values, but the estimates obtained by trial and error. In Table 1, the color indices computed by using the blackbody model are marked with a colon. The $H - V$ color for an unreddened star was estimated by interpolation; it is also marked with a colon in Table 1.

An examination of Fig. 2 leads us to the following conclusions.

For the *UBVR* bands, there is good agreement between the observed energy distribution and the energy distribution for a normal reddened O7 star with $A_V = 0\overset{m}{.}95(5)$. This allowed us to use the magnitudes in these bands to roughly estimate the interstellar reddening.

From the I ($\lambda = 0.88$ μm) band to the M ($\lambda = 4.7$ μm) band inclusive, the observed flux is higher than that for a reddened O7 star. This difference can be eliminated by adding blackbody radiation with temperature $T_2 = 4000(500)$ K and blackbody radius $R_2 = 16.2(5)\,R_\odot$. The nature of this radiation is unclear; however, if the star is assumed to be binary, then the radiation with $T_2 = 4000$ K belongs to a companion of spectral type K7. Below, we consider the nature of this hypothetical companion.

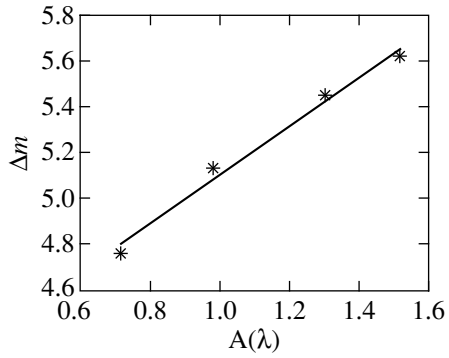

Fig. 1. Visual absorption for a normal law A(λ) versus *UBVR* magnitudes for Θ^1 Ori C.

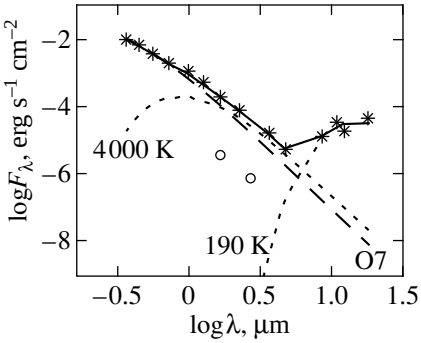

Fig. 2. The observed energy distribution for Θ^1 Ori C (asterisks); the energy distribution for an unreddened O7 star (object 1, dashed line); a blackbody energy distribution for temperature T_2 = 4000 K, presumably a K7 companion (object 2, dotted line); blackbody radiation with temperature T_3 = 190 K, presumably a cocoon star or a dust envelope (object 3, dotted line); and the total radiation of the O7 star, the K7 companion, and the dust envelope (solid line). The flux from Θ^1 Ori F is indicated by circles.

As we see from Fig. 2, the flux in the last four bands (λλ 8.6–18 μm) abruptly increases compared to that for a reddened O7 star. In order to explain this effect, we must assume the existence of a third radiation source with temperature T_3 = 190(10) K and radius R_3 = 10700(500) $R_\odot$. Such a phenomenon was detected in Θ^2 Ori A by Ney *et al.* [10]. There is a close match between the source temperatures, T = 200 K, in [10]. These authors provide no error.

Our analysis of the energy distribution shows that the spectrum can be satisfactorily described by a three-component model. A normal O7 star (object 1), a blackbody source with a temperature of 4000 K (object 2), and a blackbody source with a temperature of 190 K (object 3) emit radiation.

The last four columns in Table 1 give, respectively, ratios of the flux from a reddened O7 star to the observed flux, the same ratios for objects 2 and 3 (columns Ob2 and Ob3), and *O–C* residuals in the form of differences between the observed flux and the sum of fluxes from the O7 star and objects 2 and 3. The residuals are in magnitudes.

An analysis of these data and Fig. 2 leads us to the following conclusions.

From *U* to *H*, the O7 star makes the largest contribution to the total flux. From *H* to *M*, object 2 is brightest. Secondary lines should therefore be sought in the wavelength range 1.6–4.7 μm. Starting from the *N*' band, the system's emission is produced almost entirely by object 3. This object should be sought at wavelengths λ > 8.6 μm.

Let us consider the properties of each of the three objects. We assume that they all form a single, dynamically bound system. Alternative approaches can involve: (1) a chance projection of the objects and (2) a nonstellar nature of the objects. For example, object 3 can be a circumstellar dust envelope [10]. Analysis of alternatives is beyond the scope of this paper.

PRIMARY STAR

Let us determine the absolute magnitude of the primary star by using the formula

$$M_{\rm bol} = V_0 - (m - M) + {\rm BC} = -7\overset{m}{.}7(1). \qquad (4)$$

Here, $V_0 = 4\overset{m}{.}20(5)$ is the dereddened magnitude of the primary, $(m - M) = 8\overset{m}{.}22(5)$ is the distance modulus for the star, and BC = $3\overset{m}{.}65$ is the bolometric correction [16]. According to Straizis and Kuriliene [16], the absolute magnitude for a normal star is $-7\overset{m}{.}5(2)$, in good agreement with our estimate for the primary.

Given this estimate, the bolometric luminosity is $L_1 = 9.3 \times 10^4$ solar luminosities.

According to the tables from [16], the effective temperature for a normal O7 star is T_1 = 37 000 K. The stellar radius can then be estimated by using the formula

$$M_{\rm bol} = 42.36 - 10\log T_1 - 5\log R_1. \qquad (5)$$

Hence, we obtain $R_1 = 7.4(7)\ R_\odot$. The radius for a normal O7 star must be 6.6 $R_\odot$ [16], in satisfactory agreement with our estimate.

We drew the following general conclusion from our analysis of the properties of the primary star: it is a normal ZAMS star.

Figure 3 shows the Hertzsprung–Russell diagram, in which all the components of the system under consideration are plotted. We see from this figure that the primary lies exactly on the ZAMS and that its mass is considerably larger than 15 $M_\odot$. We estimated the primary's mass by extrapolation to be 20(2) $M_\odot$.

Can the hypothesis of axial rotation of a star with a spot on its surface account for the star's spectral variability with a period of 15 days? If $R_1 = 7.4\ R_\odot$ and the period is 15.41 days, then the equatorial rotational veloc-

ity of the star must be of the order of $V_e = 24$ km s^{-1}. The projected rotational velocity is $V_e \sin i = 50$ km s^{-1} [7], so the spectral variability cannot be explained in terms of the spot theory. A further discussion of this fundamental issue requires refining the rotational velocity and estimating its errors.

THE NATURE OF OBJECT 2

Consider two assumptions about the nature of the emitting body with temperature 4000 K.

First, this may be a companion of the O7 star. If its orbital plane lies near the plane of the sky, then no radial-velocity variations will be observed, nor will any eclipse occur. The excessively large radius can be explained by the fact that this is a contracting protostar.

Second, the star Θ^1 Ori F lying at a distance of $4''.0$ from Θ^1 Ori C [17] falls within the photometer aperture. Magnitude measurements for star F are given in [12]: $H = 9^m.05$ and $K = 8^m.99$. We converted these magnitudes to fluxes. These fluxes are indicated in Fig. 2 by circles. We see from the figure that the light source with temperature 4000 K cannot be Θ^1 Ori F, because the *HK* flux from this source is almost two orders of magnitude larger than that from star F.

So, object 2 is probably a companion of the primary O7 star. If this companion were a normal star, then the spectral type K7 would correspond to its temperature [16]. The assumption that Θ^1 Ori C has an unseen companion of spectral type K0 was previously invoked to account for the anomalous interstellar reddening law [13]. Stebbins and Whitford [13] concluded that the reddening law was normal, while the color anomalies were coupled with the existence of a K0 companion.

Let us estimate the bolometric luminosity of the companion in solar luminosities by using the formula

$$L_2/L_\odot = 4\pi R_2^2 \sigma T_2^4 / L_\odot = 8.5 \times 10^3. \quad (6)$$

In the Hertzsprung–Russell diagram (see Fig. 3), object 2 lies on the birthline for 15 $M_\odot$ stars. The following question remains open. The star may be on the Hayashi track and may continue to move downward. In this case, its mass is less than 15 $M_\odot$. An alternative possibility is that the star turns to the horizontal segment of the track. In that case, its mass is 15 $M_\odot$. These two cases are impossible to distinguish; we assume the second alternative.

Let us use the track for a 15 $M_\odot$ star and estimate the radius of the protostar at the right end of the track from the relation

$$L_2/L = (R_2/R)^2 (T_2/T)^4. \quad (7)$$

Here, the subscript 2 and no subscript refer to the star near the right and left ends of the track, respectively. From the tables in [16], we find for ZAMS stars that $L = 3.2 \times 10^3\ L_\odot$, $R = 3.5\ R_\odot$, and $T = 22\,400$ K. Taking the previously determined L_2 and T_2, we obtain $R_2 = 32\ R_\odot$, a value that is twice that determined by analyzing the continuous radiation. However, if the error in T_2 is taken into account, then the agreement can, nevertheless, be considered satisfactory. This discrepancy can be eliminated by assuming that the stellar mass is less than 15 $M_\odot$.

Let us estimate the minimum separation between object 2 and the primary star under the following assumptions: object 2 has no intrinsic energy sources, and it is heated by the primary star. In this case, the separation between object 2 and the primary cannot be smaller than r_2, which is given by the relations [18]

$$T_2 = T_1 W^{1/4}, \quad W = R_1^2/4r_2^2, \quad (8)$$

where $T_2 = 4000$ K and $T_1 = 37\,000$ K are the temperatures of object 2 and the primary star, respectively; W is the dilution factor; and $R_1 = 7.4\ R_\odot$ is the primary's radius. Equations (8) yield $r_2 = 300\ R_\odot = 1.5$ AU.

An upper limit on the separation between the primary and object 2 can be estimated by using speckle interferometry [17]. As follows from [17], object 2 was not detected. The angular resolution was $0''.035$, which corresponds to 15 AU at a distance of 440 pc. However, a different explanation for the negative result is also possible: the magnitude difference in V is $\sim 2^m.5$, which is close to the detection limit (3^m).

Recently, a new attempt has been made to detect companions in the Orion Trapezium stars by speckle interferometry [19]. A companion was discovered in Θ^1 Ori C at a distance of $0''.033$. Its temperature calculated from the *H–K* color lies in the range 3550–7000 K, in agreement with our estimate. Weigelt *et al.* [19] provide *HK* magnitudes for the companion. If these magnitudes are converted to fluxes, then they are in good agreement with the fluxes from object 2 (see Fig. 2).

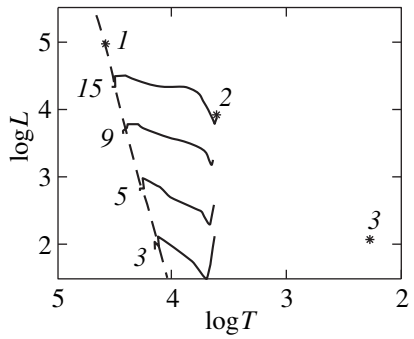

Fig. 3. Hertzsprung–Russell diagram. The logarithm of effective temperature (in K) is along the *x* axis, and the bolometric luminosity (in solar units) is along the *y* axis. The dashed line represents the ZAMS, as constructed by Straizis and Kuriliene [16]. The numbers near the left end of the evolutionary tracks [23] indicate stellar masses (in solar masses). The star positions are: *1*—primary; *2*—object 2, and *3*—object 3.

Table 2. Model parameters for the system Θ^1 Ori C

Parameter	O7	Ob2	Ob3
Mass, $M_\odot$	20(2)	15(2)	
Radius, $R_\odot$	7.4(7)	16.2(5)	10700(500)
Temperature, K	37000(2000)	4000(500)	190(10)
M_{bol}	$-7^m.7(1)$	$-5^m.1(2)$	$-0^m.6(2)$
Separation, AU		>1.5	>660
Wavelength range of search, μm	<1.6	1.6–4.7	>8.6

There is every reason to conclude that object 2 is identical to the star detected by speckle interferometry.

Using Kepler's third law and neglecting the mass of object 2, we obtain the minimum revolution period

$$P_2 = (M_1 r_2^3)^{1/2} = 8 \text{ years}. \quad (9)$$

This result shows that the 15-day period found in the star by its spectral variability cannot be associated with the revolution of object 2 around the primary.

It follows from the estimated minimum separation and minimum period that the orbital velocity of object 2 cannot exceed 5 km s^{-1}, while for the primary star this velocity cannot exceed 4 km s^{-1}. Since these values are of the order of the measurement errors in the radial velocity, it comes as no surprise that the radial velocity is believed to be constant.

THE NATURE OF OBJECT 3

Object 3 lies well to the right of the birthline for stars in the Hertzsprung–Russell diagram (see Fig. 3), so it can be neither a star nor a protostar in the contraction stage. The object's radius is $R_3 = 10700\ R_\odot = 50$ AU. The minimum globule radius is ~10000 AU [18]; i.e., object 3 cannot be a globule. In all probability, the prototype of object 3 should be sought among cocoon stars [20], while the related objects could be proplyds and silhouettes [21].

We estimated the minimum separation r_3 between object 3 and the primary star using formula (8) to be $r_3 = 1.4 \times 10^5\ R_\odot = 660$ AU = $1''.5$. If the object lies near the plane that is perpendicular to the line of sight and that passes through the primary, then it could have been seen at 10 μm. Unfortunately, no map of the Orion Trapezium has been constructed at this wavelength.

As was already pointed out above, the excess emission at 10 μm is also observed in Θ^2 Ori A [9]. Lee [9] believes this emission to be produced by the dust envelope formed by stellar radiation pressure and stellar wind on the interstellar dust. The choice between the models (a cocoon, a proplyd, or an envelope) can be made by constructing a map of the Θ^1 Ori C and Θ^2 Ori A field at ~10 μm.

CONCLUSION

Having analyzed the continuum spectrum of Θ^1 Ori C, we propose a three-component model. Parameters of this model are given in Table 2.

In this table, columns O7, Ob2, and Ob3 refer to the primary star, object 2, and object 3, respectively. The next-to-last row gives minimum separations between the objects and the primary, and the last column gives the spectral range in which the flux from one object exceeds the fluxes from the other objects. These data are useful in searching for objects 2 and 3. Object 2 can be found by using a spectrum in the above range, while object 3 can be found by using a map of the Θ^1 Ori C field constructed in a photometric band with an effective wavelength $\lambda > 8.6$ μm.

The main problems to be solved are as follows.

The most important problem is to study the star's radial velocity. It is argued in the literature that this velocity is both constant [3] and variable with an amplitude of no less than 16 km s^{-1}; however, the period, if it exists, proved to be considerably longer than the period of spectral variability [4]. The most accurate determination of the period of spectral variations yields $P = 15.422 \pm 0.002$ days, while the period of radial-velocity variations is more than 40 days [4]. The problem can be solved by a long-term monitoring of the star, by obtaining high-quality spectra, and by measuring radial-velocity variations with an accuracy of ~1 km s^{-1}.

A two-dimensional classification of the star should be made to accurately determine T_{eff} and $\log g$. This makes it possible to estimate the mass and radius of both the primary star and the potential companion with a smaller error.

We did not determine the chemical composition of the star. However, this is of crucial importance because unexpected results can be obtained. For example, it is well known that there are no Si IV lines in the spectrum which must be strong in an O7 star [22].

ACKNOWLEDGMENTS

I wish to thank V.G. Klochkova, O.B. Kostina, V.P. Fedotov, and Yu.M. Chesnokov for useful discussions.

REFERENCES

1. P. O. Vandervoort, Astrophys. J. **139**, 869 (1964).
2. E. A. Vitrichenko, Pis'ma Astron. Zh. **22**, 587 (1996).
3. P. S. Conti, Astrophys. J. Lett. **174**, L79 (1972).
4. O. Stahl, B. Wolf, Th. Gang, *et al.*, Astron. Astrophys. **274**, L29 (1993).
5. N. R. Walborn and J. S. Nichols, Astrophys. J. Lett. **425**, L29 (1994).
6. N. R. Walborn, Astrophys. J. Lett. **243**, L37 (1981).
7. M. Gagné, J.- P. Cailault, J. R. Stauffer, and J. L. Linski, Astrophys. J. Lett. **478**, L87 (1997).

8. J. Babel and Th. Montmerle, Astrophys. J. Lett. **485**, L29 (1997).
9. T. A. Lee, Astrophys. J. **152**, 913 (1968).
10. E. P. Ney, D. W. Strecker, and R. D. Gehrz, Astrophys. J. **180**, 809 (1973).
11. V. Straizis, *Multicolor Stellar Photometry* (Mokslas, Vilnius, 1977).
12. M. G. Petr, V. C. Foresto, S. V. W. Beckwith, *et al.*, Preprint Max Planck Inst., No. 1998-5 (1998).
13. J. Stebbins and A. E. Whitford, Astrophys. J. **102**, 318 (1945).
14. E. A. Vitrichenko and V. M. Larionov, Pis'ma Astron. Zh. **22**, 178 (1996).
15. E. A. Vitrichenko, Pis'ma Astron. Zh. **25**, 220 (1999).
16. V. Straizis and G. Kuriliene, Astrophys. Space Sci. **80**, 353 (1981).
17. B. D. Mason, D. R. Gies, W. I. Hartkopf, *et al.*, Astron. J. **115**, 821 (1998).
18. D. Ya. Martynov, *A Course in General Astrophysics* (Nauka, Moscow, 1988).
19. G. Weigelt, J. Balega, T. Preibisch, *et al.*, Preprint Max Planck Inst., No. 799 (1999).
20. V. G. Surdin, *The Birth of Stars* (URSS, Moscow, 1997).
21. C. R. O'Dell and Z. Wen, Astrophys. J. **436**, 194 (1994).
22. P. S. Conti, Astrophys. J. **179**, 181 (1973).
23. I. Iben, Astrophys. J. **141**, 993 (1965).

Translated by V. Astakhov

Astronomy Letters, Vol. 26, No. 4, 2000, pp. 250–260. Translated from Pis'ma v Astronomicheskiĭ Zhurnal, Vol. 26, No. 4, 2000, pp. 301–312.

Dynamical Stability of Triple Stars

V. V. Orlov and A. V. Petrova

Astronomical Institute, St. Petersburg State University, Bibliotechnaya pl. 2, Petrodvorets, 198904 Russia

Received April 5, 1999

Abstract—The dynamical stability of 38 observed hierarchical triple stars with known orbital elements of the internal and external binary subsystems and component masses is considered. Four different criteria of dynamical stability are used. The observed stability parameters and their critical values are calculated by taking into account errors in the orbital elements and component masses. Most triple systems are stable. According to some criteria, several triple stars (ADS 440, ξ Tau, λ Tau, ADS 3358, VV Ori, ADS 10157, HZ Her, Gliese 795, ADS 15971, and ADS 16138) may be dynamically unstable. This result is probably associated with unreliability of the empirical stability criteria and/or with errors in the observed quantities. © *2000 MAIK "Nauka/Interperiodica".*

1. INTRODUCTION

The observed triple stars can be subdivided into two groups: nonhierarchical and hierarchical systems. The first population consists of young, dynamically unstable systems whose dynamical evolution leads to the formation of a close binary as the third component goes away. Since the stars have finite radii, two or even all three components can merge in principle. The hierarchical triple stars can be both stable and unstable, depending on the component mass ratio and on the orbital elements of the internal and external binary subsystems.

Szebehely and Zare [1], Fekel [2], and Donnison and Mikulskis [3] considered the problem of stability for samples of observed hierarchical triple stars.

Szebehely and Zare [1] considered dynamical stability for eight triple stars and showed all these systems to be stable, provided that the motions in them were plane and direct ones (the orbits of both binary subsystems lay in a single plane and the rotation in them occurred in the same sense). Five of the systems considered may be dynamically unstable if the orbital planes are inclined at a nonzero angle.

Fekel [2] (1981) analyzed a sample of 27 triple stars. He showed that 23 systems were dynamically stable, whereas the four remaining ones could be dynamically unstable in the case of retrograde motions of the internal and external binaries.

Donnison and Mikulskis [3] analyzed a more representative sample of 38 triple stars and showed all these systems to be dynamically stable, irrespective of the mutual orbital inclination.

At the same time, the stability of some hierarchical triple stars is still an open question. This is because, on the one hand, the observational data are unreliable, and, on the other hand, there is no universal criterion of dynamical stability for triple systems (see Sect. 3).

In this study, we draw up a list of triple stars with known component masses and orbital elements (periods, eccentricities, and inclinations) of the internal and external binaries. All data were taken from original studies. Some of the references were taken from [2, 4, 5]. We found a total of 38 such triple systems. The systems are listed in Sect. 2, in which we also discuss the reliability of the measured parameters and their errors. In Sect. 3, we describe the stability criteria used. In Sect. 4, we present the results of applying our criteria of dynamical stability to the chosen triple stars. We specially discuss those systems for which some criteria point to instability. We discuss the results obtained in Sect. 5.

2. LIST OF TRIPLE STARS

We found a total of 38 hierarchical triple stars in the literature with measured component masses (M_1, M_2, M_3), periods (P_{in} and P_{ex}), eccentricities (e_{in} and e_{ex}), and inclinations (i_{in} and i_{ex}) of the internal and external binaries. In what follows, $M_1 \geq M_2$ are the masses of the components of the internal pair, and M_3 is the mass of the distant body. However, the original papers do not provide errors for all parameters of the triple stars, by any means. At the same time, the reliability of the estimated parameters of dynamical stability (see Sect. 3) depends on errors in the initial parameters, which are inferred from observational data.

To order to make judgements on the errors in our results, we made some assumptions about unknown errors in the initial quantities. The following errors were assumed for the periods P_{in} and P_{ex}:

(1) $\sigma_P = 0$ if $P < 100^d$;

(2) $\sigma_P = 0.1P$ if $100^d < P < 100^a$.

(3) $\sigma_P = 0.3P$ if $P > 100^a$.

The errors in the masses, orbital inclinations, position angles of the lines of nodes, and eccentricities were

1063-7737/00/2604-0250$20.00 © 2000 MAIK "Nauka/Interperiodica"

assumed to be $\sigma_M = 0.1\ M$, $\sigma_i = 10°$, $\sigma_\Omega = 10°$, and $\sigma_e = 0.1$, respectively.

Table 1 gives the system names, their indices $(\alpha, \delta)_{1900}$, orbital elements P_{in}, e_{in}, i_{in}, Ω_{in}, P_{ex}, e_{ex}, i_{ex}, Ω_{ex} (here, Ω_{in} and Ω_{ex} are the position angles of the lines of nodes connecting the intersections of the orbital planes of the internal and external binaries with the plane of the sky), and component masses M_1, M_2, M_3 together with their errors. The systems in Table 1 are listed in order of increasing right ascension.

If several studies were available in which particular parameters of the triple systems were determined, we chose the most recent study. All quantities in Table 1 were taken from the original papers cited in the last column. We did not make independent estimates of any quantities in Table 1.

For the mutual orbital inclination i of the internal and external binaries to be estimated by using the well-known formula [6]

$$\cos i = \cos i_{in}\cos i_{ex} + \sin i_{in}\sin i_{ex}\cos(\Omega_{ex} - \Omega_{in}), \quad (1)$$

the angles Ω_{in} and Ω_{ex} must be known. However, no data on Ω_{in} and/or Ω_{ex} are available for most of the triple systems considered. Only for seven systems do we know both angles (occasionally, to within 180°); these systems are marked by asterisks in Table 1. For each of the stability criteria considered (see Sect. 3), we used the value of all the possible mutual inclinations i that yielded the smallest stability margin. Even under these conditions, most systems are stable according to all criteria. We discuss each instability case separately.

Among the triple systems considered, the components of maximum, intermediate, and minimum mass prove to be distant components with an approximately equal probability. Systems with close internal pairs dominate: $P_{in} < 10^d$ in 23 systems (about 60% of the cases). As a rule, triple systems have a high degree of hierarchy: $X = P_{ex}/P_{in} > 100$ in 23 systems (about 60% of the cases). However, some triple systems exhibit a moderately high degree of hierarchy: $X < 10$ in two systems, λ Tau ($X = 8.4$) and ADS 10157 ($X = 3.3$). The orbits of the internal binaries are, as a rule, nearly circular: $e_{in} < 0.1$ in 22 systems (about 60% of the cases). At the same time, the external binaries usually have appreciable eccentricities: $e_{ex} \geq 0.3$ in 25 systems (about 2/3 of all the cases considered). Even highly eccentric orbits with $e_{ex} \geq 0.8$ are encountered (ADS 999, 14839, and 14893).

Note that the systems considered may include systems of a larger multiplicity (for example, IU Aur may be a quadruple system). This fact should be borne in mind when interpreting the results from Sect. 4.

3. CRITERIA OF DYNAMICAL STABILITY FOR TRIPLE STARS

The following two scenarios for the disturbance of dynamical stability are possible in hierarchical triple systems:

(1) replacement of one of the components of a close pair by the distant component (the violation of hierarchy);

(2) escape of the distant component from the system in a hyperbolic orbit without the preceding violation of hierarchy.

We know several criteria for the stability of triple systems of point masses against the violation of hierarchy (see, e.g., [3, 7–10] and references therein). In principle, the distant component can always escape without the violation of hierarchy [1]. However, numerical simulations show (see, e.g., [9]) that this possibility is not realized for triple systems with a high degree of hierarchy during at least 10 000 revolutions of the external binary.

Here, we consider those criteria of dynamical stability for triple systems for which we derived an analytic expression or propose an analytic fit to the results of numerical simulations for triple systems with arbitrary initial conditions.

Golubev [11, 12] suggested the first criterion. Subsequently, the same condition was independently derived by other authors (see, e.g., references in [1]). The stability parameter in Golubev's criterion has the form

$$s = -\frac{c^2 H}{G^2 \overline{M}^5}, \quad (2)$$

where c and H are the angular momentum and total energy of the triple system, respectively; G is the gravitational constant; and $\overline{M}$ is the mean mass of the bodies in the triple system.

If s is larger than some critical value s_c, then the hierarchy in the triple system is maintained indefinitely. Otherwise, the triple system can violate its hierarchical structure. In contrast to the other stability criteria considered, Golubev's criterion was derived analytically and ensures that the hierarchy is preserved in the triple system. At the same time, if s does not exceed the critical value s_c, then the hierarchy is not necessarily violated. Kiseleva *et al.* [10] pointed out that there is a domain of initial conditions in which Golubev's criterion is not satisfied, while the triple system does not violate its hierarchy during at least 10 000 revolutions of the outer binary subsystem. Golubev's criterion says nothing about the stability of a triple system against escape of the distant component without the violation of hierarchy.

The critical value s_c depends only on the body masses. According to [1],

Table 1. Orbital elements and component masses of the triple systems

No.	Name Index	P^{d}_{in}, $\sigma_{P_{in}}$ P^{a}_{ex}, $\sigma_{P_{ex}}$	e_{in}, $\sigma_{e_{in}}$ e_{ex}, $\sigma_{e_{ex}}$	i_{in}, $\sigma_{i_{in}}$ i_{ex}, $\sigma_{i_{ex}}$	Ω_{in}, $\sigma_{\Omega_{in}}$ Ω_{ex}, $\sigma_{\Omega_{ex}}$	M_1, σ_{M_1} M_2, σ_{M_2}	M_3, σ_{M_3} $M_\odot$	References
1*	ADS 440	5826.0	0.05	45.0	167.0	0.40	0.12	[26]
	00263+6642	±80.0	±0.07	–	–	±0.02	±0.02	
		320.0	0.0	51.0	168.0	0.13		
		–	–	–	–	±0.01		
2	ADS 999	5.3337	0.155	90.0	–	1.17	1.4	[27, 28]
	01084+6025	0.0000	0.003	–	–	–	–	
		75.0	0.88	129.0	77.4	1.11		
		–	–	–	–	–		
3*	Gliese 60	1665.0	0.316	25.25	68.1	0.88	0.54	[1, 29, 30]
	01304–3026	–	–	–	–	–	–	
		111.8	0.21	29.3	141.8	0.87		
		–	–	–	–	–		
4	ADS 1833	1.58	0.00	85.0	–	4.0	4.0	[2, 31, 32]
	02182+6106	–	–	3.0	–	–	–	
		581.861	0.613	47.25	141.15	4.0		
		–	–	–	–	–		
5	β Per	2.8673	0.0217	81.4	–	3.70	1.42	[33–35]
	03017+4034	–	0.0025	0.2	–	0.30	0.13	
		1.86	0.22	83.0	311.0	0.81		
		–	0.02	2.0	–	0.05		
6	ξ Tau	7.15	0.00	57.0	–	3.2	5.5	[2, 20]
	03254+1236	–	–	5.0	–	–	–	
		0.397	0.40	48.0	–	3.1		
		–	–	4.0	–	–		
7	ADS 2644	2.8377	0.0	33.0	–	1.4	0.53	[36, 37]
	03317+0015	0.0000	–	2.0	–	0.2	–	
		21.01	0.18	32.07	92.35	1.1		
		–	–	–	–	0.2		
8	λ Tau	3.9530	0.0	76.0	–	7.18	0.7	[38]
	03551+1212	–	–	–	–	0.09	0.2	
		0.09054	0.15	69.0	–	1.89		
		0.00014	0.06	–	–	0.04		
9	b Per	1.5274	0.023	55	–	2.25	1.3	[39]
	04107+5003	0.0000	0.014	3	–	–	–	
		1.9214	0.235	65	–	0.50		
		0.0012	0.058	5	–	0.02		
10*	ADS 3358	9735.0	0.86	141.0	20.8	2.4	3.2	[21]
	04320+5317	–	–	–	–	–	–	
		430	0.32	133.0	112.5	1.4		
		–	–	–	–	–		
11	IU Aur	1.8115	0.00	88.20	–	15.9	12	[40, 41]
	05212+3442	–	–	0.10	–	0.7	–	
		0.809	0.40	80	–	10.8		
		–	–	–	–	0.7		
12	VV Ori	1.485	0.00	85.6	–	10.2	2.3	[42, 43]
	05285–0114	–	–	–	–	–	–	
		0.33	0.29	90	–	4.5		
		–	–	–	–	–		
13	64 Ori	14.5722	0.387	24	–	4.0	6.0	[2, 44]
	05575+1942	0.0001	0.004	4	–	–	–	
		13.03	0.734	50	244	3.5		
		0.05	0.009	–	–	–		

Table 1. (Contd.)

No.	Name Index	P^{d}_{in}, $\sigma_{P_{in}}$ P^{a}_{ex}, $\sigma_{P_{ex}}$	e_{in}, $\sigma_{e_{in}}$ e_{ex}, $\sigma_{e_{ex}}$	i_{in}, $\sigma_{i_{in}}$ i_{ex}, $\sigma_{i_{ex}}$	Ω_{in}, $\sigma_{\Omega_{in}}$ Ω_{ex}, $\sigma_{\Omega_{ex}}$	M_1, σ_{M_1} M_2, σ_{M_2}	M_3, σ_{M_3} $M_\odot$	References
14	HD 76360	9.07	0.50	33	–	1.8	1.9	[2, 45, 46]
	08505–4708	–	–	3	–	–	–	
		7.24	0.20	33.2	–	1.6		
		–	–	–	–	–		
15	pVel	10.2104	0.5077	149	–	2.13	2.41	[2, 47, 48]
	10331–4742	0.0000	0.0119	4	–	–	–	
		16.30	0.73	129.4	38.3	1.81		
		–	–	–	–	–		
16	55 Uma	2.5538	0.329	38	–	2.26	1.7	[49, 50]
	11137+3844	0.0000	0.013	7	–	0.23	1.1	
		5.12	0.123	64.4	129.5	2.0		
		–	–	–	–	0.3		
17	ADS 8189	7.3990	0.377	69	–	1.6	1.3	[2, 51, 52]
	11254+4150	0.0001	0.010	3	–	–	–	
		86.44	0.37	56.7	337.1	1.5		
		–	–	–	–	–		
18	η Vir	71.7919	0.272	47	–	2.34	1.61	[53]
	12148–0007	0.0009	0.009	2	–	0.20	0.10	
		13.12	0.079	51.1	173.0	1.95		
		0.05	0.014	0.2	2.4	0.20		
19	CQ Dra	0.1656	0.00	50	–	0.58	5.0	[54]
	12257+6945	0.0014	–	–	–	–	–	
		4.663	0.30	50	–	0.27		
		0.008	0.05	–	–	–		
20	ADS 9019	0.4077	0.00	90.0	–	1.0	1.0	[55–57]
	13141+0537	0.0000	–	1.5	–	–	–	
		282.5	0.63	43.7	168.8	1.0		
		–	–	–	–	–		
21	DL Vir	1.3155	0.0	68	–	2.4	2.0	[2, 58]
	13472–1813	–	–	–	–	–	–	
		6.247	0.44	84	–	1.1		
		0.036	0.03	–	–	–		
22	HD 129132	101.606	0.117	45	–	1.97	1.82	[59]
	14358+2214	0.003	0.007	–	–	–		
		9.268	0.073	104.6	78.2	1.29		
		0.019	0.010	0.5	0.7	–		
23	ADS 9494	0.2678	0.0	70.92	–	0.98	1.06	[60–64]
	15005+4803	0.0000	–	0.20	–	–	–	
		225.0	0.43	83.9	57.8	0.55		
		–	–	–	–	–		
24*	ADS 10157	3840	0.07	90	23	1.05	0.73	[22]
	16375+3147	–	–	–	–	–	–	
		34.487	0.460	132.9	49.2	0.19		
		–	–	–	–	–		
25	HZ Her	1.7002	0.01	87	–	2.18	0.3	[25, 65, 66]
	16542+3530	–	–	3	–	0.11	0.2	
		0.096	0.5	–73	–	1.30		
		–	0.1	–	–	0.14		
26	V819 Her	2.2296	0.0	137	–	1.86	1.11	[67]
	17184+4004	0.0000	–	56	–	0.09	0.02	
		5.5273	0.672	56.2	323.7	1.53		
		0.0019	0.002	0.4	0.3	0.08		

Table 1. (Contd.)

No.	Name Index	P^{d}_{in}, $\sigma_{P_{in}}$ P^{a}_{ex}, $\sigma_{P_{ex}}$	e_{in}, $\sigma_{e_{in}}$ e_{ex}, $\sigma_{e_{ex}}$	i_{in}, $\sigma_{i_{in}}$ i_{ex}, $\sigma_{i_{ex}}$	Ω_{in}, $\sigma_{\Omega_{in}}$ Ω_{ex}, $\sigma_{\Omega_{ex}}$	M_1, σ_{M_1} M_2, σ_{M_2}	M_3, σ_{M_3} $M_\odot$	References
27	HD 157978/9	3.76	0.00	65	–	2.8	3.7	[2, 45]
	17215+0741	–	–	4	–	–	–	
		3.29	0.39	79	–	2.8		
		–	–	7	–	–		
28	Kuiper 84	34.5031	0.386	66	–	0.55	0.65	[68]
	17535+0428	0.0100	0.016	–	–	0.03	0.32	
		14.508	0.549	69.2	173.7	0.46		
		0.069	0.031	4.1	2.1	0.03		
29	TY CrA	2.8887	0.0216	90	–	2.98	1.26	[69]
	18549–3702	0.0000	0.0055	–	–	0.12	0.29	
		0.7392	0.507	20	–	1.57		
		0.0019	0.043	1.5	–	0.04		
30	ADS 12214	10.7786	0.47	71	–	2.3	2.9	[2, 70, 71]
	19094–2526	–	–	5	–	–	–	
		18.75	0.468	85	291.9	1.7		
		–	–	–	–	–		
31	Gliese 795	920.2	0.747	18	–	0.67	0.51	[27, 72]
	20346+0437	1.7	0.017	2	–	–	–	
		39.40	0.12	85.4	128.3	0.44		
		–	–	–	–	–		
32	Gliese 815	3.2762	0.007	42	–	0.42	0.30	[73, 74]
	20562+3941	0.0000	0.007	–	–	–	–	
		27	0.50	48.1	97.0	0.27		
		–	–	–	–	–		
33	ADS 14839	3.9660	0.0033	50.72	–	1.138	0.974	[75]
	21138+1109	0.0000	0.0008	0.46	–	0.021	0.021	
		78.54	0.8651	100.36	255.03	1.078		
		0.47	0.0008	0.16	0.17	0.020		
34	ADS 14893	2.2361	0.0635	104	–	0.83	0.81	[2, 76, 77]
	21165+0955	0.0000	0.0055	4	–	–	0.23	
		6.107	0.870	132.26	300.58	0.66		
		0.050	0.050	30.00	15.00	–		
35*	ADS 15600	823	0.589	79.9	93.5	2.05	1.462	[78–80]
	22009+6408	2	0.010	–	1.0	0.64	–	
		3822.6	0.24	109.01	85.0	0.74		
		–	–	–	–	0.23		
36*	ADS 15971	9390	0.59	34.3	202.7	1.5	1.5	[81]
	22237–0032	37	0.10	–	–	–	–	
		760	0.50	135.87	304.64	0.4		
		–	0.10	–	–	0.1		
37*	ADS 16138	551.6	0.05	90	150	1.00	1.18	[27, 82]
	22344+4347	0.84	0.02	–	–	0.16	0.18	
		30	0.30	85	153.3	0.72		
		–	–	–	–	0.08		
38	ADS 16591	109.74	0.33	27	–	1.02	0.96	[27, 83]
	23075+0209	0.03	0.02	–	–	–	0.16	
		29.5	0.31	109	112	0.51		
		–	–	3.5	2	–		

$$s_c = \frac{f^2(\rho)g(\rho)}{6\overline{M}^6}, \quad (3)$$

where ρ is the only positive root of the fifth-degree equation

$$(1+\alpha_1)\rho^5 + (3+2\alpha_1)\rho^4 + (3+\alpha_1)\rho^3 - (\alpha_1+3\alpha_2)\rho^2 - (2\alpha_1+3\alpha_2)\rho - (\alpha_1+\alpha_2) = 0, \quad (4)$$

$$f(\rho) = M_{\max}^2\left(\alpha_1 + \frac{\alpha_2}{1+\rho} + \frac{\alpha_1\alpha_2}{\rho}\right), \quad (5)$$

$$g(\rho) = M_{\max}^2[\alpha_1 + \alpha_2(1+\rho)^2 + \alpha_1\alpha_2\rho]. \quad (6)$$

Here, $M_{\max}$ is the largest of the component masses, $\alpha_1 = \min(M_1, M_2)/M_{\max}$, $\alpha_2 = \min[M_3$, and $\max(M_1, M_2)]/M_{\max}$.

Based on numerical simulations for triple systems with components of equal mass, Harrington [13] suggested a different stability criterion. Subsequently, Harrington generalized his criterion to the case of unequal masses and gave the final formula in [14]. The stability parameter is

$$F = \frac{a_{ex}(1-e_{ex})}{a_{in}}, \quad (7)$$

where a_{in} and a_{ex} are the semimajor axes of the internal and external binaries, respectively. The critical value F_c depends on the body masses and the mutual orbital inclination:

$$F_c = A\left[1 + B\log\left(\frac{1+\frac{M_3}{M_1+M_2}}{3/2}\right)\right] + K, \quad (8)$$

where $K = 2$; $A = 3.50$ and $B = 0.70$ for direct motions ($i = 0°$); and $A = 2.75$ and $B = 0.64$ for retrograde motions ($i = 180°$). Harrington believes that formula (8) is also valid for spatial cases of the three-body problem ($i \neq 0°, 180°$), with the exception of a small instability domain near the mutual orthogonality of the orbital planes ($i \approx 90°$).

Based on numerical simulations, Black with his coauthors suggested several related stability criteria [15–17]. However, these criteria were obtained only for systems with zero orbital eccentricities of the internal and external binaries, whereas the eccentricities of many binaries in our sample differ significantly from zero. We therefore do not use these criteria here. Donnison and Mikulskis [3] generalized Black's criterion to arbitrary eccentricities e_{in} and e_{ex}. However, since they did not provide any analytic fit, we do not use their results.

Eggleton and Kiseleva [18] suggested yet another stability criterion for hierarchical triple systems:

$$X = \frac{P_{ex}}{P_{in}} > X_c = \left(\frac{q_{ex}}{1+q_{ex}}\right)^{1/2}\left(\frac{1+e_{in}}{1-e_{ex}}\right)^{3/2} Y_c^{3/2}, \quad (9)$$

where

$$Y_c \approx 1 + \frac{3.7}{q_{ex}^{1/3}} + \frac{2.2}{1+q_{ex}^{1/3}} + \frac{1.4}{q_{in}^{1/3}}\frac{q_{ex}^{1/3}-1}{q_{ex}^{1/3}+1}. \quad (10)$$

Here, $q_{in} = M_1/M_2$, $q_{ex} = (M_1+M_2)/M_3$, and Y_c is the critical ratio of the pericentric distance of the external binary to the apocentric distance of the internal pair. The series of numerical simulations performed by Eggleton and Kiseleva [18] shows that the values of Y_c(10) differ from the empirical ones by no more than 40% in a wide range of component mass ratios, eccentricities of both binaries, mutual orbital inclinations, and initial phases of the relative orbital motions. These errors in Y_c should therefore be kept in mind when interpreting the results for observed triple systems.

Aarseth and Mardling [19] suggested a new empirical stability criterion:

$$Z = \frac{a_{ex}(1-e_{ex})}{a_{in}(1+e_{in})} > Z_c = 2.6\frac{(1+e_{ex})^{0.4}(1+q)^{0.4}}{(1-e_{ex})^{0.0728}(1+e_{in})^{1.2}}\left(1-0.3\frac{i}{\pi}\right), \quad (11)$$

where $q = M_3/(M_1+M_2)$. The authors of this criterion believe that the fit (11) is valid over a wide range of component mass ratios, eccentricities of the external and internal binaries, and mutual orbital inclinations, except for a small domain in the vicinity of $i = 90°$ (the orbital planes are nearly orthogonal).

4. STABILITY OF TRIPLE STARS

We now apply the stability criteria described in Sect. 3 to the triple stars listed in Sect. 2. Table 2 gives stability parameters s, F, X, and Z for the 38 triple systems considered and critical values s_c, F_c, X_c, and Z_c of the stability parameters. We define the stability margin of triple stars as the ratios

$$\delta_s = \frac{s-s_c}{s_c}, \quad \delta_F = \frac{F-F_c}{F_c}, \quad \delta_X = \frac{X-X_c}{X_c}, \quad \delta_Z = \frac{Z-Z_c}{Z_c}. \quad (12)$$

The larger δ, the larger the stability margin of the triple system. If $\delta < 0$, then the triple system can be dynamically unstable: motions of the bodies in the triple system result in the violation of hierarchy and/or in the escape of the distant component. The δ values (12) are also given in Table 2. The last column gives the following quantities for each system:

Table 2. Stability parameters for the triple systems

No.	Name	s F X Z	s_c F_c X_c Z_c	δ_s δ_F δ_X δ_Z	Δ_s Δ_F Δ_X Δ_Z	No.	Name	s F X Z	s_c F_c X_c Z_c	δ_s δ_F δ_X δ_Z	Δ_s Δ_F Δ_X Δ_Z
1	ADS 440	3.2	3.4	−0.046	−0.072	13	64 Ori	17	5.8	1.9	1.4
		7.9	5.3	0.50	1.5			15	5.7	1.7	13
		20	8.4	1.4	1.9			330	120	1.8	26
		7.5	2.6	1.9	2.8			11	2.9	2.8	15
2	ADS 999	47	6.2	6.6	0.90	14	HD 76360	36	6.3	4.7	2.0
		42	5.6	6.5	1.0			41	5.5	6.4	6.0
		5100	280	17	7.8			290	24	11	9.1
		36	3.7	8.8	1.1			27	2.1	12	5.8
3	Gliese 60	8.8	5.7	0.54	0.66	15	p Vel	26	6.2	3.2	1.5
		7.3	5.4	0.36	1.1			22	5.6	3.0	2.0
		25	19	0.30	0.65			580	120	3.7	5.0
		5.5	2.2	1.6	2.3			15	2.5	4.8	2.2
4	ADS 1833	1200	6.25	200	2.0	16	55 Uma	57	6.1	8.3	0.53
		1200	5.5	210	3.0			80	5.4	14	6.2
		130000	39	3500	3.3			730	17	43	9.8
		1200	3.7	310	2.9			60	2.1	27	6.4
5	β Per	12	3.1	2.9	1.7	17	ADS 8189	160	6.2	25	2.2
		33	5.4	5.1	11			190	5.4	33	5.6
		240	12	18	9.3			4300	29	140	10
		32	3.1	9.3	12			140	2.3	57	5.6
6	ξ Tau	5.4	5.6	−0.029	−0.038	18	η Vir	12	6.0	1.0	1.2
		5.5	5.7	−0.041	−0.23			17	5.4	2.1	21
		20	21	−0.037	−0.12			67	14	3.6	86
		5.5	3.9	0.41	1.3			13	2.3	4.8	25
7	ADS 2644	93	4.9	18	1.6	19	CQ Dra	7.2	0.31	22	1.8
		170	5.3	31	6.6			630	7.1	87	12
		2700	11	250	10			10000	17	590	120
		170	3.0	55	5.5			630	6.4	97	7.7
8	λ Tau	0.14	1.3	−0.89	−2.6	20	ADS 9019	1800	6.25	290	2.0
		3.6	5.1	−0.30	−6.1			1700	5.5	310	2.9
		8.4	7.6	0.095	0.47			250000	41	6100	3.3
		3.6	2.8	0.27	1.3			1700	3.7	460	2.8
9	b Per	25	3.8	5.6	1.9	21	DL Vir	73	5.5	12	2.1
		52	5.5	8.5	11			94	5.5	16	15
		460	14	32	260			1700	22	77	160
		51	3.2	15	11			94	3.7	25	8.1
10	ADS 3358	5.7	5.4	0.051	0.071	22	HD 129132	6.8	6.1	0.13	0.17
		5.3	5.7	−0.069	−0.29			11	5.5	1.0	15
		16	44	−0.63	−2.4			33	12	1.7	36
		2.9	1.6	0.75	1.6			10	2.5	2.9	22
11	IU Aur	25	6.0	1.5	1.5	23	ADS 9494	2500	5.7	430	2.0
		20	5.5	2.7	4.0			3100	5.6	550	3.7
		160	19	7.4	8.3			310000	22	14000	3.3
		20	3.5	4.7	4.0			3100	3.8	820	3.5
12	VV Ori	2.1	3.3	−0.36	−0.43	24	ADS 10157	1.5	3.7	−0.60	−0.89
		14	5.2	1.7	4.0			1.4	5.6	−0.75	−14
		81	12	5.7	8.6			3.3	26	−0.87	−2.8
		14	3.1	3.5	4.1			1.3	3.2	−0.60	−3.9

Table 2. (Contd.)

No.	Name	s F X Z	s_c F_c X_c Z_c	δ_s δ_F δ_X δ_Z	Δ_s Δ_F Δ_X Δ_Z	No.	Name	s F X Z	s_c F_c X_c Z_c	δ_s δ_F δ_X δ_Z	Δ_s Δ_F Δ_X Δ_Z
25	HZ Her	0.13	2.9	–0.95	–1.1	32	Gliese 815	110	6.0	18	2.1
		3.9	5.2	–0.25	–1.6			120	5.5	21	4.4
		21	19	0.082	0.22			3000	26	120	8.9
		3.8	3.2	0.19	0.65			120	3.6	31	4.5
26	V819 Her	27	5.8	3.6	3.8	33	ADS 14839	62	6.2	9.1	10
		34	5.4	5.3	52			57	5.5	9.4	99
		910	46	18	120			7200	190	38	160
		34	3.4	9.1	8.8			57	4.1	13	100
27	HD 157978/9	28	6.1	3.5	1.6	34	ADS 14893	17	6.2	1.7	0.62
		34	5.6	5.0	4.6			15	5.5	1.7	1.6
		320	20	15	9.2			1000	220	3.6	6.1
		34	3.7	8.2	4.3			14	4.1	2.5	1.8
28	Kuiper 84	14	6.1	1.3	0.32	35	ADS 15600	77	5.0	14	0.83
		15	5.6	1.7	6.6			120	5.5	22	3.7
		150	51	2.0	9.7			1700	28	61	3.3
		11	2.7	3.1	7.7			78	1.9	41	3.8
29	TY CrA	7.6	4.9	0.56	0.54	36	ADS 15971	4.2	4.3	–0.022	–0.025
		11	5.3	1.1	5.8			5.8	4.9	0.19	0.55
		93	25	2.8	19			30	55	–0.46	–1.3
		11	3.1	2.5	7.9			3.7	1.9	0.96	1.7
30	ADS 12214	39	5.9	5.6	1.8	37	ADS 16138	4.5	6.0	–0.25	–0.26
		47	5.6	7.3	4.4			6.1	5.6	0.087	0.48
		640	44	13	9.0			20	18	0.13	0.52
		32	2.4	12	4.3			5.8	3.4	0.71	2.5
31	Gliese 795	5.4	6.0	–0.11	–0.16	38	ADS 16591	13	5.6	1.2	0.83
		6.2	5.5	0.14	0.91			17	5.6	2.1	4.1
		16	25	–0.38	–2.1			98	25	2.9	6.3
		3.6	1.5	1.5	4.3			13	2.2	4.9	5.0

$$\Delta_s = \frac{s - s_c}{\sqrt{\sigma_s^2 + \sigma_{s_c}^2}}, \quad \Delta_F = \frac{F - F_c}{\sqrt{\sigma_F^2 + \sigma_{F_c}^2}},$$
$$\Delta_X = \frac{X - X_c}{\sqrt{\sigma_X^2 + \sigma_{X_c}^2}}, \quad \Delta_Z = \frac{Z - Z_c}{\sqrt{\sigma_Z^2 + \sigma_{Z_c}^2}}, \tag{13}$$

where σ are the errors of the corresponding quantities indicated in the subscripts. The quantities Δ characterize deviations of the observed stability parameters from their critical values with respect to the errors of these differences. If $\Delta > 2$, a given triple system can be said to be probably dynamically stable. If $\Delta < -2$, the triple system is probably dynamically unstable. If $-2 \le \Delta \le 2$, then it is difficult to say anything about the stability of a given triple system either because of large observational errors or because the triple system lies near the stability boundary.

Most of the triple systems considered are dynamically stable according to all the four criteria used, provided that we take observational data without allowance for their errors. At the same time, there are ten systems (ADS 440, ξTau, λTau, ADS 3358, VV Ori, ADS 10157, HZ Her, Gliese 795, ADS 15971, and ADS 16138) that can be dynamically unstable according to some (or even all) criteria: $\delta < 0$. This situation may be associated with several circumstances:

(1) the mutual orbital inclination of the internal and external binaries is uncertain;

(2) some of the observational data used are erroneous;

(3) the stability criteria are unreliable;

(4) the triple stars considered are dynamically young.

The quantities Δ characterize the differences between the observed and critical stability parameters

with respect to their errors. Many triple systems have small Δ. These triple systems appear to be dynamically stable, and the small Δ are coupled either with large observational errors or with the fact that the triple system is close to the stability boundary. All the criteria used yield $\Delta > 2$ only for nine systems, whereas the relative excesses of the stability parameters over their critical values $\delta > 2$ for 19 systems.

On the other hand, there are nine systems with $\Delta > 0$ and $\delta > 0$ for all criteria, but the values of Δ and δ themselves can be small. These systems appear to be also dynamically stable, but their stability margins are not as large as those of triple systems with $\delta > 2$. Note also that different stability criteria yield widely differing δ and Δ. This may be due to the fact that different stability parameters and their critical values depend differently on system parameters (component masses and orbital elements of the external and internal pairs).

At the same time, there are nine systems (ADS 440, ξTau, λTau, ADS 3358, VV Ori, HZ Her, Gliese 795, ADS 15971, and ADS 16138) that are dynamically stable ($\delta > 0$) according to some criteria and can be dynamically unstable ($\delta < 0$) according to other criteria. This is because the stability boundaries given by different criteria do not coincide: the same triple system falls within the stability zone for one criterion and within the instability zone for another criterion.

Harrington, Eggleton and Kiseleva, and Aarseth and Mardling obtained their empirical criteria from numerical simulations performed for several sets of masses and orbital parameters. The derived dependences of the critical stability parameters on body masses and orbital elements were fitted by a particular method. However, the fits suggested by the authors may prove to be poor for some of the triple stars considered. For example, the fitting error was estimated from the figures in [18] to be as large as 40%. In other empirical criteria, the fitting error can also be considerable. On the other hand, Golubev's analytic criterion places an upper limit on the critical stability parameter s_c. Kiseleva *et al.* [10] showed that the difference between the critical value s_c according to Golubev's criterion and the value of s_c determined from numerical simulations can reach 40%.

Let us consider in more detail the nine systems mentioned above, which can be dynamically unstable, and the triple system ADS 10157, which is dynamically unstable according to all the criteria considered.

The triple systems ADS 440, VV Ori, and ADS 16138 can be dynamically unstable according to Golubev's criterion in the case of retrograde motions. According to the remaining three criteria, they are dynamically stable. This may be because the angle between the orbital planes of the internal and external binaries was chosen arbitrarily.

ξ Tau is dynamically unstable according to three criteria, but the observed parameters *s*, *F*, and *X* are close to their critical values. If we take the orbital eccentricity of the external binary $e_{ex} = 0.15$ from [20], then the system is dynamically stable according to all the criteria considered.

λ Tau has a low degree of hierarchy ($X = 8.4$). This system is stable but close to the stability threshold according to two criteria: δ_X and $\delta_Z > 0$. According to Golubev's and Harrington's criteria, this system can be dynamically unstable (δ_s, $\delta_F < 0$), with a large excess over the errors: $|\Delta_s| = 2.6$ and $|\Delta_F| = 6.1$. This result may stem from the fact that Harrington's criterion for a triple system with such observed parameters is inaccurate, and that the estimated mutual inclination, which is important in Golubev's criterion, is also inaccurate.

ADS 3358 can be dynamically unstable according to Harrington's criterion, as well as Eggleton and Kiseleva's criterion (δ_F, $\delta_X < 0$). According to the other two criteria, this system is stable (δ_s, $\delta_Z > 0$). The instability is significant if Eggleton and Kiseleva's criterion is used ($|\Delta_X| = 2.4$). This result probably stems from the fact that Eggleton ad Kiseleva's criterion cannot be applied to the above triple system. Note that, according to [21], ADS 3358 may be a quadruple system: the distant component is a close binary. Since no criteria of dynamical stability are known for quadruple systems, we can say nothing about the dynamical stability of ADS 3358.

The triple system ADS 10157 is dynamically unstable according to all the criteria we used ($\delta < 0$); according to all criteria except Golubev's one, this system is unstable at a very high confidence level ($|\Delta| > 2$). This system has the lowest degree of hierarchy among all the 38 triple systems considered. Based on orbital perturbations of the distant body, Baize [22] computed the orbit of the internal pair. McCarthy [23] discovered a secondary, low-mass component of the internal pair by means of infrared speckle interferometry. At the same time, no third body was detected in the system [24]. To reach a conclusion about the dynamical stability or instability of ADS 10157 requires that the presence of a third body in the system be confirmed.

HZ Her (X-ray source Her X-1) is a hypothetical triple system. The dynamics of this system has been extensively studied by Mazeh and Shaham [25], who suggested the presence of a distant, low-mass component in it. This system is unstable according to two criteria (δ_s, $\delta_F < 0$) and stable according to the other two criteria (δ_X, $\delta_Z > 0$), although the stability margin is small. An independent confirmation of the presence of a third body in the system and more accurate estimates of its mass and orbital elements of the external binary subsystem are required.

Reliable estimates of the component masses and orbital elements, except the mutual orbital inclination of the internal and external binaries, are available for the triple system Gliese 795. It is dynamically stable according to two criteria (δ_F, $\delta_Z > 0$), although the stability margin is rather small. The system can be dynamically unstable according to Golubev's criterion in the case of retrograde motions and is significantly unsta-

ble according to Eggleton and Kiseleva's criterion ($\Delta_X = -2.1$). This situation may suggest that the latter criterion is inapplicable to the triple system in question.

The situation with the triple system ADS 15971 is similar. Two criteria indicate that it is dynamically stable (δ_F, $\delta_Z > 0$). According to Golubev's criterion, the system can be dynamically unstable in the case of retrograde motions and is stable in the case of direct motions. Eggleton and Kiseleva's criterion suggests that it is dynamically unstable ($\delta_X < 0$).

Note that, in all the five triple systems considered to be dynamically unstable according to Eggleton and Kiseleva's criterion (ξ Tau, ADS 3358, ADS 10157, Gliese 795, and ADS 15971), the less massive component of the close pair is the lightest body in the triple system. For such systems, Eggleton and Kiseleva's criterion may yield greatly (severalfold) overestimated critical ratios of the orbital periods of the external and internal binaries X_c.

5. DISCUSSION

The ages of the 38 triple stars we considered exceed the characteristic time scales of dynamical evolution for unstable triple systems with similar dynamical parameters (mean crossing time, mean system size, and mean component mass) by several orders of magnitude. Consequently, if these triple stars had been dynamically unstable, they would have long ceased to exist as triple systems. Thus, one might expect all the observed triple stars except very young and/or very wide systems to be dynamically stable.

In general, the systems we considered are consistent with this conclusion: 28 of the 38 triple stars are stable according to all criteria. For the remaining ten systems, which are unstable according to some criterion, there is always a different explanation of the result: the choice of a mutual inclination is arbitrary, the multiplicity of a system is uncertain, some stability criteria are inapplicable to individual systems, and some original data are unreliable.

ACKNOWLEDGMENTS

We are grateful to A.A. Tokovinin for a number of valuable remarks.

REFERENCES

1. V. Szebehely and K. Zare, Astron. Astrophys. **58**, 145 (1977).
2. F. C. Fekel, Astrophys. J. **246**, 879 (1981).
3. J. R. Donnison and D. F. Mikulskis, Mon. Not. R. Astron. Soc. **272**, 1 (1995).
4. C. R. Chambliss, Publ. Astron. Soc. Pacif. **104**, 663 (1992).
5. A. A. Tokovinin, Astron. Astrophys., Suppl. Ser. **124**, 75 (1997).
6. A. H. Batten, *Binary and Multiple Systems of Stars* (Pergamon, Oxford, 1973).
7. V. G. Golubev and E. A. Grebenikov, *Three-Body Problem in Celestial Mechanics* (MGU, Moscow, 1985).
8. C. Marchal, *The Three-Body Problem* (Elsever, Amsterdam, 1990).
9. L. G. Kiseleva, P. P. Eggleton, and J. P. Anosova, Mon. Not. R. Astron. Soc. **267**, 161 (1994).
10. L. G. Kiseleva, P. P. Eggleton, and J. P. Anosova, Mon. Not. R. Astron. Soc. **270**, 936 (1994).
11. V. G. Golubev, Dokl. Akad. Nauk SSSR **12**, 529 (1967).
12. V. G. Golubev, Dokl. Akad. Nauk SSSR **13**, 373 (1968).
13. R. S. Harrington, Celest. Mech. **6**, 322 (1972).
14. R. S. Harrington, Astron. J. **82**, 753 (1977).
15. F. Graziani and D. C. Black, Astrophys. J. **251**, 337 (1981).
16. D. C. Black, Astron. J. **87**, 1333 (1982).
17. Y. J. Pendleton and D. C. Black, Astron. J. **88**, 1415 (1983).
18. P. P. Eggleton and L. G. Kiseleva, Astrophys. J. **455**, 640 (1995).
19. S. J. Aarseth and R. A. Mardling, in preparation (1999).
20. C. T. Bolton, personal communication (1975).
21. W. D. Heintz, Astron. J. **111**, 408 (1996).
22. P. Baize, Astron. Astrophys., Suppl. Ser. **26**, 177 (1976).
23. D. W. McCarthy, *The Nearby Stars and the Stellar Luminosity Function*, Ed. by A. G. D. Philip and A. R. Upgren (Pergamon, New York, 1983), p. 107.
24. A. A. Tokovinin, personal communication (1998).
25. T. Mazeh and J. Shaham, Astrophys. J. Lett. **213**, L17 (1977).
26. J. L. Hershey, Astron. J. **78**, 935 (1973).
27. A. Duquennoy, Astron. Astrophys. **178**, 114 (1987).
28. P. Muller, J. Observ. **38**, 58 (1955).
29. N. Wieth-Knudsen, Lund Univ. Ars. N. F. A2 **52**, 12 (1956).
30. J. L. Newburg, Repub. Obs. Johannesburg Circ. **7**, 190 (1969).
31. J. H. Karle, personal communication (1977).
32. A. Valbousquet, Astron. Astrophys., Suppl. Ser. **41**, 295 (1980).
33. M. J. Sarna, Mon. Not. R. Astron. Soc. **262**, 534 (1993).
34. J. W. Stein and W. R. Beardsley, Vistas Astron. **21**, 43 (1977).
35. G. Gatewood, J. K. de Jonge, and W. D. Heintz, Astron. J. **109**, 434 (1995).
36. F. C. Fekel, Astrophys. J. **268**, 274 (1983).
37. J. Hopmann, Ann. Univ.-Sternw. Wien **26**, 22 (1964).
38. F. C. Fekel and J. Tomkin, Astrophys. J. **263**, 289 (1982).
39. G. Hill, G. C. L.Aikman, A. P. Cowley, *et al.*, Astrophys. J. **208**, 152 (1976).
40. P. Mayer and H. Drechsel, Astron.Astrophys. **183**, 61 (1987).
41. P. Mayer, Bull. Astron. Inst. Czech. **34**, 335 (1983).
42. C. R. Chambliss, Astrophys. Space Sci. **89**, 15 (1983).
43. H. W. Duerbeck, Astron. Astrophys., Suppl. Ser. **22**, 19 (1975).
44. F. C. Fekel and C.D. Scarfe, Astron. J. **92**, 1162 (1986).

45. F. C. Fekel, Ph.D. Thesis, Univ. of Texas at Austin (1979).
46. W. S. Finsen, Circ. Inf. No. 60 (1973).
47. D. S. Evans, Mon. Not. R. Astron. Soc. **142**, 523 (1969).
48. W. S. Finsen, Circ. Inf. No. 44 (1968).
49. J. Horn, J. Kubat, P. Harmanec, *et al.*, Astron. Astrophys. **309**, 521 (1996).
50. H. A. McAlister, B. D. Mason, and W. I. Hartkopf, Astron. J. **106**, 1639 (1993).
51. R. M. Petrie and D. M. Laidler, Publ. Dominion Astrophys. Obs. **9**, 181 (1952).
52. P. Couteau, J. Observ. **48**, 39 (1965).
53. W. I. Hartkopf, H. A. McAlister, X. Yang, and F. C. Fekel, Astron. Astrophys. **103**, 1976 (1992).
54. D. Reimers, R. F. Griffin, and A. Brown, Astron. Astrophys. **193**, 180 (1988).
55. R. L. Walker and C. R. Chambliss, Astron. J. **90**, 346 (1985).
56. W. D. Heintz, Astrophys. J. **208**, 474 (1976).
57. H. A. McAlister and W. I. Hartkopf, personal communication (1984).
58. E. Schöffel, Astron. Astrophys. **61**, 107 (1977).
59. D. J. Barlow and C. D. Scarfe, Astron. J. **102**, 2098 (1991).
60. L. Binnendijk, Astron. J. **60**, 355 (1955).
61. D. M. Popper, Astrophys. J. **97**, 394 (1943).
62. C. Marceroni, L. Milano, G. Russo, and C. Sollazzo, Astron. Astrophys., Suppl. Ser. **45**, 187 (1981).
63. W. D. Heintz, Astrophys. J., Suppl. Ser. **37**, 71 (1978).
64. G. Hill, W. A. Fisher, and D. Holmgren, Astron. Astrophys. **211**, 81 (1989).
65. J. Middleditch and J. Nelson, Astrophys. J. **208**, 567 (1976).
66. H. D. Tananbaum and J. B. Hutchings, Ann. New York Acad. Sci. **262**, 299 (1975).
67. C. D. Scarfe, D. J. Barlow, F. C. Fekel, *et al.*, Astron. J. **107**, 1529 (1994).
68. A. A. Tokovinin, Pis'ma Astron. Zh. **20**, 368 (1994).
69. P. Corporon, A. M. Lagrange, and H. Beust, Astron. Astrophys. **310**, 228 (1996).
70. F. C. Fekel, Astron. J. **80**, 844 (1975).
71. W. S. Finsen, Circ. Inf. No. 69 (1976).
72. P. Baize, Astron. Astrophys., Suppl. Ser. **44**, 199 (1981).
73. A. Duquennoy and M. Mayor, Astron. Astrophys. **200**, 135 (1988).
74. P. Baize, Astron. Astrophys., Suppl. Ser. **87**, 49 (1991).
75. F. C. Fekel, C. D. Scarfe, D. J. Barlow, *et al.*, Astron. J. **113**, 1095 (1997).
76. F. R. West, Astrophys. J. **205**, 194 (1976).
77. G. Gatewood and I. Han, Astron. J. **110**, 1860 (1995).
78. H. A. McAlister, Astrophys. J. **236**, 522 (1980).
79. C. A. Hummel and J. T. Armstrong, *Very High Angular Resolution Imaging*, Ed. by J. G. Robertson and W. J. Tango (Kluwer Acad., Dordrecht, 1994), p. 410.
80. G. Zeller, Ann. Univ. Sternw. Wien **26**, 111 (1965).
81. W. D. Heintz, Astrophys. J. **284**, 806 (1984).
82. B. Cester, Mem. Soc. Astron. Ital. **33**, 177 (1962).
83. P. Baize, J. Observ. **38**, 37 (1955).

Translated by A. Dambis

Astronomy Letters, Vol. 26, No. 4, 2000, pp. 261–267. Translated from Pis'ma v Astronomicheskiĭ Zhurnal, Vol. 26, No. 4, 2000, pp. 313–320.

Internal Rotation of the Sun as Inferred from GONG Observations

E. A. Gavryuseva[1, 2], V. G. Gavryusev[3]*, and M. P. Di Mauro[4]

[1] *Institute of Nuclear Research, Russian Academy of Sciences, pr. 60-letiya Oktyabrya 7a, Moscow, 117312 Russia*
[2] *Osservatorio di Capodimonte, Via Moiariello 16, I-80131 Naples, Italy*
[3] *Centro per l'Astronomia Infrarossa e lo Studio del Mezzo Interstellare, Consiglio Nazionale delle Ricerche, Largo E. Fermi 5, I-50125 Florence, Italy*
[4] *Istituto di Astronomia, Città Universitaria, Viale A. Doria 6, I-95125 Catania, Italy*

Received May 21, 1999

Abstract—Helioseismology is a direct and most informative method of studying the structure and dynamics of the Sun. Determining the internal differential rotation of the Sun requires that the frequencies of its eigentones be estimated with a high accuracy, which is possible only on the basis of continuous long-term observations. The longest quasi-continuous series of data have been obtained by the Global Oscillation Network Group (GONG). The parameters of each individual mode of solar acoustic oscillations with low spherical degrees $l = 0, 1, 2, 3, 4, 5, 6$ are determined by using 1260-day-long series of GONG observations. The mean frequency splitting by rotation for the modes of each radial order n is calculated by using all possible combinations between the eigenfrequencies in multiplets. As a result, it has become possible to statistically estimate the splitting and its measurement errors for the modes of each radial order. The mean splitting for each given degree $l = 1$–6 is presented under the assumption of its independence of oscillation frequency, which holds for the achieved accuracy. The frequencies and splittings for the modes with low spherical degrees l, together with the MDI group results for higher degrees l, are used to invert the radial profile of solar angular velocity. Using the SOLA method to solve the inverse problem of restoring the rotation profile has yielded solutions sensitive to the deepest stellar interiors. Our results indicate that the solar core rotates faster than the surface, and there may be a local minimum in angular velocity at its boundary. © *2000 MAIK "Nauka/Interperiodica".*

Key words: *solar oscillations, solar differential rotation*

1. INTRODUCTION

Helioseismology is one of the most powerful tools for obtaining information about the internal structure of the Sun. The radial dependences of the speed of sound and angular velocity can be derived by solving the inverse problem. The inversion procedures use the oscillation frequencies and fine structure of the spectrum, i.e., the so-called frequency splitting into multiplets under the effect of rotation through the removal of their degeneracy due to the appearance of an east–west asymmetry. Information about the deepest layers comes from the acoustic modes of the lowest spherical degrees l, which penetrate almost down to the center. So far, attempts to restore the rotation of the solar core have yielded conflicting results. One group of measurements of low-l splittings gives a slower rotation of the solar core than that of the surface [1, 2], though others [3–15] suggest a relatively faster rotation of the core.

The fine spectrum can be studied only on the basis of continuous long-term observations. One of the best organized networks of ground-based facilities was created on the initiative of the National Solar Observatory (USA) and includes six globally distributed instruments. The velocities on the solar surface have been measured in continuous mode since May 5, 1995, with a high spatial resolution by using a 256×242-pixel CCD array. Subsequently, the data from different facilities are merged, calibrated, and decomposed into spherical harmonics. The members of the GONG project have at their disposal time series of the coefficients in the decomposition of surface velocities into modes of different spherical degrees l and azimuthal orders m, where l characterizes the global asymmetry over the sphere, whereas m characterizes only the asymmetry in longitude, $m = 0, \pm 1, \ldots, \pm l$. We determined the parameters of the mode profiles for all clearly visible radial orders n (n is the number of nodal points in radius, where the radial shift from the equilibrium position is zero) of solar oscillations with low spherical degrees $l = 0, 1, 2, 3, 4, 5, 6$ by using the 1260-day-long time series obtained in the GONG experiment from May 7, 1995, until October 17, 1998. We *statistically* estimated the rotational splitting of individual modes and its errors. For this purpose, we used all possible combinations between the multiplet frequencies for each radial order n. To increase the statistics of measurements, we made all determinations for 42 data series, each with a

* E-mail address for contacts: vladimir@arcetri.astro.it

duration of 400 days, shifted with a 20-day step. The constructed splitting distributions are mostly fairly close to the normal ones. This information obtained from the longest continuous series available to date with a filling no less than 87% is used to restore the radial distribution of angular velocity down to the solar core. In conclusion, we discuss a possible interpretation of our results.

2. SPLITTING MEASUREMENTS

The GONG time series have occasional gaps, but these are rather short (no more than 13%, on average). As a result, we see virtually no daily harmonics in the spectrum. To determine the profiles of solar *p*-modes, we used the method of Fourier power averaging (FPA) [11], which is a special case of the segment-averaging technique [16] specially adapted to the needs of helioseismology and takes into account the finite visibility time of individual oscillation modes. In this method, the power spectrum for a complete series is obtained by averaging the power for each "window" running over the complete series of observations. The critical parameter of the method, the size of the running window, was chosen in such a way that it exceeded the mean visibility time of a mode (different for different modes). This method yields relatively smooth mode profiles averaged over the observing time as functions of frequency. In agreement with the central limit theorem, the uncorrelated noise for such a long data series is fairly normalized when the power is averaged. The parameters of the oscillation mode profiles can therefore be obtained by fitting the FPA spectra by a nonlinear least-squares method.

In the GONG time series intended for the detection of oscillations with low spherical degrees *l*, we also see other modes of different spherical degrees at close frequencies. We used this "contamination", which deteriorates the accuracy of the oscillation parameters when the profile of the "contaminating" mode is close to the profile of the mode studied, as an additional source of information about the accompanying modes, when it was reasonable. The parameters of each individual *m* component from a $(2l + 1)$-component rotational multiplet were measured directly from the FPA profiles. In addition, the FPA spectra were fitted by appropriate combinations of Lorentzians with free parameters (frequencies, power amplitudes, profile half-widths) with allowance for noise. Figure 1 shows the FPA spectrum near the $m = \pm 1$ doublet of dipole oscillations with radial order $n = 15$, as it is seen in the power spectrum of the time series for $l = 0$. The solid line represents the FPA profiles, and the dotted line corresponds to the fit by a combination of two Lorentzians. The splitting can be measured directly as half the separation between the maxima of the FPA profiles for the $l = \pm 1$ components, as well as from the Lorentzian profiles. The latter is, in a sense, more accurate, because it takes into account the mutual influence of the wings of adjacent modes or components.

Mean (most probable) sidereal splitting $\Delta\nu$ obtained from the distributions over all measured radial orders *n* and its standard deviation σ for spherical degrees $l = 1, 2, 3, 4, 5, 6$

l	1	2	3	4	5	6
$\Delta\nu$, nHz	453.6	430.3	429.3	432.1	435.8	434.7
σ, nHz	5.5	5.3	3.8	2.5	1.7	1.4

We used all possible independent combinations of the measured frequencies of the *m* components in each multiplet to calculate the mean multiplet splitting by assuming that, to a first approximation, it did not depend on *m*. This assumption is fairly realistic for low *l*; at least this dependence is not observed at the achieved accuracy. The splitting distributions thus obtained are a good approximation to the normal one, and all possible deviations from this assumption are appreciably smaller than the measurement errors of the frequencies. These distributions also yield a statistical estimate of the corresponding standard errors.

The number of *m* components in the multiplet for $l = 6, 5, 4$, and even for $l = 3$ is large enough to provide a satisfactory statistics. For $l = 2$, we additionally used measurements of the quadrupole multiplets seen in the time series of oscillations for $l = 0, 1, 3, 4$ by assuming that the errors of the frequencies in the time series were basically independent for different *l*. The derived splitting distributions confirm this assumption. The splitting of the $l = 1$ dipole modes is most difficult to determine. Only three possible independent combinations of the components of each multiplet are not statistically representative. The presence of the $m = -1$ components in the time series intended for the detection of $m = +1$ and, conversely, the noticeable presence of other modes near the frequency of the mode under study, because of imperfect separation of the original measurements into coefficients of the specified spherical functions ("spatial leakage" increases with decreasing spherical number *l*), all makes the determination of the frequencies of dipole oscillations less accurate than that for the modes with other low *l*. Additional information about the dipole modes obtained by using the time series of the coefficients of the harmonics with $l = 0, 2, 3, 4$ improves the situation, although the splitting distributions show much larger deviations from the normal one. As a result, the errors in the splittings for the $l = 1$ modes are larger than those for higher *l*. Figure 2 shows the distributions of the sidereal splittings obtained for each radial order *n* for the spherical degrees from 1 to 6. We measured the mean splittings in the rotational multiplets of the following radial orders: for $l = 1$ $n = 6$–27; for $l = 2$ $n = 5$–32; for $l = 3$ $n = 5$–30; for $l = 4$ $n = 4$–32; for $l = 5$ $n = 4$–32; for $l = 6$ $n = 3$–31.

For each *l*, we also calculated the mean splittings for all the measured radial orders and their standard deviations. The table lists the calculated mean sidereal splittings for *l* from 1 to 6.

At present, there are a fairly large number of rotational-splitting measurements for low *l*. These measurements were made on the basis of different experi-

ments, different periods of time, and different techniques used for data analysis. Naturally, the results of different authors differ, sometimes markedly. In particular, the very small splittings, especially for $l = 1, 3$, are interpreted as an indication that the solar core rotates slower than the surface, whereas the large ones, on the contrary, require that the angular velocity in the central regions exceed considerably that of the surface regions. Figure 3 compares the measurements of rotational splitting made by different authors for $l = 1, 2$. The set of tables used does not claim to be complete, but gives a rather comprehensive idea about the results obtained approximately over the last ten years in virtually all dedicated experiments: BISON ([1, 17], "C" series of data; [2]); GONG [12, 18, 19]; GOLF [15, 20, 21]; IPHIR [3, 4, 11, 22]; IRIS [6, 7, 14, 23]; MDI [24]; VIRGO [10]; LOI [8, 9, 25, 26, 27].

Figure 3 shows the number of intersections of the confidence intervals of different authors (the measured sidereal splitting plus/minus the standard deviation) for $l = 1$ and $l = 2$ as a function of sidereal splitting at 1-nHz steps. In this representation, we clearly see that the data of different authors fit well into the idea that fairly complex multiple measurements yield a splitting distribution close to the normal one (if they are, at least approximately, independent and free of systematic errors). Each distribution for $l = 1$ and $l = 2$ has a distinct "agreement" peak. The sidereal rotational splittings presented in this paper are shown in Fig. 3 by vertical lines above the distributions. The horizontal lines intersecting them correspond to the confidence interval. It is easy to see that the "agreement" peaks lie within these confidence intervals. A similar situation also takes place for higher $l = 3, 4, 5, 6$.

3. INTERNAL ROTATION OF THE SUN

We determined the rotation of the solar core by inversion of a set of rotational splittings of the acoustic oscillation frequencies for low degrees using GONG observations. This set of splittings was composed of the splittings averaged over n for each l with the corresponding errors. At the achieved accuracy of measurements, the splitting does not depend on frequency for a given l.

Determination of the rotation of the solar core is complicated by the fact that a major contribution to the frequency splitting comes from the outer solar zones. For the analysis, we used our results for $1 \le l \le 6$ combined with the frequencies estimated for $7 \le l \le 80$ on the basis of MDI measurements [28]. The inversion of splittings $\Delta\nu_{n,l}$ allows the radial dependence of equatorial angular velocity to be determined by solving a one-dimensional integral equation:

$$\Delta\nu_i = \int_0^{R_\odot} K_i(r)\frac{\Omega(r)}{2\pi}dr + \sigma_i, \qquad (1)$$

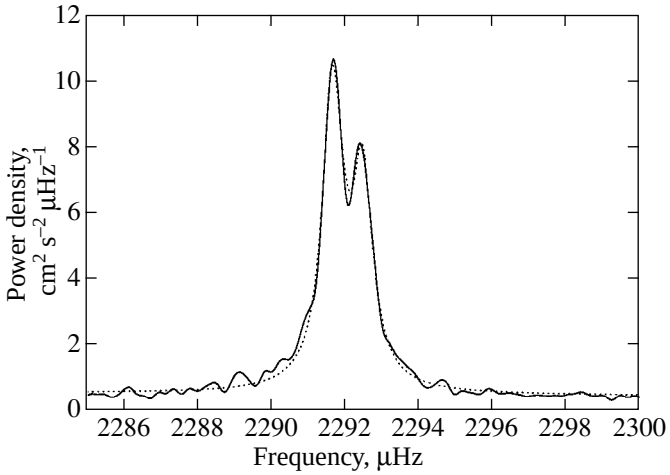

Fig. 1. Profile of the $m = \pm 1$ doublet $l = 1$ of the $n = 15$ (dipole) mode. The solid line represents the FPA profile, and the dotted line indicates the Lorentz fit.

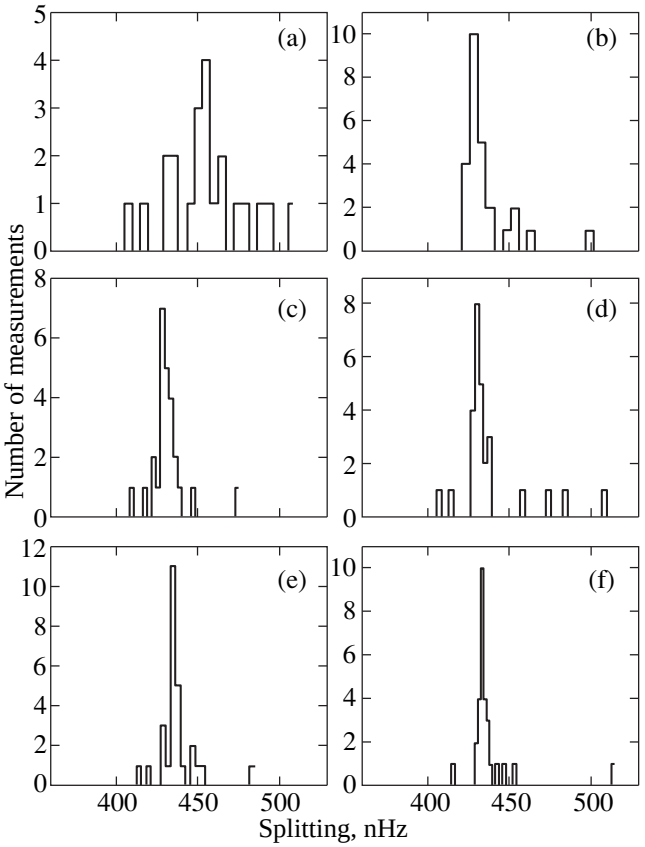

Fig. 2. Distribution of measured sidereal splittings for various radial orders n for (a) $l = 1$, (b) $l = 2$, (c) $l = 3$ (d) $l = 4$, (e) $l = 5$, and (f) $l = 6$.

where $K(r)$ are the kernels calculated, as described by Di Mauro *et al.* [29], for each mode $i = 1, \ldots, k$ of spherical degree l and radial order n, which depend on the equilibrium solar model and oscillation eigenfunctions; σ_i are the standard deviations calculated from the experimental errors.

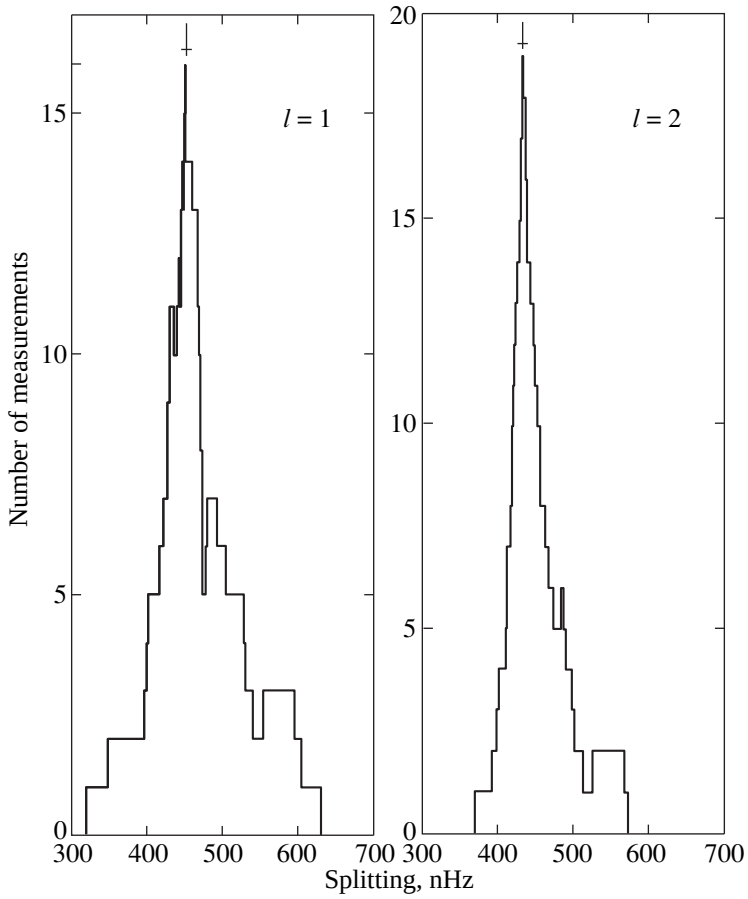

Fig. 3. Number of intersections of the confidence intervals of various authors (measured sidereal splitting plus/minus standard deviation) for $l = 1$ and $l = 2$ versus sidereal splitting at 1-nHz steps. The sidereal rotational splittings presented here are indicated by vertical lines above the distributions. The horizontal lines intersecting them correspond to the confidence interval.

To solve the inverse problem, we used the method of averaging kernels [29], which allows data to be combined to determine the localized weighted averages of angular velocity $\bar{\Omega}(r_0)$ at each selected radius r_0:

$$\bar{\Omega}(r_0) = \sum_{t}^{k} c_i(r_0)\Delta\nu_i = \sum_{i=1}^{k} c_i(r_0)\int_0^{R_\odot} K_i(r)\Omega(r)dr,$$

where $c_i(r_0)$ are the inversion coefficients and

$$\mathcal{H}(r_0, r) = \sum_{i=1}^{k} c_i(r_0)K_i(r) \qquad (2)$$

are the averaging kernels. We used this method in the form described by Pijpers and Thompson [30] and known as SOLA (subtractive optimally localized averaging). The coefficients $c_i(r_i)$ were determined by minimizing the functional

$$\int_0^{R_\odot} [G(r_0, r) - \mathcal{H}(r_0, r)]^2 dr + \alpha\sum_{i=1}^{k} c_i(r_0)^2\sigma_i^2 \qquad (3)$$

provided that $|\mathcal{H}| = 1$, using Gaussians $G(r_0, r)$ with appropriate widths centered on the given radius as fits to the averaging kernels. Because of internal difficulties of the inversion procedures, it is necessary to introduce a regularization parameter α, which allows a compromise choice to be made between the errors in the position and magnitude of the rotation. The regularization parameter varies along the radius to maintain a constant width of the averaging kernels and to achieve a higher accuracy of kernel resolution close to the nominal concentration of points.

Figure 4 shows some averaging kernels obtained for the set of experimental data used.

In Fig. 5, the equatorial angular velocity is plotted versus depth. The spatial resolution along the radius at each point $\bar{\Omega}(r_0)$ corresponds to the half-width at half-maximum of the kernel functions, which are nearly Gaussian in shape. The vertical errors are the standard deviations due to observational errors. Since the solutions are naturally less backed up by data in the deep interiors, a high accuracy cannot be achieved there. However, it is easy to see that the accuracy achieved in determining the splitting in rotational multiplets for

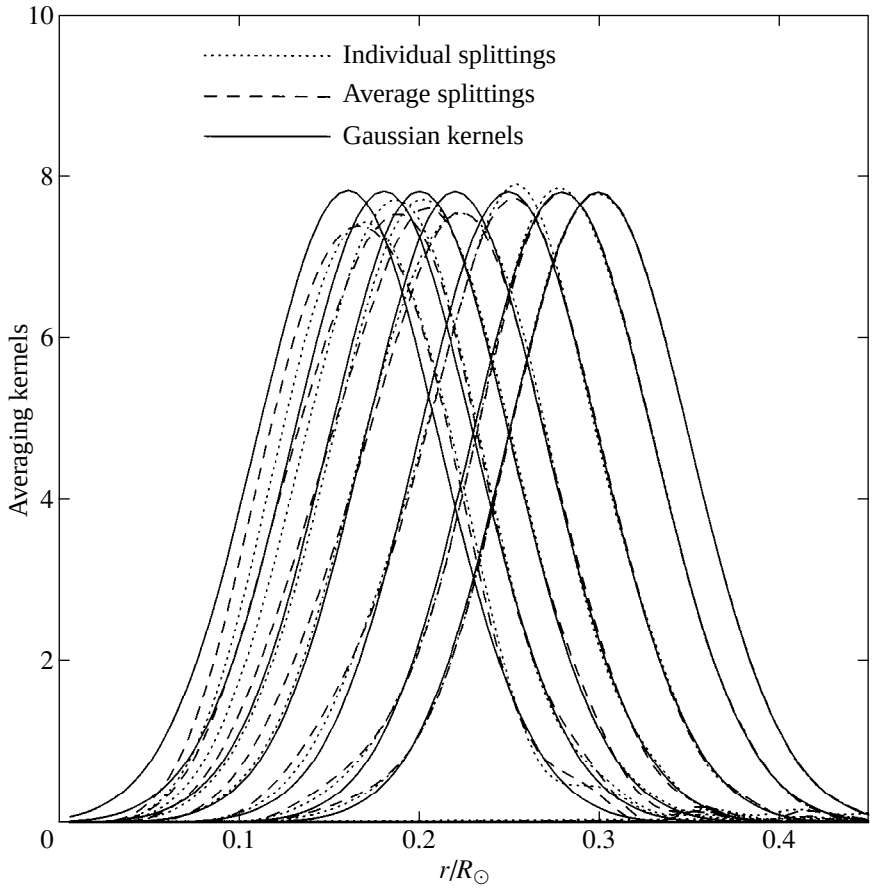

Fig. 4. Averaging kernels obtained by SOLA inversion and used to calculate the rotation velocity (Fig. 5) for small radii. The small deviations from Gaussians (solid lines) correspond to a more accurate inversion.

low l (and these provide basic information about the deep interiors) enables us to measure deviations from the equatorial surface angular velocity that exceed two standard deviations for the smallest radii. Near the local minimum ($0.18R_\odot$), this deviation exceeds 5σ.

We conclude that the solar core rotates at a velocity that is a factor of 1.2–1.5 higher than the equatorial surface angular velocity. This conclusion is in qualitative and, occasionally, quantitative agreement with other experiments, such as IRIS and GOLF [29], but is in conflict with the conclusion of the Birmingham group about a slower rotation of the interiors compared even to the low angular velocity near the poles [1].

4. DISCUSSION

As we see from Fig. 5, the inversion strongly suggests that the core rotates faster than the envelope. To refine the rotation velocity requires as accurate input data as possible, i.e., as accurate measurements of the frequency splitting for modes of low degrees l and various radial orders as possible.

We clearly see a local minimum in angular velocity near $0.18R_\odot$ and a hint of a less significant local maximum near $0.43R_\odot$. This local maximum and the subsequent decrease in angular velocity with decreasing radius was previously reported by Schou *et al.* [31] for $r \geq 0.2R_\odot$ (the inversion was carried out by using six-month-long LOWL measurements). The small waves on the angular-velocity curve at $r > 0.3R_\odot$ are caused by the MDI data for high l. Here, we are interested only in the rotation in the solar core, about which our measurements give basic information, and we do not discuss the causes of this phenomenon. It should also be added that many other inversions, for example, of the MDI data [32], reveal a difference between the speeds of sound in the Sun and in the standard solar model near the same radius, where the angular velocity has a minimum. It should be noted that, since inversion of the radial angular-velocity profile is basically an ill-posed problem and requires regularization for its solution, the behavior of the solution should be studied further under various assumptions about regularization to obtain more reliable results.

The behavior of the angular velocity presented in Fig. 5, if confirmed, may suggest the presence of an extended layer intermediate between the rapidly rotating core and the more slowly rotating envelope, where

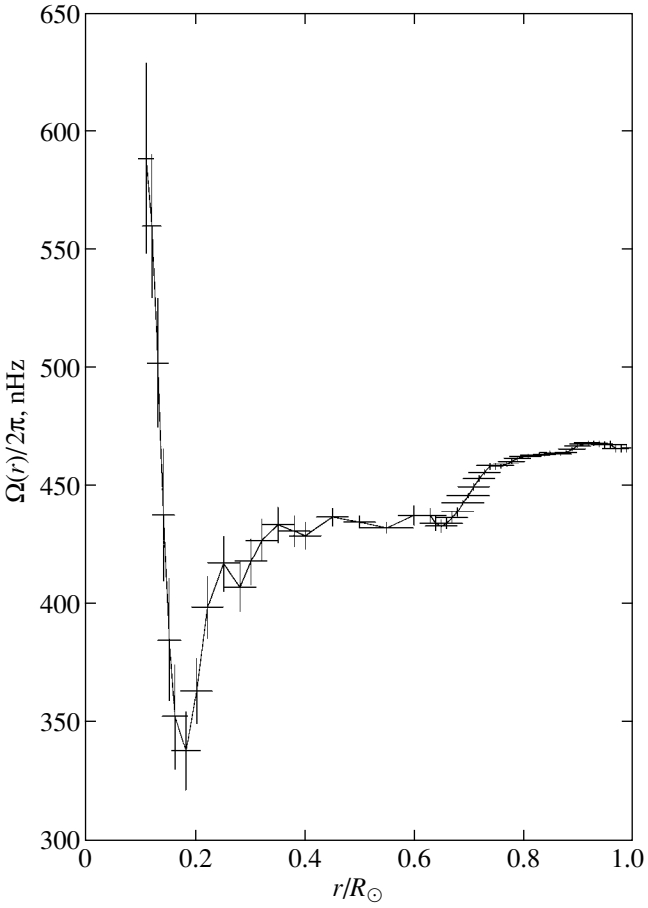

Fig. 5. Solar angular velocity obtained by inversion of a set of mean frequency splittings from GONG observations for low spherical degrees *l*. The same splitting was used for all radial orders *n* and for each *l* from 1 to 6.

hydrodynamic instabilities take place. It is probably not accidental that the middle of this layer is located near the maximum of ^{3}He concentration. Macroscopic motions inevitably mix the matter in the Sun, bringing additional hydrogen and ^{3}He to the central region, make the distributions of concentrations flatter and the temperature inside the nuclear active zone lower. This decreases the fluxes of high-energy neutrinos and reduces the discrepancies in the so-called problem of a deficit of solar neutrinos. Magnetic fields etc. can also be generated in this unstable zone. In this case, many interesting physical processes should be taken into consideration, in addition to those which were taken into account by the standard solar model.

ACKNOWLEDGMENTS

We used data from the GONG (Global Oscillation Network Group) project managed by the National Solar Observatory (USA), a Division of the National Optical Astronomy Observatories operated by the Association of Universities for Research in Astronomy (AURA), under a cooperative agreement with the National Science Foundation (USA). The GONG data were instruments operated by the Big Bear Solar Observatory, High Altitude Observatory, Learmonth Solar Observatory, Udaipur Solar Observatory, Instituto de Astrofísico de Canarias, and Cerro Tololo Interamerican Observatory. BISON and IRIS are two networks of ground-based stations intended to measure solar acoustic oscillations during observations of the Sun as a star without spatial resolution of spherical harmonics. GOLF, MDI, and VIRGO (LOI) are the experiments carried out onboard the SOHO space station located near the Lagrangian point between the Sun and the Earth. SOHO is a joint project of ESA and NASA.

REFERENCES

1. Y. Elsworth, R. Howe, G. R. Isaak, *et al.*, Nature **376**, 669 (1995).
2. W. J. Chaplin, Y. Elsworth, R. Howe, *et al.*, Mon. Not. R. Astron. Soc. **280**, 849 (1996).
3. T. Toutain and C. Fröhlich, Astron. Astrophys. **257**, 287 (1992).
4. T. Toutain and A. G. Kosovichev, Astron. Astrophys. **284**, 265 (1994).
5. S. Loudagh, J. Provost, G. Berthomieu, *et al.*, Astron. Astrophys. **275**, L25 (1993).
6. E. Fossat, S. Loudagh, B. Gelly, *et al., Helio- and Astero-Seismology from the Earth and Space*, Ed. by R. K. Ulrich, E. J. Rhodes, Jr., and W. Däppen (Astron. Soc. Pacif. Conf. Ser., San Francisco, 1995), Vol. 76, p. 24.
7. E. Fossat *et al.*, *Helioseismology*, Ed. by J. T. Hoeksema *et al.* (ESA Publ. Division, ESA SP-376, 1995), Vol. 2, p. 261.
8. T. Appourchaux *et al.*, Astron. Astrophys. **294**, L13 (1995).
9. T. Appourchaux *et al.*, *Helioseismology*, Ed. by J. T. Hoeksema *et al.* (ESA Publ. Division, ESA SP-376, 1995), Vol. 2, p. 265.
10. T. Appourchaux *et al.*, *Sounding Solar and Stellar Interiors, IAU Symp. No. 181*, Ed. by J. Provost and F.-X. Schmider (Université de Nice, Nice, 1996), Poster Volume, p. 3.
11. V. Gavryusev and E. Gavryuseva, Astron. Astrophys. **310**, 651 (1996).
12. V. Gavryusev and E. Gavryuseva, *New Eyes to See Inside the Sun and Stars, IAU Symp. No. 185*, Ed. by F.- L. Deubner *et al.* (Kluwer, Dordrecht, 1998), p. 153.
13. V. Gavryusev and E. Gavryuseva, *Structure and Dynamics of the Interior of the Sun and Sun-like Stars*, Ed. by S. Korzennik and A. Wilson (ESA Publ. Division, ESA SP-418, 1998), Vol. 1, p. 187.
14. M. Lazrek, A. Pantel, E. Fossat, *et al.*, Solar Phys. **166**, 1 (1996).
15. M. Lazrek, F. Baudin, L. Bertello, *et al.*, Solar Phys. **175**, 227 (1997).
16. P. D. Welch, IEEE Trans. *AU-15*, No. 2, 70 (1967).
17. Y. Elsworth, R. Howe, G. R. Isaak, *et al., Helio- and Astero-Seismology from the Earth and Space*, Ed. by

R. K. Ulrich, E. J. Rhodes, Jr., and W. Däppen (Astron. Soc. Pacif. Conf. Ser., San Francisco, 1995), Vol. 76, p. 43.

18. E. Gavryuseva, V. Gavryusev, and M. P. Di Mauro, *Structure and Dynamics of the Interior of the Sun and Sun-Like Stars*, Ed. by S. Korzennik and A. Wilson (ESA Publ. Division, ESA SP-418, 1998), Vol. 1, p. 193.
19. M. C. Rabello-Soares and T. Appourchaux, Astron. Astrophys. **345**, 1027 (1999).
20. G. Grec *et al.*, *Sounding Solar and Stellar Interiors, IAU Symp. No. 181*, Ed. by J. Provost and F.- X. Schmider (Université de Nice, Nice, 1996), p. 91.
21. D. Fierry-Fraillon *et al.*, *Structure and Dynamics of the Interior of the Sun and Sun-Like Stars*, Ed. by S. Korzennik and A. Wilson (ESA Publ. Division, ESA SP-418, 1998), Vol. 1, p. 161.
22. T. Toutain, *Helio- and Astero-Seismology from the Earth and Space*, Ed. by R. K. Ulrich, E. J. Rhodes, Jr., and W. Däppen (Astron. Soc. Pacif. Conf. Ser., San Francisco, 1995), Vol. 76, p. 34.
23. L. Gizon, E. Fossat, M. Lazrek, *et al.*, Astron. Astrophys. **317**, L71 (1997).
24. T. Toutain and A. G. Kosovichev, *Structure and Dynamics of the Interior of the Sun and Sun-like Stars*, Ed. by S. Korzennik and A. Wilson (ESA Publ. Division, ESA SP-418, 1998), Vol. 1, p. 349
25. T. Brown and C. Morrow, *The Internal Solar Angular Velocity*, Ed. by B. R. Durney and S. Sofia (Reidel, Dordrecht, 1987), Vol. 137, p. 7.
26. A. Cacciani *et al.*, *Helioseismology*, Ed. by J. T. Hoeksema *et al.* (ESA Publ. Division, ESA SP-376, 1995), Vol. 2, p. 311.
27. E. J. Rhodes, Jr., A. Cacciani, S. Korzennik, *et al.*, Astrophys. J. **351**, 687 (1990).
28. J. Schou, H. M. Antia, S. Basu, *et al.*, Astrophys. J. **505**, 390 (1998).
29. M. P. Di Mauro, W. A. Dziembowski, and L. Paternó, *Structure and Dynamics of the Interior of the Sun and Sun-Like Stars*, Ed. by S. Korzennik and A. Wilson (ESA Publ. Division, ESA SP-418, 1998), Vol. 1, p. 759.
30. F. R. Pijpers and M. J. Thompson, Astron. Astrophys. **262**, L33 (1992).
31. J. Schou, S. Tomczyk, and M. J. Thompson, *Helioseismology*, Ed. by J. T. Hoeksema *et al.* (ESA Publ. Division, ESA SP-376, 1995), Vol. 2, p. 275.
32. A. G. Kosovichev *et al.*, Solar Phys. **166**, 43 (1996).

Translated by G. Rudnitskii